



NMR and neutron total scattering studies of silicon-based anode materials for lithium-ion batteries

Christopher James Kerr

St Catharine's College

This dissertation is submitted for the degree of Doctor of Philosophy and contains the corrections requested by the examiners to the dissertation submitted on 23 May 2016, which was itself a revision of the original dissertation submitted on 31 October 2014.

Abstract

NMR and neutron total scattering studies of silicon-based anode materials for lithium-ion batteries

Christopher James Kerr

Silicon (in the form of lithium silicides) has almost ten times the theoretical charge storage capacity of graphite, the anode material used in most commercially-available lithium-ion batteries. Replacing graphite with silicon therefore promises a substantial improvement over the state-of-the-art in electrochemical energy storage. However, it has proved difficult to realise this high theoretical capacity in a practical electrochemical cell and maintain it over repeated charge-discharge cycles. This dissertation presents experimental work probing the changes in local structure occurring during the electrochemical reactions of lithium with silicon, using neutron total scattering and nuclear magnetic resonance, together with novel processing methodologies for analysing the resulting data, in the hope of suggesting ways of improving the performance of silicon-based lithium-ion batteries.

Neutron total scattering patterns were obtained from silicon-based anode materials extracted from cells at various states of charge. These samples were composed of a heterogeneous mixture of amorphous, crystalline and disordered crystalline materials. Reverse Monte Carlo is a technique for obtaining structural information from experimental data (particularly total scattering patterns) from amorphous and disordered crystalline materials. However, previously existing Reverse Monte Carlo software could only handle homogeneous materials. Therefore, the `RMCprofile` software package was extended to handle data from heterogeneous samples. The improved `RMCprofile` was applied to the aforementioned total scattering patterns, but the much stronger scattering from the other components (themselves not well-characterised) swamped that from the lithium silicide. Future work should attempt to reduce the scattering from the inactive components, particularly the hard-to-model incoherent scattering.

NMR data were acquired *in situ* from silicon-nanowire-based lithium-ion batteries during repeated charge-discharge cycles, achieving much better electrochemical performance than had been seen in previous *in situ* experiments with silicon. Owing to the large quantities of data obtained, an automated, model-free dimensionality reduction technique was needed. The NMR data were processed using principal component analysis and a variant of non-negative matrix factorisation. With both of these methods, one of the components was found to be associated with high voltages *vs* $\text{Li}|\text{Li}^+$ (*i.e.* a fully discharged anode). This region has seen very little interest by comparison with the low voltage (high levels of lithiation) region of the charge-discharge cycle, so this discovery suggests a new avenue for future research.

Declaration

This dissertation is the result of my own work and includes nothing which is the outcome of work done in collaboration except as declared in the Preface and specified in the text. It is not substantially the same as any that I have submitted, or am concurrently submitting, for a degree or diploma or other qualification at the University of Cambridge or any other University or similar institution except as declared in the Preface and specified in the text. I further state that no substantial part of my dissertation has already been submitted, or is being concurrently submitted, for any such degree, diploma or other qualification at the University of Cambridge or any other University or similar institution except as declared in the Preface and specified in the text. This dissertation does not exceed the prescribed limit of 60 000 words.

Christopher James Kerr
19 April 2017

Acknowledgments

I would like to thank the Cambridge Nano Science and Technology Doctoral Training Centre (NanoDTC) for their financial support, and the UK Science and Technology Facilities Council and US Department of Energy for providing access to research facilities. The Institut Laue-Langevin, the International Center for Materials Research and the German Neuroinformatics Node all subsidised my attendance at conferences or training workshops which they had organised.

The Grey group has too many members for me to thank them all individually for the help and support they gave, but there are some who deserve special notice. Elodie Salager's instruction and gentle encouragement was very helpful during the time we worked together. Alison Michan seemingly always had time to discuss tricky issues of silicon chemistry or just to provide moral support. I would particularly like to thank Kenny Rosina for helping with battery assembly when I was unable to do this myself due to a broken thumb.

Ken Ogata's collaboration was very helpful — his dedication to his work is either an inspiration or an admonition. Seemingly working all hours of the day and night, producing the silicon nanowire electrodes for the *in situ* NMR experiments was the least of his contributions. More than once we had to break out of the department when we found ourselves locked in after he had stayed helping with the experiments or discussing the results until the small hours of the morning.

Matt Tucker's work as local contact at ISIS, especially in finding solutions to the problems posed by small sample quantities and air-sensitive materials, was indispensable for the neutron scattering experiments.

I would like to thank my supervisors Martin Dove and Clare Grey: Martin for his careful instruction and for the freedom he gave me to pursue my own vision for RMCprofile, and Clare for her patience in dealing with the mountains of paperwork which the University loaded on her in my name.

The discussions I had with Martin and with Anthony Phillips were very helpful in the design and implementation of RMCprofile, while their contributions to other parts of the code base meant I had more time for the improvements discussed in this dissertation. Matt Tucker and Martin Dove were both helpful in the discussions that led to the development of ProfFitS. While ProfFitS does not contain any code from MCGRtof, having access to the MCGRtof code and to some sample input and output was very helpful in the development process, so I should thank Martin for making this available to me.

Adam Best of CSIRO must be credited with the suggestion to use a glue gun to seal the bag cells over the copper mesh current collectors, and with helpful discussions about minimising the use of expensive d4-EC in the deuterated electrolyte for neutron scattering experiments.

Contents

1	Introduction	1
1.1	Battery composition	4
1.1.1	The choice of electrode material	4
1.1.2	Current lithium-ion batteries	6
1.1.3	Electrolytes	7
1.1.4	Lithium anode materials	8
1.2	Silicon in lithium-ion batteries	11
1.2.1	Lithium-silicon binary compounds	11
1.2.2	Electrochemical reactions with lithium	11
1.2.3	Pulverisation due to electrochemical shock	14
1.2.4	Binders	16
1.2.5	Conducting carbon	18
1.2.6	Silicon nanostructures	19
1.3	Diffraction and total scattering	24
1.3.1	The scattering function	24
1.3.2	Scattering of monochromatic radiation	24
1.3.3	Polychromatic radiation	26
1.3.4	Pair distribution function methods	26
1.3.5	Total scattering	27
1.3.6	Radiation sources	28
1.3.7	Transformation to real space	30
1.4	Reverse Monte Carlo analysis	30
1.4.1	Monte Carlo algorithms	30
1.4.2	Computational limits	31
1.4.3	RMCprofile	32
1.5	Nuclear magnetic resonance	33
1.5.1	Physical basis of NMR	33
1.5.2	Effects of atomic motion	34
1.5.3	Skin depth effects	34
1.5.4	In situ methods	35

1.6	Analysis of NMR data	36
1.6.1	Decomposition into simpler spectra	36
1.6.2	Principal Component Analysis	37
1.6.3	Non-negative matrix factorisation	38
1.6.4	Implementation	39
1.7	Research aims	41
2	Improvements to RMCprofile	42
2.1	Profile-guided optimisation	42
2.2	Build system	43
2.3	Unit testing	43
2.4	Modular architecture	43
2.5	Multiple configurations	44
2.6	Improved compatibility with Condor	45
2.7	Explicit uncertainty information in data files	45
2.8	Functionality that has been removed	46
2.8.1	Automatic calculation of neighbour lists	46
2.8.2	Automatic conversion of DATA_TYPE and FIT_TYPE	46
2.8.3	Temporarily removed functionality	47
2.9	Validation	47
2.9.1	Atom swap moves	47
2.9.2	Bending distortions	49
2.9.3	Heterogeneous mixture	49
2.10	Results of validation runs	50
2.10.1	Atom swap moves	50
2.10.2	Bending distortions	55
2.10.3	Heterogeneous mixture	55
2.11	Conclusions	59
3	Deconvolution of the resolution function	60
3.1	Matrix formulation and linear least-squares solution	61
3.1.1	Ideal case	61
3.1.2	Resolution function	61
3.1.3	Linear least squares solvers	62
3.2	Example: crystalline aluminium phosphate	62
3.3	Results	62
3.4	Discussion	62

4	Neutron diffraction and RMC studies on silicon anode materials	65
4.1	Methods	66
4.1.1	Preparation of active material	66
4.1.2	Assembly of Swagelok cells	66
4.1.3	Electrochemical cycling	69
4.1.4	Extraction of active material	69
4.1.5	Neutron scattering experiments	69
4.1.6	Preliminary data processing	70
4.1.7	RMC calculations	70
4.2	Results	72
4.2.1	Electrochemical performance	72
4.2.2	Raw scattering patterns	74
4.2.3	RMC	76
4.3	Discussion	80
5	In situ NMR experiments on SiNWs	83
5.1	Methods	83
5.1.1	Preliminary tests of substrate suitability	83
5.1.2	Assembly of bag cells	85
5.1.3	In situ NMR	87
5.2	Results	88
5.2.1	PCA analysis	88
5.2.2	NMF analysis	91
5.2.3	Comparison of NMR and PCA results	94
6	Conclusion	95
6.1	Summary of results	95
6.2	Future opportunities	96
6.2.1	Electrolytes	96
6.2.2	Improvements to RMCprofile	96
	Bibliography	98
A	Methods for samples and data provided by others	115
A.1	Materials synthesis	115
A.1.1	CVD-synthesised silicon nanowires and amorphous silicon	115
A.2	Experimental procedures for data	116
A.2.1	MCGRtof data for aluminium phosphate	116

B	Methods for selected experiments not discussed in this dissertation	117
B.1	Preparation of active materials	117
B.1.1	Slurry with CMC binder	117
B.1.2	Mechanosynthesis of lithium silicide model compounds	118
B.2	Cell assembly	118
B.2.1	Coin cells	118
C	Open source programs for file formats used in my research	119
C.1	Arbin file format	119
C.2	Bio-Logic MPR format	120
C.2.1	Header and “VMP settings” block	121
C.2.2	“VMP data” block	123
C.2.3	Timestamp and other data	123
C.2.4	Implementation details	124
C.3	TNMR format	124
D	Availability of software code	126
D.1	ProfFitS	126
D.2	RMCprofile	126
D.3	pytnt	126
D.4	Galvani	127
D.5	NMR PCA and NMF	127

Glossary

a-Si amorphous silicon. 19, 21, 22

AIRSS *ab initio* random structure searching. 11

battery cycler an appliance with electronic circuitry which measures the current through and potential across a battery or other device while passing through it a current or voltage determined by a computer-generated schedule, logging the current, voltage and other variables to a file on the computer. 67, 69, 87, 119, 120, 124

BCC body-centred cubic. 47

BEV battery electric vehicle. 3

brilliance the intensity of radiation per unit area and unit solid angle of convergence or divergence within a particular frequency range. Typically has the units
 $\frac{\text{photons}}{\text{s mrad}^2 \text{ mm}^2 \cdot 0.1\% \text{ BW}}$. 29

BSD Berkeley software distribution. 126

BVS bond valence sum. 47

c-Si crystalline silicon. 20, 21

capacity fade the decrease in the charge capacity of an electrode over the course of repeated cycling. viii, 17

capacity retention the property of an electrode whose charge capacity remains the same over the course of repeated cycling, the absence of capacity fade. 16–18, 41

CF carbon fibre. 18, 20, 83, 85, 96

CFGDL carbon-fibre-based gas diffusion layer. 83, 115

chemical shift the difference between the Larmor precession frequency of a nucleus in a given chemical environment and that in a standard reference environment. 33, 34

CMC carboxymethyl cellulose. 14, 16, 17, 66, 117

Coulombic efficiency the delithiation capacity as a fraction of the lithiation capacity. 11, 14, 17, 20

CPU central processing unit. 42

CV cyclic voltammetry. 21

CVD chemical vapour deposition. 17, 19–21, 41, 115

DEME N,N-diethyl-N-methyl-N-(2-methoxyethyl)ammonium. 8

DFT density functional theory. 11, 20

DMC dimethyl carbonate. 6, 8, 66, 70, 71, 118

EC ethylene carbonate. 6–8, 66

EELS electron energy-loss spectroscopy. 12

EIS electrochemical impedance spectroscopy. 21

EMF electromotive force. xi, 4

EXAFS extended X-ray absorption fine structure. 31, 42, 47, 82

FCEV fuel cell electric vehicle. 3

FFT fast Fourier transform. 61

FID free induction decay. 36, 38, 94

FT Fourier transform. 25–27, 31, 36, 39, 60, 61

galvanostatic constant current. 9, 22

GPL GNU general public license. 126, 127

gravimetric capacity the amount of electrical charge stored by a system, divided by its mass. 8, 10, 16

gravimetric energy density the amount of energy stored by a system, divided by its mass. 10

ICE internal combustion engine. 4

ICP-MS inductively coupled plasma mass spectrometry. 82

initial capacity the capacity of an electrode in the first charge-discharge cycle. 17

instrumental resolution function broadening of peaks from their ideal shapes due to instrumental imperfections. 30

INVERT invariant environment refinement technique. 31

ionic liquid a salt that is liquid (possibly supercooled) at room temperature. 6, 8

irreversible capacity the difference between the lithiation and delithiation capacity on a given cycle. 9, 14, 16

Kapton[®] DuPont's trade name for poly(4,4'-oxydiphenylene-pyromellitimide). 67, 68

LIB lithium-ion battery. 2, 6–9, 11, 17, 19–21, 34

Makefile file, customarily named **Makefile**, containing instructions for the **make** program. 43

Markov chain Monte Carlo an algorithm in which state transitions are random and the probability of transition to any given state depends only on the current state and not on previous states. x, 30, 39

Metropolis Monte Carlo a Markov chain Monte Carlo algorithm in which state transition probabilities are weighted by a Boltzmann factor calculated from the difference in 'energy' between the two states in question. 30, 31, 60

monochromator device for selecting a single wavelength out of a polychromatic beam of radiation. Typically composed of a crystal or pair of crystals aligned so that a strong Bragg peak scatters the desired wavelength in the desired direction and all other wavelengths into a beam stop. 26, 29

Monte Carlo (of an algorithm) making use of random sampling to find an approximate solution to a computationally hard problem. 30, 31, 60

MRI magnetic resonance imaging. 38, 39

Ni-Cd nickel-cadmium. 10

NiMH nickel metal hydride. 4

NMF non-negative matrix factorisation. 38, 39, 88, 91, 94–96, 127

NMR nuclear magnetic resonance. 11, 16, 31, 33–41, 82–85, 87, 88, 91, 95, 96, 119, 123

NP-hard the computational complexity class of problems to which any problem in the ‘NP’ (nondeterministic polynomial time) class can be reduced in polynomial time. 39, 94

NW nanowire. 17, 19–22

OCV open circuit voltage. 69

overpotential the difference, due to factors such as internal resistance, between the actual voltage across a cell and the EMF implied by the thermodynamic free energy of the electrode materials. 6, 9, 13

PC propylene carbonate. 6–8

PCA principal component analysis. 37–40, 88–91, 94, 127

PDF pair distribution function. 27, 31, 65, 70, 71

PFPE perfluoropolyether. 8, 96

precision the number of bits used to store the value of an individual data point in a computer’s memory. 42

PVDF poly vinylidene difluoride. 14, 16–18

RAM random access memory. 32, 42

RF radio frequency. 34, 35

RMC reverse Monte Carlo. 31, 32, 42, 44, 46, 47, 49, 76, 77, 80, 81, 96, 97

SAED selected area electron diffraction. 19

scattering density the chance of radiation (*e.g.* X-rays or neutrons) being scattered from a given point or region of space. 24–27

SEI solid-electrolyte interphase. 7, 8, 19–21, 42, 66, 69–71, 74, 80, 81, 91, 94, 96

SEM scanning electron microscope. 20

SHE standard hydrogen electrode. 6, 7

Si NP silicon nanoparticle. 19

SiNW silicon nanowire. 17, 19–22, 41, 83, 84, 96, 115

SS stainless steel. 83, 85

SVD singular value decomposition. 38

Swagelok cell a cell morphology made from a modified Swagelok[®] pipe fitting. 67–69

TCO total cost of ownership. 3

TEM transmission electron microscope. 11, 20, 21

TFSI bis-(trifluoromethyl sulfonyl) imide. 8

theoretical capacity the amount of electrical charge that can be stored and released by an electrode or other system if the charge storage reaction proceeds quantitatively (to completion) and reversibly. 4–6, 16, 20

ToF time of flight. 30, 32, 60, 62

VEELS valence electron energy-loss spectroscopy. 12

volumetric capacity the amount of electrical charge stored by a system, divided by its volume. 8, 16

volumetric energy density the amount of energy stored by a system, divided by its volume. 10

XPS X-ray photoelectron spectroscopy. 20, 21

XRD X-ray diffraction. 11, 12, 41, 96

Chapter 1

Introduction

People around the world use energy for transport, heating and cooling, lighting, industrial processes, entertainment, and many other uses. (Technically, since energy is a conserved quantity, it is not ‘used’ but rather converted into a less available form *i.e.* waste heat.) The energy consumption for all human activity in the year 2012 was 3.74×10^{20} J [1], which works out as an average power use of 1.7kW per person. Most of this energy originates (ignoring events prior to the formation of the solar system) from nuclear fusion reactions in the Sun and is transmitted to the Earth in the form of light, with a few percent coming from nuclear fission reactions inside nuclear power plants and further small fractions from radioactive decay in the Earth’s interior and the rotational kinetic energy of the Earth (geothermal and tidal power respectively).

Nuclear fission reactors provide a concentrated source of energy, but require a great deal of machinery and protective shielding to extract this energy safely (and indeed not always as safely as could be hoped) and convert it to a usable form. Light from the Sun, on the other hand, is spread out over the Earth’s surface so that not much is available in any one location. In any case, it also needs to be converted if it is to be used for anything other than daytime lighting and heating. For the past two centuries, the majority of the energy used by humanity has been in the form of fossil fuels — energy absorbed by ancient plants or algae, stored in the form of carbohydrates or fats, then buried and converted into simpler hydrocarbons by the action of geological processes over millions of years. These are mined or otherwise extracted from the ground and then burnt to provide heat.

While the rate of extraction of fossil fuels is still growing [1], many of the most accessible deposits have been exhausted and new reserves are only made economical by increasing prices, while the cost of renewable energy generation (*e.g.* solar [2]) has been falling exponentially owing to continued technological advances. On top of these cost pressures, the CO₂ emitted by burning fossil fuels is leading to an increased greenhouse effect [3] and to acidification of the oceans, leading many to call for reductions in fossil fuel use.

Fossil fuels are not only a source of energy but a very convenient way of storing energy and making it available where and when it is needed. Neither nuclear nor any of the forms of renewable energy (other than biofuels, which have their own problems such as competition for land against food crops and urban expansion) have this property. Therefore it is necessary to store energy where and when it is available so that it can be released where and when it is needed. Since most renewable energy technologies generate energy in the form of electricity, and an increasing share of energy consumption is also in the form of electricity [1], storage of electrical energy is considered more and more important. While there are other methods of storing electrical energy, by far the most prominent in everyday life is the rechargeable (also known as ‘secondary’) battery.

Batteries and their uses

A battery is a discrete, encapsulated unit containing one or more electrochemical cells which can be used to supply and/or store electrical power. Although static batteries do exist, the majority of batteries are used as portable sources of electrical power for vehicles, devices or appliances that have to be used in circumstances where mains electricity is unavailable, impractical or even just inconvenient. The requirement of portability means that power density and energy density (both gravimetric and volumetric) are important criteria when choosing between battery chemistries, and indeed between batteries and other portable power sources such as fuel cells, supercapacitors or heat engines.

Portable electronics represent an almost ideal use case for batteries. They contain expensive electronic circuitry that becomes obsolete within a few years, so pressures on cost are relaxed and a cycle life of a few hundred to a thousand charge-discharge cycles is sufficient. They are used almost exclusively in environments tailored for human comfort, thus avoiding extremes of pressure and temperature. Moreover, since portable devices are small, they have a high surface area to volume ratio and therefore the risk of overheating and thermal runaway is reduced. Portable electronics are typically used for a period of a few hours to days and can be left to charge overnight while the user is asleep, so neither fast charging nor fast discharging are needed. If someone needs to go an exceptionally long time without mains power, a backup battery is small and light enough that it can be carried without difficulty. Unsurprisingly, therefore, portable electronics are by far the biggest market for lithium-ion batteries (LIBs) today [4].

Grid-scale electricity storage requires prices far cheaper than today’s batteries [5] combined with high efficiency and an incredibly long cycle life. (Electricity grid infrastructure typically has a design life of several decades.) Although maintenance costs must still be controlled, large centralised facilities can typically afford to hire highly skilled tech-

nicians to maintain and operate their equipment, so the end-user simplicity of battery storage is less of an advantage from their perspective. Currently, 99 % of worldwide grid storage capacity is in the form of pumped hydroelectric energy storage [5]. However, many of the most suitable sites for pumped hydro have already been used, so expanding it to meet the additional requirements posed by large-scale use of intermittent renewables is not feasible. The second most heavily used technology, with 315 MW of installed capacity, is the sodium/sulfur battery [5]. Many other technologies for grid scale storage have been proposed, with compressed air in natural geological caverns being the closest to large-scale use — a 2700 MW facility is under construction in Norton, Ohio [6].

One study [7] based on simulations of the California electricity grid and data on electricity consumption and production in California indicate that 100 % elimination of CO₂ emissions, in the absence of demand management, will require energy storage systems able to store on the order of 1 month of total electricity demand and able to supply 65 % of peak power. On the other hand, Barnhart et al. [8] calculate that it is cheaper to overprovision by building many more wind turbines and solar panels than are strictly necessary, so that they are able to supply enough power even with weak winds and faint sunlight, thus requiring a much smaller amount of energy storage capacity. Even in the latter case, the capacity that would be required to supply power for *e.g.* a windless night in winter is still much greater than the currently installed capacity, so grid energy storage is a very large potential market for batteries.

Electric vehicles must carry their own energy supply around with them, meaning that the weight and volume of batteries are severe disadvantages compared with fossil fuels. The potential for high-speed collisions adds additional design constraints, and even the requirement to function at a wide range of temperatures restricts the range of materials that can be used. For battery electric vehicles (BEVs), a battery large enough to cope with long-distance journeys will be so heavy and bulky as to make the far more numerous short trips much less efficient, not to mention increasing the up-front cost of the battery. Using a smaller battery for long trips would require the ability to recharge in the few minutes it currently takes to refill a tank of petrol, or at most the time it takes to refuel the car's occupants with food and/or caffeinated beverages. A car's design life is on the order of a decade, and the cost of the rest of the car, relative to its energy requirements, is far less than the cost of consumer electronics, so the price of the battery will be a much more significant part of the total product cost.

Modelling of zero net emission vehicle performance and total cost of ownership (TCO) by Contestabile et al. [9] suggests that zero emission vehicles will split between BEVs and fuel cell electric vehicles (FCEVs). BEVs will dominate the market for small cars used only for short trips *e.g.* in cities. FCEVs will be used for larger vehicles and longer

journeys. Hybrids with internal combustion engines (ICEs) powered by biofuels seem unlikely, as applications such as aviation, with its high premium on specific energy, will bid up the price of biofuels to levels where they are no longer competitive for other uses.

While some (*e.g.* [10]) have raised concerns about the world's known lithium reserves not containing enough lithium to replace the world's current stock of petrol and diesel engined vehicles with battery electric vehicles, a more detailed analysis [11] indicates that, assuming used batteries are recycled efficiently, current lithium reserves are sufficient for all new car production until at least 2050.

1.1 Battery composition

An electrochemical cell is conventionally divided into three parts. At one end is the anode, at the other the cathode, and between them is the electrolyte, which is often absorbed into an inert separator. Each of these has its own requirements and challenges from the point of view of materials selection and fabrication. At the anode, an oxidation reaction occurs, releasing electrons which flow through the circuit to the cathode, where they are taken up by a reduction reaction. To balance this flow of charge, positive ions flow through the electrolyte (which conducts ions but not electrons) from the anode to the cathode. (In principle the charge could also be balanced by a flow of negative ions from the cathode to the anode, but this is much less common.)

1.1.1 The choice of electrode material

The energy density of an electrochemical device is the product of its electrical charge density and its electromotive force (EMF), also known as voltage. Therefore, a device with a high energy density will require electrode materials with high charge densities and widely separated electrical potentials. Electrical half cell potentials are hard to predict as they depend on many factors such as the choice of solvent, the temperature and, for practical current densities, any kinetic barriers such as a passivation layer. I will therefore first consider the charge densities available with different elements.

Hydrogen has the highest theoretical charge density of any element, with a theoretical capacity for $\text{H}^+ + \text{e}^- \rightleftharpoons \frac{1}{2}\text{H}_2$ of 26 587 mA h g⁻¹. Unsurprisingly there is a great deal of interest in hydrogen-based electrochemical devices, mainly fuel cells [12]. However, molecular hydrogen is a gas at room temperature, so in order to store appreciable quantities of it it must either be compressed and stored in strong tanks or reacted with another element to form a compound. Indeed, the popular nickel metal hydride (NiMH) battery chemistry can be considered a hydrogen-based electrochemical cell, with the hydrogen reacted to form nickel oxyhydroxide at the cathode and a metal hydride at the anode.

Both of these methods involve energy losses in each direction and also add additional mass which reduces the energy density. Also, currently the electrochemical reduction of H^+ (*e.g.* in the form of H_2O) to give H_2 requires expensive catalysts and is relatively inefficient, although this problem is diminishing every year as new discoveries are made [13].

Carbon has the second highest theoretical capacity — although it is not often found as a single-atom C^{4+} or C^{4-} ion, has compounds with formal oxidation states ranging from +4 to -4, giving a theoretical capacity of 8926 mA h g^{-1} for $\text{C}^{4+} + 4 \text{ e}^- \rightleftharpoons \text{C}$ or $\text{C} + 4 \text{ e}^- \rightleftharpoons \text{C}^{4-}$. The widespread availability of carbon, and compounds of carbon and hydrogen, in the form of fossil fuels (coal, oil and natural gas) make carbon today's most popular form of stored energy [1]. Indeed, petrol is in some ways the ideal energy storage compound as it combines hydrogen, which has the highest gravimetric capacity, with just enough carbon (the element with the second highest capacity) to make it liquid at room temperature and thus easy to store and transport. However, the carbon dioxide released by burning carbon-containing fuels accumulates in the atmosphere and oceans if it is produced faster than natural processes can absorb it, leading to warming of the climate and acidification of the oceans [3]. Reducing CO_2 back into organic carbon, thus using it as an energy storage medium rather than an energy source, is even harder than reducing hydrogen — plants and algae have had hundreds of millions of years of evolution driving them to improve their photosynthetic processes, but the best efficiency they can achieve is a few percent. Moreover, from the point of view of electrochemistry, carbon's strong covalent bonding makes it very hard to develop an electrolyte which could transport C^{4+} or C^{4-} ions. Instead, energy is usually obtained from carbon-containing fuels by burning them in air, with the heat being used to drive a heat engine if mechanical power is needed, and the mechanical output of the heat engine driving an electrical generator if electric power is desired. Most ideas for using carbon-containing fuels in fuel cells either involve reacting the fuel with water to produce hydrogen for a hydrogen fuel cell or using an electrolyte that transmits oxide ions, with the oxidation products remaining on the cathode side [14].

Boron forms covalent compounds rather than isolated ions. Its oxidation states range from +3 to -1, and the notional $\text{B}^{3+} + 3 \text{ e}^- \rightleftharpoons \text{B}$ reaction gives a theoretical capacity of 7438 mA h g^{-1} . Just as with carbon, however, boron's covalency makes it difficult for B^{3+} or B^- to be transported on their own. Boron is more often used in the form of BF_4^- as the counterion to a metal ion electrolyte or with an organic cation in a supercapacitor electrolyte [15]. BH_4^- salts and other boron hydrides have also been proposed as hydrogen storage materials for fuel cells [12].

Beryllium typically forms compounds with an oxidation state of +2, giving it a theoretical capacity of 5948 mA h g^{-1} for the reaction $\text{Be}^{2+} + 2 \text{e}^{-} \rightleftharpoons \text{Be}$. Beryllium electrochemistry appears to be a relatively poorly explored field, with a Web of Knowledge search for “beryllium electrochemistry” returning just 18 results of which only 5 (two journal articles [16, 17] and three conference proceedings) were concerned wholly or mainly with beryllium. Both articles report a high overpotential due to a passivation layer on the surface of the beryllium. Venugopal et al. [17] state that the passivation layer is often assumed to be BeO , but that the lack of thermodynamic data mean that BeH_2 cannot be ruled out. This high overpotential, combined with beryllium’s toxicity, rule out beryllium as an electrode material for electrochemical energy storage.

Nitrogen has a theoretical capacity of 5740 mA h g^{-1} for the reduction of nitrogen gas to nitride: $\frac{1}{2} \text{N}_2 + 3 \text{e}^{-} \rightleftharpoons \text{N}^{3-}$. The nitrogen reduction reaction, and the reverse oxidation, have been demonstrated at 783 K by Ito and Goto [18] using a molten salt electrolyte. They report that both reactions proceed “almost quantitatively” with a half cell potential of $0.382 \text{ V vs Li|Li}^{+}$. Progress [19] has been made on solid electrolytes for N^{3-} ions, but all those developed so far only function at high temperatures. Nitrogen is, of course, a gas, but it is abundant in the air so only the nitride (which would be a solid, or a liquid at high temperature) would need to be stored. A more significant problem with using nitrogen for electrochemical energy storage is that, since the element is the low-energy phase and the salt is the high-energy phase, the nitride salt is potentially vulnerable to spontaneous decomposition, depending on the choice of cation.

Lithium has a theoretical capacity of 3861 mA h g^{-1} for $\text{Li}^{+} + \text{e}^{-} \rightleftharpoons \text{Li}$. In water (*i.e.* $\text{Li}^{+}(\text{aq}) + \text{e}^{-} \rightleftharpoons \text{Li}(\text{m})$), lithium has the lowest standard electrode potential of any element, at $-3.040 \text{ V vs the standard hydrogen electrode (SHE)}$ [20]. The next highest is caesium at -3.027 V for $\text{Cs}^{+}(\text{aq}) + \text{e}^{-} \rightleftharpoons \text{Cs}(\text{m})$ [20]. However, this ordering is due to the very high solvation enthalpy of the Li^{+} ion in water, with K, Rb and Cs all being more reducing than Li in many other solvents, including propylene carbonate (PC) [20] and the ionic liquid N-butyl-N-methylpyrrolidinium bis(trifluoromethylsulfonyl)imide ($[\text{C}_4\text{mPyrr}]^{+}[\text{NTf}_2]^{-}$) [21]. Results are not reported for the mixture of ethylene carbonate (EC) and dimethyl carbonate (DMC) commonly used as an electrolyte solvent for LIBs today, but presumably the ordering is the same as for PC.

1.1.2 Current lithium-ion batteries

Most lithium-ion batteries currently on the market have a graphite anode, a nonaqueous electrolyte containing organic carbonates, and a LiCoO_2 cathode [4]. This combination was first reported by Ohzuku et al. [22], and was commercialised by Sony in the early

1990s; Nishi [23] gives an interesting account of the commercialisation process. LiCoO_2 was first proposed as a cathode material by Mizushima et al. [24]. The reaction of lithium with graphite at high temperatures was first reported by Herold [25] in 1955, and Juza and Wehle [26] showed that the layered compound LiC_6 is the result. Initial attempts to carry out this reaction electrochemically were unsuccessful due to the decomposition of the electrolyte on the graphite surface [27] and it was not until the 1980s that appropriate electrolytes were found [28], leading eventually to the development of the graphite/ LiCoO_2 cell mentioned above.

Scrosati [29] said (in 1999) that “a major change in LIB anode materials is expected in the near future” as electronics require lower voltages, allowing anode materials with thermodynamic stability in the electrolyte. He suggests $\text{Li}_4\text{Ti}_5\text{O}_{12}$ as a promising anode material. He was also optimistic about replacing the LiCoO_2 cathode with cheaper, more environmentally friendly materials based on nickel or manganese oxides.

1.1.3 Electrolytes

Since anode materials are the topic of this dissertation, I will not consider cathode materials in any great detail. However, since the electrolyte is in direct contact with the anode, it must therefore be chemically compatible with the anode (and also the cathode) in order for the battery to function. I will therefore give a brief overview of the available options for electrolytes and the criteria for choosing one.

Most battery chemistries that were developed before Li-ion use aqueous electrolytes. However, the extreme reducing power of lithium (at -3.04 V *vs* the SHE) and other Li-ion anode materials is incompatible with protic solvents such as water. The drive for larger potential windows, and thus higher energy densities, led to research in aprotic electrolyte solvents.

A good electrolyte solvent must be able to solvate the electrolyte salt, and the solvated Li^+ ions must have a high mobility. The former requirement correlates with a high dielectric constant, and the latter with a low viscosity. The solvent must also either not react with the electrode materials at all or react in such a way as to form a stable barrier layer on the surface of the electrode which prevents further solvent decomposition. Such a barrier layer is known as a solid-electrolyte interphase (SEI). The electrolyte must also remain liquid over the temperature range in which the battery is supposed to operate, and it must not present insuperable fire or toxicity hazards.

Early research with lithium metal anodes in the 1960s and 1970s tended to use propylene carbonate (PC) as the solvent [30]. However, problems with dendrite formation led to a switch to ether-based electrolytes [30], although these had problems with decomposition on the cathode. Early graphite-based Li-ion cells used PC, but then Fong et al. [28] showed that ethylene carbonate (EC) forms a good SEI on the surface of graphite,

while PC tends to intercalate between the graphite layers and cause exfoliation. EC has a melting point of 36.4 °C, so it must be mixed with a lower-melting solvent to give an electrolyte that is liquid at room temperature. Today, the most common [30] LIB electrolyte solvent is a mixture of EC and one or more linear carbonates such as dimethyl carbonate (DMC).

Ionic liquids have received much research interest as electrolytes for LIBs because of their low flammability and high voltage stability window. However, even ionic liquids with broad stability windows such as DEME-TFSI will decompose at low voltages *vs* Li|Li⁺. Adding a few % of carbonate electrolyte solvents to ionic liquid electrolytes will form a good SEI [31].

Wong et al. [32] recently discovered that perfluoropolyethers (PFPEs) have a very high Li⁺ transference number of 0.91, and function well as electrolytes for LIBs. Because they contain no hydrogen, PFPE electrolytes would be particularly suitable for preparing samples for neutron total scattering experiments as they would not require deuteration.

1.1.4 Lithium anode materials

Lithium metal obviously has the highest gravimetric capacity and lowest electrochemical potential of any possible lithium-ion battery anode material. Those who claim that silicon has a higher gravimetric capacity, such as Arico et al. [33], have confounded two different definitions of gravimetric capacity (also known as specific capacity), in particular including the mass of the lithium when calculating the capacity for pure lithium metal (which would otherwise be infinite) but not when calculating the capacity for silicon or other materials. Regarding the electrochemical potential, any material with a lower potential than Li|Li⁺ and enough ionic and electronic conductivity to act as an LIB electrode would spontaneously decompose into lithium metal and the delithiated anode material. Interestingly though, lithium metal does not have the highest volumetric capacity, as several intermetallic compounds (including the silicon compounds Li₂₁Si₅, Li₁₅Si₄ and even Li₁₃Si₄) have more lithium atoms per unit volume than pure lithium metal despite the presence of additional atoms (see Table 1.1).

So it seems obvious that lithium metal would be the material of choice for LIB anodes. Unfortunately, lithium metal has a tendency to plate unevenly when electrodeposited, leading over time to the formation of dendrites which can cause short circuits by penetrating through the separator and forming an electrical contact with the cathode [34].

Adding salts of metals which can alloy with lithium (see section 1.1.4), such as Al³⁺ or Sn²⁺, to the electrolyte used with a lithium metal anode [35] can cause alloy formation in the incipient dendrites, suppressing further dendrite growth. However, the alloy layer does not dissolve back into the electrolyte on discharge, meaning that the salts are eventually used up on repeated cycling, after which dendrite formation resumes. Ding et al. [36]

showed that adding low concentrations of Cs^+ or Rb^+ to the electrolyte can suppress dendrite formation by screening the charge of the dendrite tip without being incorporated into the solid phase, thus avoiding this depletion.

Another way of suppressing dendrite growth is pulsed charging, which has been shown by Mayers et al. [37] to reduce dendrite formation relative to galvanostatic charging with the same average current.

Intercalation materials have a structure with enough empty space and/or flexibility to allow ions to be inserted and removed without rearranging the host atoms. Commonly they are anisotropic and allow ionic motion only within the planes between layers in the material, or alternatively only within one-dimensional ‘columns’ of ion sites.

The vast majority [4] of commercial lithium-ion batteries today are based on the so-called “rocking-chair” chemistry of graphite anode and lithium cobalt oxide cathode. Both graphite and LiCoO_2 are layered materials, and the lithium ions can reversibly intercalate between the layers with simultaneous oxidation or reduction of the host material to maintain overall charge neutrality.

Many other intercalation materials are the subject of research interest as possible LIB electrodes, but most of these (such as LiFePO_4 , LiMn_2O_4 and their derivatives) are being considered as cathode materials. However, one layered oxide, $\text{Li}_4\text{Ti}_5\text{O}_{12}$, is being considered as an anode [38]. Its voltage *vs* $\text{Li}|\text{Li}^+$ of 1.55 V [39] is higher than those of graphite or silicon, which gives a lower energy density but on the other hand drastically reduces the problems of electrolyte decomposition and dendrite formation [38].

Conversion materials (also referred to as ‘displacement’ materials) react along the general scheme:



with MX_n being a salt of metal M and counterion X. The reduced metal is typically formed as very small nanoparticles that ensure that MX_n can re-form on delithiation.

Although conversion materials can (at least in theory) achieve much higher capacities than intercalation materials, without the huge volume changes of alloy materials, they suffer from high overpotentials which make energy storage very inefficient and lead to heating on charge and discharge. It is thought that the reason for this overpotential is the high surface energy of the metal nanoparticles [40]. Conversion materials typically also have a very large irreversible capacity in the first cycle [40]. Finally, although the volume changes are smaller than in alloy materials, they can still be enough to cause mechanical degradation.

Alloy materials are conceptually the simplest of electrode materials — an element reacts reversibly with lithium to form a binary compound. Typically the name ‘alloy material’ is used only for anode materials, with single-element cathode materials such as sulfur or oxygen not included under this classification.

Many different elements have been investigated for use as alloy electrode materials. Silicon, aluminium and magnesium are popular because they are abundant in nature and also relatively light, leading to high gravimetric capacities. Heavier elements such as tin and antimony have also been considered, particularly for applications where volumetric energy density is more important than gravimetric energy density. Tin is the only alloy electrode material which has so far been commercialised, in the form of Sony’s Nexelion [41].

Typically the reaction of lithium with alloy materials entails very large volume changes (*e.g.* 281 % for $4\text{Si} \longrightarrow \text{Li}_{15}\text{Si}_4$) which can in turn lead to problems with the mechanical integrity of the electrode. The volume change typically does not proceed continuously and uniformly over the entire electrode; instead some regions are lithiated faster than others and the resulting strain leads to a phenomenon analogous to thermal shock [42]. However, large volume changes have not proved insuperable barriers to commercialisation of other battery chemistries such as lead-acid (120 % for $\text{Pb} \longrightarrow \text{PbSO}_4$) [43] or nickel-cadmium (Ni-Cd) (130 % for $\text{Cd} \longrightarrow \text{Cd}(\text{OH})_2$) [43].

1.2 Silicon in lithium-ion batteries

Since silicon is the subject of this dissertation, I will now discuss its use in lithium-ion batteries in greater detail.

1.2.1 Lithium-silicon binary compounds

Lithium is generally thought to form four thermodynamically stable binary compounds with silicon [44], namely $\text{Li}_{12}\text{Si}_7$, Li_7Si_3 (also referred to as $\text{Li}_{14}\text{Si}_6$), $\text{Li}_{13}\text{Si}_4$ and $\text{Li}_{21}\text{Si}_5$. The $\text{Li}_{21}\text{Si}_5$ phase was formerly thought to have the composition $\text{Li}_{22}\text{Si}_5$, analogous to $\text{Li}_{22}\text{Pb}_5$, but was subsequently shown [45] to be $\text{Li}_{21}\text{Si}_5$. More recently, Zeilinger et al. [46] have found evidence that the $\text{Li}_{21}\text{Si}_5$ phase is actually $\text{Li}_{17}\text{Si}_4$, with a possible non-stoichiometry ranging down to $\text{Li}_{16.42}\text{Si}_4$ [47]. There are also several metastable phases which can be isolated at room temperature, including LiSi [48] and $\text{Li}_{15}\text{Si}_4$ [49].

All the above cited published structures of thermodynamic lithium silicide phases were determined with X-ray diffraction (XRD), and a literature search in July 2014 revealed no articles with neutron diffraction data on lithium silicides. Thus, because of lithium's low Z , the positions of the lithium atoms in the crystal structures are perhaps not as well-defined as they could be. In any case, variable-temperature multidimensional NMR experiments [50] show that the lithium atoms are able to diffuse between different crystal sites at room temperature and only become immobile when cryogenically cooled.

The lithium-silicon binary system has also been explored computationally through density functional theory (DFT) calculations [51, 52]. Exploration of the possible structures of lithium defects in silicon using *ab initio* random structure searching (AIRSS) by Morris et al. [53] showed that interstitial lithium can couple with defects in the silicon crystal structure, with the $\{4\text{Li}, V\}$ complex being particularly stable. As well as indicating a possible mechanism for the initial lithiation of silicon, this also suggests that it will be very difficult to remove the last few lithium atoms from the defect sites in the amorphous silicon network formed during delithiation, offering a partial explanation for the low Coulombic efficiency in the first cycle.

1.2.2 Electrochemical reactions with lithium

Electrochemical cycling of silicon against lithium at high temperature [55] shows distinct voltage plateaux for each of the thermodynamic phases. However, cycling at room temperature [56] shows only a single plateau at around 100 mV *vs* $\text{Li}|\text{Li}^+$ on the first discharge, with a final capacity of approximately 3500 mA h g⁻¹. XRD and transmission electron microscope (TEM) studies by Limthongkul et al. [57] showed that the phase formed during this single plateau is an amorphous lithium silicide with approximate composition $\text{Li}_{2.17}\text{Si}$.

REDACTED - these images are derived from copyrighted information in the Inorganic Crystal Structures Database

Figure 1.1: Single unit cell of the crystal structure of $\text{Li}_{15}\text{Si}_4$, taken from Kubota et al. [54] (ICSD code 159397), seen along the $[1\ 0\ 0]$ crystal axis. Silicon atoms in grey, lithium in purple. The three images show a view along the $[1\ 0\ 0]$, $[1\ 1\ 0]$ and $[1\ 1\ 1]$ axes respectively. The space group is $I\bar{4}3d$, giving a cubic unit cell with $a = 10.60\ \text{\AA}$. The silicon atoms are entirely surrounded by lithium, with no covalent Si–Si bonding present. The distance between adjacent lithium atoms is much shorter than in metallic lithium, to the extent that there is more lithium in a given volume of $\text{Li}_{15}\text{Si}_4$ than in the same volume of pure lithium, despite the presence of the additional silicon atoms.

REDACTED - these images are derived from copyrighted information in the Inorganic Crystal Structures Database

Figure 1.2: Single silicon atom (grey) from the $\text{Li}_{15}\text{Si}_4$ crystal structure [54], together with surrounding lithium atoms (purple), seen from two different angles. The local arrangement of the twelve nearest-neighbour lithium atoms is similar to a distorted hexagonal close-packed structure. The Li–Li and Si–Li nearest neighbour distances are both approximately $2.7\ \text{\AA}$

They named this process “electrochemically-driven solid state amorphization” and rationalise it as the large and complex unit cells of the thermodynamic lithium silicide phases, which are very different to the unit cell of crystalline silicon, presenting an excessive nucleation barrier. Subsequently, *ex situ* XRD by Obrovac and Christensen [49] and *in situ* XRD by Hatchard and Dahn [58] demonstrated that room temperature cycling forms the metastable $\text{Li}_{15}\text{Si}_4$ phase, which crystallises at a voltage of 30 mV to 50 mV *vs* $\text{Li}|\text{Li}^+$.

By contrast, valence electron energy-loss spectroscopy (VEELS) work by Danet et al. [59] suggested a composition of $\text{Li}_{2.9}\text{Si}$ for the amorphous lithiation product. They list several advantages of VEELS over previously used techniques such as XRD and core-loss electron energy-loss spectroscopy (EELS).

The voltage profile of the delithiation process displays a hysteresis effect [60]. If the voltage goes below $\sim 50\ \text{mV}$, so that crystalline $\text{Li}_{15}\text{Si}_4$ is formed, then the delithiation process has one plateau at 500 mV, but if the voltage stays above 50 mV then there are two plateaux at $\sim 400\ \text{mV}$ and $\sim 500\ \text{mV}$. This is explained [60] by the presence of residual Si–Si bonds in the amorphous phase facilitating the delithiation process (and thus lowering the voltage) by providing nucleation points for silicon clusters — in the crystalline $\text{Li}_{15}\text{Si}_4$ all the Si–Si bonds have been broken and only isolated silicon ions remain.

The final product of this delithiation process is amorphous silicon with some residual lithium defects [53]. Subsequent lithiation processes show two voltage plateaux at $\sim 250\ \text{mV}$ and $\sim 100\ \text{mV}$. It is thought [60] that the higher voltage plateau corresponds

to the amorphous silicon network breaking up into clusters to form a phase similar to $\text{Li}_{12}\text{Si}_7$ (although forming the exact $\text{Li}_{12}\text{Si}_7$ structure would be very unlikely given its highly ordered nature). The second plateau corresponds to breaking up these clusters to give isolated Si^{4-} ions or small ‘dumb-bell’ Si_2^{6-} clusters. (The 4– and 6– are notional charges — in practice the electron density would be delocalised across the surrounding lithium atoms to a significant extent.) The lithiation of crystalline silicon, on the other hand, does not form the large clusters, possibly because the activation energy for breaking so many atoms away from an ordered crystal at once is too high, and so there is a single voltage plateau corresponding to formation of the ‘isolated ions and dumb-bell clusters’ phase.

Overall, silicon’s low voltage *vs* $\text{Li}|\text{Li}^+$ is good from the perspective of energy density, but means that a relatively small overpotential (as might be found on fast charging) will lead to plating of lithium metal and possible dendrite formation. Goodenough [61] points out that this restricted charging rate will not be an obstacle to use in portable electronic devices, nor to electric vehicles used for daily commuting which can be left plugged in for

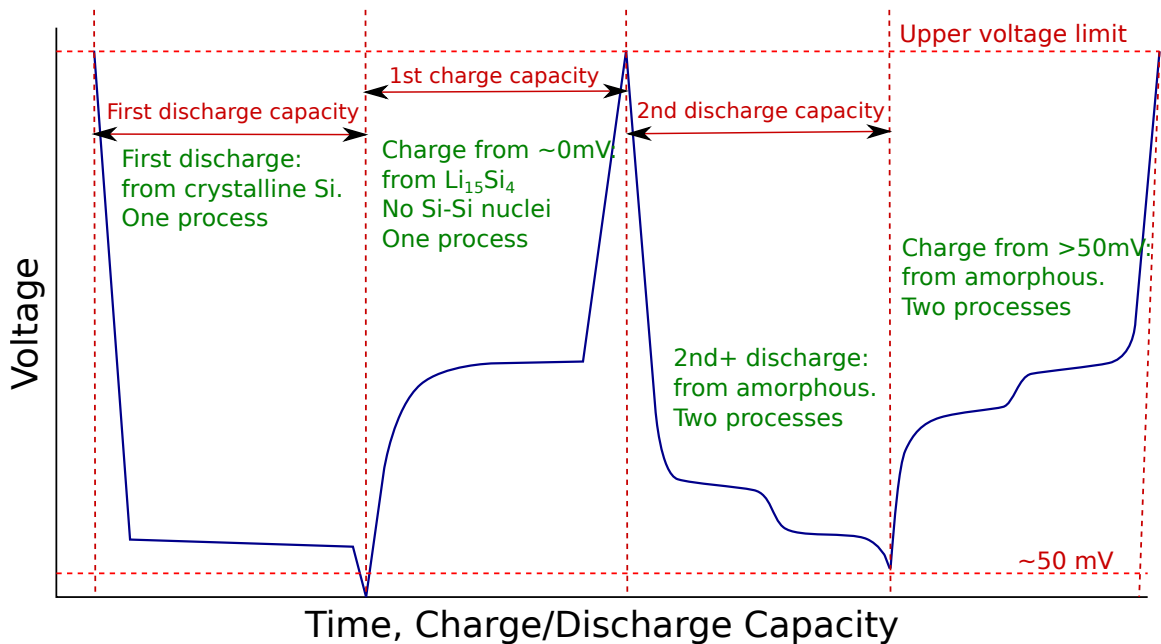


Figure 1.3: Annotated diagram of a typical (*i.e.* stylised, not from experimental data) voltage/capacity graph for the electrochemical lithiation (discharge) and delithiation (charge) of a silicon-based electrode. The first discharge (lithiation) shows a single plateau at around 100 mV, with subsequent discharges showing two gently sloping plateaux at ~ 250 mV and ~ 100 mV. The voltage profile on charge (delithiation) depends on the minimum voltage reached on discharge — if the voltage went below ~ 50 mV there is a single plateau at around 500 mV (shown here in the first charge), whereas if the voltage stayed above 50 mV there are two plateaux at ~ 400 mV and ~ 500 mV (shown in the second charge).

long periods between journeys.

1.2.3 Pulverisation due to electrochemical shock

The reaction of silicon to form lithium silicide causes a large volume expansion (281 % from crystalline silicon to $\text{Li}_{15}\text{Si}_4$ — see Table 1.1 for more data). The delithiation reaction, of course, involves a corresponding reduction in volume. This expansion and contraction does not happen simultaneously over the whole electrode, leading to large strains at the interface between lithiated and delithiated material. These strains in turn lead to cracking and, in time, complete pulverisation and loss of electrical connectivity [62, 63]. The loss of electrical connectivity causes a large irreversible capacity and a rapid capacity fade.*

In the case of anode materials with a low melting point, such as gallium [69], this cracking is not a major problem as the cell temperature can simply be raised above the melting point of the anode material and it will flow together, healing all the cracks. However, the melting point of silicon is 1414 °C, and the lowest liquidus point of any lithium-silicon alloy is 590 °C [44], so this approach is not feasible for the lithium-silicon system.

Several approaches have been proposed to limit the volume changes on cycling or to reduce their deleterious effects. The simple step of limiting the extent of lithiation [70] so as to reduce the total volume change gives a substantial improvement in Coulombic efficiency. Kasavajjula et al. [71] calculate that, above a specific capacity of $\sim 1200 \text{ mA h g}^{-1}$, the anode mass is so small compared to the masses of the other battery components (if using currently available cathode materials *etc.*) that further increases in anode specific capacity will give negligible further increases in overall energy density. Given that $\text{Li}_{15}\text{Si}_4$ has a theoretical capacity of 3579 mA h g^{-1} , there is ample opportunity for range limiting to be used without adversely affecting the overall energy density.

Going beyond the use of pure silicon anodes, several approaches have been tried with the aim of improving cycle life and Coulombic efficiency at the expense of a lower theoretical capacity. Kasavajjula et al. [71] review a number of different active and inert filler materials combined with silicon by ball milling, electroless deposition or pyrolysis. Much research nowadays uses mixtures of silicon powder, conducting carbon particles and a polymer binder such as poly vinylidene difluoride (PVDF) or carboxymethyl cellulose (CMC).

* It was surprisingly hard to find references that present experimental evidence for this well-known fact. For most such cases, simply following the references from another article in the field eventually leads to the original experiment. However, in the case of electrochemical pulverisation of silicon, this reference-following process often ends up at a dead end. Many authors cite articles on electrochemical pulverisation in tin such as [64] or general theoretical treatments of pulverisation such as Huggins and Nix [65]. Some cite articles such as Beaulieu et al. [66] or Graetz et al. [67] which demonstrate silicon nanostructures that, unlike bulk silicon, do not undergo pulverisation. Others simply pick an old paper about lithium-silicon electrochemistry such as Boukamp et al. [68] from 1981.

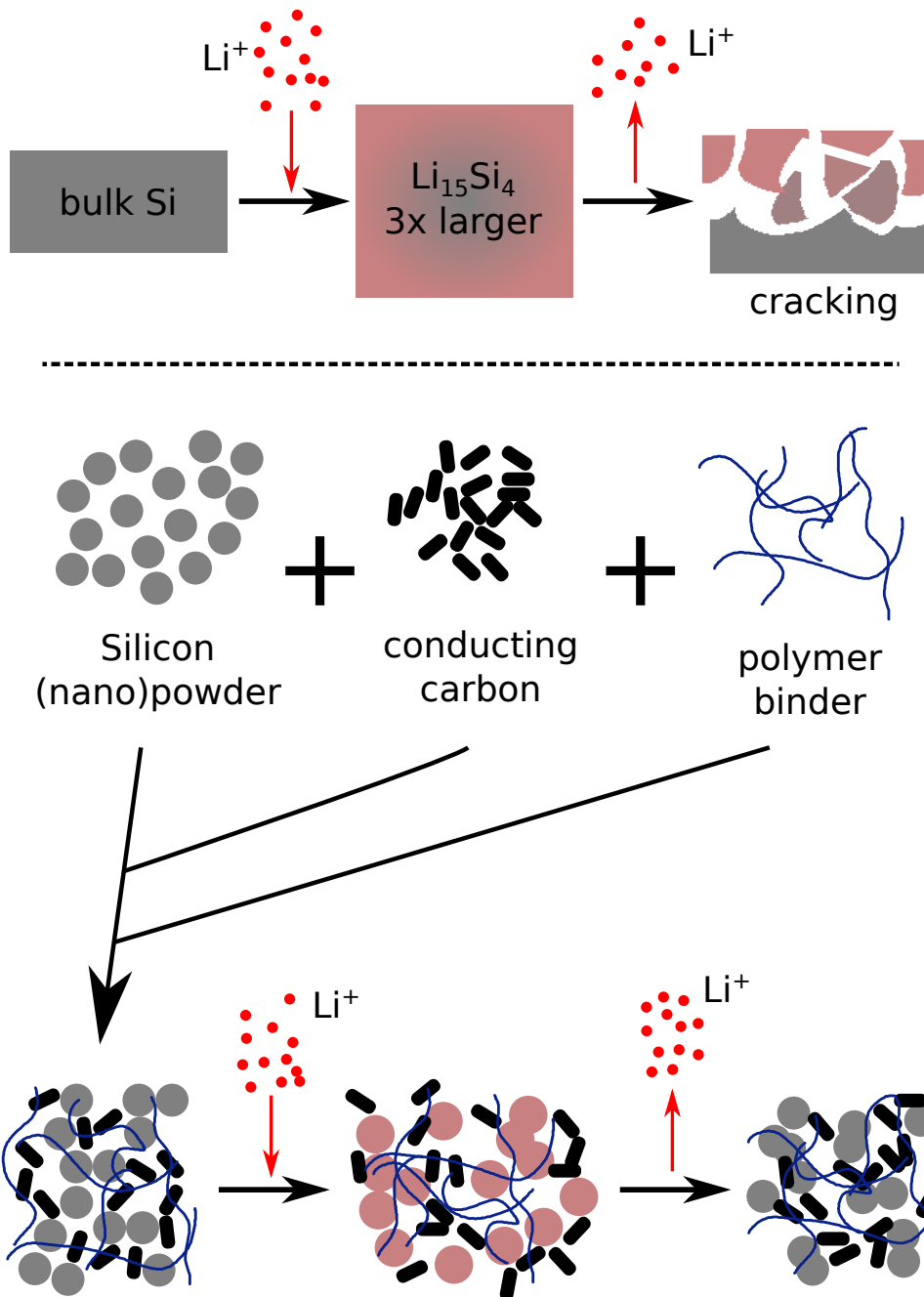


Figure 1.4: Illustration of the advantages of silicon-carbon-binder composite electrodes over bulk silicon. Below a critical particle size, lithiation and delithiation of the silicon particles occurs without mechanical degradation. The carbon filler provides an electrically conductive pathway, while the binder holds the composite together mechanically.

1.2.4 Binders

Materials which have the chemical and electronic properties needed for an electrode typically do not have the mechanical properties required to hold the electrode together and ensure that there is a continuous conductive pathway for both ions and electrons. This is particularly true when the active material is in the form of a fine powder, and when the active material's electronic conductivity is so low that additional conducting filler (see subsection 1.2.5) is required to transmit the electronic current. In these cases, an additional inactive constituent, whose function is solely or mainly to ensure mechanical integrity, is added to the electrode formulation. This additive is known as a binder, because it binds the particles of active material together into a coherent whole.

In commercial batteries, organic polymers such as poly vinylidene difluoride (PVDF) are the most common binder materials, typically added at a mass fraction of a few percent. However, silicon anodes with PVDF binders typically have poor capacity retention. Carboxymethyl cellulose (CMC) has been shown to give better capacity retention than PVDF.

Bridel et al. [72] conducted a systematic investigation into the effects of CMC (in the form of Na-CMC, Li-CMC and K-CMC), amylose, chitosan, heparin and poly-acrylic acid binders on Si, Ge, Sn and Sb electrodes. The article provides incorrect structures for CMC, chitosan and heparin, depicting them as polymers of substituted galactose units linked by $\alpha(1 \rightarrow 4)$ glycosidic bonds, whereas in reality they are formed from $\beta(1 \rightarrow 4)$ linked glucose.

Of the polymers tried, CMC gave the best capacity retention at over 90 % of theoretical capacity after 20 cycles, compared to ~ 20 % for amylose, the next best performing binder. A mixture of silicon, conducting carbon and CMC in a 1:1:1 ratio was found to give best performance, with excess silicon leading to high irreversible capacity, excess carbon lowering the capacity by adding bulk, and excess CMC both adding bulk and adding to the internal resistance. Although this formulation provides a very high gravimetric capacity, the electrodes produced are highly porous and thus have a relatively low volumetric capacity.

Attempts to obtain thick electrode layers and thus a high capacity per unit area were often frustrated by the slurry cracking as it was dried. Freeze-drying was found to be an effective solution to this problem [73].

Electrodes formulated with Li-CMC binders performed worse than those formulated with Na-CMC or K-CMC [72]. Bridel et al. [72] hypothesise that Li^+ binds too tightly to the carboxylate groups, meaning that in solution the CMC chains remain coiled in discrete units rather than extending and interacting with the other chains. On drying this results in a weaker and less well connected binder matrix.

Nuclear magnetic resonance (NMR) experiments showed no evidence of covalent bonding between the CMC and the Si surface [72], but was consistent with hydrogen bonding.

Functionalising the Si surface with bulky alkyl groups which sterically hinder interactions between the CMC matrix and the surface $-OH$ functionality of the Si particles drastically reduced the capacity retention relative to unmodified Si. The opposite approach of functionalising the surface of the Si particles with $-NH_2$ groups and reacting to form strong covalent amide bonds between the Si particles and the CMC matrix gave even worse performance, with a lower initial capacity and a faster capacity fade. Bridel et al. therefore propose that hydrogen bonding between the CMC matrix and the surface $-OH$ groups on the silicon is crucial to the process by which the CMC binder ensures reversibility and capacity retention. They also propose that residual trapped water in the CMC matrix facilitates a self-healing process by locally disrupting the hydrogen bonds, allowing them to break and re-form with the chains in a slightly different position. This is supported by experiments showing that completely eliminating water from a CMC-based electrode by heating for 12 h at $150^\circ C$ *in vacuo* gives much worse capacity retention than electrodes which have been dried less thoroughly [73]. However, they provide no explanation for how residual water and the labile H atoms necessary for hydrogen bonding are retained in the strongly reducing environment of a LIB anode.

Kovalenko et al. [74] demonstrated that alginate, a naturally carboxylated polysaccharide extracted from algae, performs even better than CMC as a binder for silicon electrodes. They achieved good capacity retention and Coulombic efficiency with a 12:4:3 Si:C:alginate mixture, *i.e.* twice as much silicon by weight as the 1:1:1 proportions needed for CMC. With restrictive cycling conditions they reported 1200 mA h g^{-1} and 99.9% Coulombic efficiency after 1250 cycles, but even at high currents and deep discharge the capacity retention was $\sim 90\%$ after 100 cycles. Kovalenko et al. reiterate the importance of electrode porosity and noncovalent interactions between silicon and binder as expressed by Bridel et al. [72], adding that the binder must be impermeable to the electrolyte solvent (to prevent decomposition on the anode surface) yet allow diffusion of Li^+ . They also emphasise that high viscosity of the aqueous slurry is essential to avoid particle aggregation and sedimentation, ensuring a uniform distribution.

By analogy to the advantages that silicon nanowire (SiNW) anodes deposited by chemical vapour deposition (CVD) on metal substrates (see subsection 1.2.6) get from the good electrical connection provided by alloying at the base of the nanowires, Joyce et al. [75] hypothesised that metallic copper deposited on the surface of silicon particles could act as both a conducting filler (see subsection 1.2.5) and as a mechanical binder. They used a modified electroless deposition protocol, omitting the chelating agent which is usually added to ensure an even coating, because they wanted an uneven and incomplete coating of copper on the surface of the particles. The copper-silicon composite was then used as an anode without any further additives. The high conductivity of copper led to a low internal resistance, but capacity retention was no better than simple Si-PVDF compos-

ites. This is by contrast to previous copper-silicon composites produced by Kim et al. [76], who coated the silicon particles with conventional conformal electroless deposition, annealed at up to 800 °C to ensure complete reaction to form Cu_3Si , then added PVDF and conducting carbon to form an anode composite. This approach had poor capacity retention.

1.2.5 Conducting carbon

Pure silicon has a relatively low electrical conductivity, around 0.1 S m^{-1} at 20 °C, and this conductivity only increases slightly on lithiation [77, 48]. To reduce the internal resistance, therefore, most formulations for silicon-based anode materials, and indeed most electrode formulations for any active material which does not itself have high electrical conductivity, include some kind of conducting filler. Carbon powder is the material most often used for this role, as it is cheap, unreactive, has a low density and a moderately high conductivity.

Many researchers have gone further in using nanostructured carbon materials to improve cycle life or allow less carbon (and thus more active material) to be used.

One particularly promising avenue for enquiry is carbon-based composites which have enough mechanical strength and electrical conductivity, allowing them to be used without a separate supporting substrate / current collector. This is particularly important for anode materials, as aluminium (which is used commercially as the cathode current collector) reacts with lithium at the low potentials found at the anode, meaning that heavier metals such as copper must be used instead.

Kercher et al. [78] claim to be the first to use carbon fibre (CF) as a freestanding current collector. They also claim that the low thermal conductivity of binders and conducting carbons used in conventional electrode composites leads to an increased risk of thermal runaway, whereas the higher thermal conductivity of CF-based composites reduces this risk by dissipating excess heat. Martha et al. [79] also make this claim in an article reporting the use of graphitised CF as current collector for a LiFePO_4 cathode. They cite a paper with the same first author [80] as their only evidence in support of this claim, but the cited paper does not even mention thermal conductivity let alone demonstrate that the thermal conductivity of binders and/or conductive carbons is an important factor in thermal runaway.

Snyder et al. [81] investigated several commercial carbon fibre fabrics, papers, mats and so on as electrode materials in their own right, and found that they have an electrochemical capacity approximately half that of pure graphite. This means that if carbon fibre is used as a current collector and mechanical support, it will also add to the electrochemical capacity, at least if the voltage range used in the cell extends low enough to lithiate the carbon.

1.2.6 Silicon nanostructures

Theoretical analysis by Woodford et al. [42] showed that mechanical degradation under electrochemical cycling will not occur below a characteristic particle size which depends on the Vegard coefficients of the electrode material. Consequently there has been interest in electrodes based on nanostructured silicon. The simplest expedient of using very fine silicon powder makes it difficult to ensure a continuous electrically conductive pathway, while the large surface area of the fine powders leads to production of excessive amounts of SEI. Several attempts have been made to mitigate these problems by the use of more advanced nanostructures.

Holzapfel et al. [82] reported improved electrochemistry for nanoparticulate silicon formed by pyrolysis of silane. They also report that the nanoparticulate silicon composites produce less gas from electrolyte decomposition than graphite-based anodes produce.

Others have used rationally designed nanostructures such as core-shell particles or nanowires (NWs). Most ordered silicon nanostructures for LIB work are created by processes such as CVD which require expensive equipment and have low yields. Zhao et al. [83] have developed a wet chemical method for making nanoporous silicon powder, but even this method is less than ideal as it uses dangerous reagents such as HF and H₂O₂.

Magasinski et al. [84] used CVD to deposit Si nanoparticles into the pores of sub-micron carbon black particles, then joined those particles into larger granules by further CVD of carbon, enhancing electrical connectivity and reducing the hazard from dispersion of particles in the air and subsequent inhalation. These granules performed well at high currents, with specific capacity of 850 mA h g⁻¹ at a current of 3 A g⁻¹.

Cui et al. [85] deposited amorphous silicon (*a*-Si) by CVD onto carbon nanofibres, obtaining an overall charge capacity of 2000 mA h g⁻¹. The C-Si core-shell nanofibre anodes had a capacity retention of 93% after 80 cycles, which Cui et al. describe as “good cycling life”.

Kim et al. [86] produced monodisperse silicon nanoparticles (Si NPs) by solvothermal synthesis with inverse micelles. The particle size can be tuned by changing the alkyl chains on the surfactant — the size with the best electrochemical performance was found to be 10 nm.

Gowda et al. [87] coated a nanostructured nickel substrate with a conformal layer of silicon by CVD. The resulting electrode had performance similar to thin films on flat substrates, but with the higher areal density allowed by the porosity and surface roughness.

The first Li-ion electrochemical cell using silicon nanowires (SiNWs) was reported by Zhou et al. [88]. Intriguingly, and conflicting with many later results, selected area electron diffraction (SAED) seems to show re-forming of crystalline Si on delithiation. The article mainly considers the reaction as a process for doping Li into SiNWs but they

also mention that it might have applications for LIBs.

Interest in SiNW anodes did not reappear for almost a decade, until Chan et al. [89] reported electrochemical cycling of SiNWs grown by CVD on a stainless steel substrate. Relatively few of the many subsequent articles cite the original work by Zhou et al.

NWs allow space for expansion while retaining the long-range connectivity needed for electron transport. This is especially true for NWs grown on a conducting substrate by CVD, as each NW has a direct electrical connection to the substrate. Chan et al. [90] also demonstrated germanium NWs, which had relatively good high-rate performance but a lower capacity than the SiNWs.

Choi et al. [91] deposited SiNWs on a CF network. A higher density of NWs was deposited per unit area than on the stainless steel substrates used by *e.g.* Chan et al. [89]. Carbon fibre is less dense than stainless steel, improving the overall specific capacity, and is also able to act as an electrode in its own right (see subsection 1.2.5). However, they were not able to access the full theoretical capacity of Si, instead observing capacities less than 2000 mA h g^{-1} .

Further experiments by Chan et al. [92] used scanning electron microscopy (SEM) and X-ray photoelectron spectroscopy (XPS) to study the SEI formed on SiNW anodes during cycling. XPS showed that the composition of the SEI formed on silicon is similar in composition to that formed on graphite. SEM images of samples taken at different points in the charge-discharge cycle showed that the SEI grows thicker during lithiation and shrinks again during delithiation. Etching the native oxide from the surface of the NWs with HF slightly improved Coulombic efficiency in the first cycle at the expense of much faster capacity loss in subsequent cycles.

DFT studies of lithium insertion into SiNWs by Zhang et al. [52] showed that the initial reaction of lithium at the surface of a SiNW is relatively easy but the layer immediately below the surface has no sites where lithium can easily penetrate, making it a barrier to lithiation of the bulk silicon interior. They show that SiNWs with the long axis along the crystallographic $[110]$ direction have the highest Li binding energies but that “diffusion barrier height has little relationship with the orientation”. However, this paper only studies the initial lithiation of very small ($\varnothing \leq 2.5 \text{ nm}$) NWs formed of crystalline silicon, and will thus not necessarily be applicable beyond the early stages of the initial lithiation.

Liu et al. [93] reported the first *in situ* TEM study of SiNW-based LIBs. They showed that, for intrinsic (pure Si) NWs, a residual crystalline silicon (*c*-Si) core remains even after prolonged charging. The volume expansion during lithiation was mainly in the radial direction, in contrast with their earlier work [94] on SnO_2 NWs, with a total volume expansion of $\approx 300\%$. Doping the silicon with phosphorus and coating the outside of the NWs with sputtered amorphous carbon both gave an order of magnitude increase in current density and showed complete lithiation with no crystalline core remaining.

Further *in situ* and *ex situ* TEM studies of SiNW-based LIBs by Liu et al. [95] showed that *c*-Si NWs expand anisotropically during first lithiation, with the greatest expansion along the crystallographic $[1\bar{1}0]$ direction. The anisotropic lithiation causes necking and sometimes even lengthwise fracture of the NWs. Liu et al. suggest that using *a*-Si NWs could give better performance than *c*-Si by avoiding the extra strain caused by anisotropic lithiation.

Most experiments with SiNWs, including those described herein, have used SiNWs produced by CVD. CVD requires high temperatures and vacuum systems, and takes hours (including all necessary preparation steps such as catalyst deposition) to produce a few milligrams of material. As such, CVD-produced SiNWs can be used to make small quantities for experimental purposes but would be prohibitively expensive as a method for producing batteries for commercial sale. However, Chan et al. [96] have demonstrated batteries made with solution-grown SiNWs coated with carbon by pyrolysis of sucrose. These solution-grown anodes showed capacities of 1400 mA h g^{-1} to 1600 mA h g^{-1} which dropped by around 20% after 50 cycles.

Peng et al. [97] demonstrated a wet etching process to produce SiNWs from *c*-Si wafers. The cycle life of the resulting cells is not clear as they only published results for three cycles.

Wang and Han [98] present an entirely solution phase process producing a SiNW-graphene composite anode, avoiding vacuum, high temperatures *etc.* They report a reversible capacity of 2470 mA h g^{-1} . They claim that “The Li-Si alloying process begins at a similar voltage of $\sim 0.22\text{ V}$.” in the first discharge. This would be intriguing as the SiNWs were etched from *c*-Si wafers, whereas the lithiation process at $\sim 0.2\text{ V}$ is characteristic of *a*-Si (see subsection 1.2.2). However, the cyclic voltammetry (CV) graph in their article does not seem to show this, but rather appears to have a single CV peak at $\sim 70\text{ mV}$, characteristic of *c*-Si as expected.

While CVD is not a viable process for manufacturing on an industrial scale, it offers good control over morphology and composition and, if done on a conducting substrate, ensures that all the deposited material has a good electrical contact. The high surface-area-to-volume ratio means that cycling can be done quickly, and enhances the importance of surface effects. These properties make CVD-deposited SiNWs an excellent model system for studying the electrochemical reactions of silicon.

Ruffo et al. [99] used SiNWs as a model system to study the SEI on silicon using electrochemical impedance spectroscopy (EIS) and X-ray photoelectron spectroscopy (XPS). The XPS experiments gave estimates for the composition of the SEI at different states of charge, showing that the region of the SEI closest to the electrolyte consists mainly of hydrocarbons, while the region closest to the anode consists mainly of inorganic species such as LiF and Li_2CO_3 . The EIS experiments showed that the surface resistance reaches

a minimum at $\sim 1000 \text{ mA h g}^{-1}$ and is highest on the first cycle, decreasing over the first ten cycles before levelling off at around an order of magnitude less than in the first cycle. The higher resistance at low lithiation levels led them to hypothesise that limiting the cycling range at the delithiation end could improve capacity retention, and galvanostatic cycling experiments confirmed this with the capacity from a 0.7 V limit exceeding that from a 2 V limit after about 30 cycles. This builds on their previous work [92] which confirms in SiNWs the findings of Obrovac and Krause [70] that limiting the extent of lithiation improves capacity retention.

This result also agrees with finite element modelling of stress-enhanced diffusion (the process by which the stress caused by volume expansion during lithiation reduces diffusion barriers) of Li in *a*-Si NWs by Gao and Zhou [100]. They found that stress-enhanced diffusion is lower at lower Li concentrations such as during the first charge or in a deep discharge condition. They recommend that deep discharge be avoided if the subsequent charge is to be done quickly.

Table 1.1: Theoretical gravimetric and volumetric capacities of lithium silicides. The full table (including calculations) is available in OpenDocument format at <http://dx.doi.org/10.6084/m9.figshare.1021500>.

Material	Formula units per unit cell	Cell volume (\AA^3)	Formula mass (g mol^{-1})	Gravimetric capacity (mA h g^{-1})		Volumetric capacity (mA h ml^{-1})		Expansion		reference for lattice parameters	
				Li+Si	<i>vs</i> Si	Li+Si	<i>vs</i> Si	<i>vs</i> Si	Li+Si		<i>vs</i> Li
Si	8	160.17	28.09	0	0	0	0	0	N/A		
LiSi	16	502.76	35.03	765	954	1416	2223	57%	-25%	45%	Stearns et al. [48]
Li ₁₂ Si ₇	8	2437.17	279.88	1149	1636	1753	3811	117%	-24%	17%	Nesper [101]
Li ₇ Si ₃	2	308.90	132.84	1412	2227	2017	5187	157%	-27%	2%	Nesper [101]
Li ₁₃ Si ₄	2	538.37	202.56	1720	3101	2149	7225	236%	-25%	-4%	Nesper [101]
Li ₁₅ Si ₄	4	1219.90	216.44	1857	3579	2189	8336	281%	-25%	-6%	Xu et al. [51]
Li _{16.42} Si ₄	4	1310.61	226.29	1945	3917	2230	9125	309%	-25%	-8%	Zeilinger et al. [47]
Li ₂₁ Si ₅	16	6549.70	286.17	1967	4008	2283	9336	309%	-26%	-10%	Nesper and von Schnering [45]
Li ₁₇ Si ₄	20	6566.41	230.32	1978	4056	2304	9448	310%	-27%	-11%	Zeilinger et al. [46]
Li	2	43.24	6.94	3862	N/A	2058	N/A	N/A	0	0	

1.3 Diffraction and total scattering

X-rays and thermal neutrons have wavelengths of the same order of magnitude as the interatomic distances in condensed matter. This means that, when they interact with a material, any ordering of the atomic positions will be reflected in the distribution of the scattered radiation. Helpfully, their interaction with matter is strong enough to give detectable scattering from small samples, but still weak enough that the weak scattering approximation is reasonable *i.e.* most of the scattered radiation has only been scattered once. This simplifies the process of deducing information about the atomic structure from the scattering pattern.

This chapter uses the nomenclature for scattering functions outlined in Keen [102], except that $S(Q)$ is defined as unnormalised: $S(Q) = F(Q) + S^0$ rather than $S(Q) = \frac{F(Q)+S^0}{S^0}$.

1.3.1 The scattering function

In the weak scattering approximation, incident radiation (X-rays or neutrons) impinges on the sample and either passes straight through with no scattering or is scattered exactly once. The probability of scattering occurring at a point \mathbf{x} in the sample is given by the scattering density $f(\mathbf{x})$. The radiation scattered from all the different points in the sample then interacts by wave superposition giving an interference pattern. Radiation with different energies will give an interference pattern that oscillates with a frequency $\frac{\Delta E}{h}$, where ΔE is the difference between the two energies. Because this oscillation is so fast for any appreciable difference in energies, the observed interference is averaged out — interference is only observed between radiation of the same energy. If a beam contains radiation of different energies, the different energies will scatter independently and can therefore be considered in isolation — there is no difference between the scattering of one particular energy in a polychromatic beam and the scattering of a monochromatic beam of that energy. I will therefore start by discussing the scattering of monochromatic radiation, and go on to discuss polychromatic radiation in subsection 1.3.3.

1.3.2 Scattering of monochromatic radiation

In scattering experiments, the incident radiation is usually collimated *i.e.* a plane wave with wave vector \mathbf{k}_i , although there are some applications (such as ptychographic coherent diffractive imaging [103]) where divergent or convergent incident radiation is used. The detector is also usually far enough from the sample that radiation there can also be considered planar with wave vector \mathbf{k}_d . Parallel absorbing plates known as Söller slits are sometimes used to ensure collimation of the detected radiation and to block out unwanted radiation that has not come from the sample.

The amplitude of the radiation arriving at the detector with wave vector \mathbf{k}_d having been scattered at point \mathbf{x} is given by

$$e^{-i\mathbf{k}_i \cdot \mathbf{x}} f(\mathbf{x}) e^{i\mathbf{k}_d \cdot \mathbf{x}} \quad (1.1)$$

Summing the scattered radiation from every point in the sample gives the total amplitude of the scattered radiation at a given wave vector (*i.e.* wavelength and scattering angle).

$$a(\mathbf{k}_d) = \int \int e^{i(\mathbf{k}_d - \mathbf{k}_i) \cdot \mathbf{x}} f(\mathbf{x}) d\mathbf{x} d\mathbf{k}_i \quad (1.2)$$

For a given \mathbf{k}_i , and defining $\mathbf{Q} = \mathbf{k}_d - \mathbf{k}_i$, this results in a Fourier transform (FT):

$$a(\mathbf{Q}) = \int e^{i\mathbf{Q} \cdot \mathbf{x}} f(\mathbf{x}) d\mathbf{x} \quad (1.3)$$

Detectors are only able to measure the intensity $S(\mathbf{Q})$ of the scattered radiation, which is given by the square modulus of the (in general complex) amplitude.

$$S(\mathbf{Q}) = \left| \int e^{i\mathbf{Q} \cdot \mathbf{x}} f(\mathbf{x}) d\mathbf{x} \right|^2 \quad (1.4)$$

Expanding the square gives an expression in terms of the scattering at two points \mathbf{x} and \mathbf{x}' and the distance $\mathbf{r} = \mathbf{x} - \mathbf{x}'$ between them:

$$S(\mathbf{Q}) = \int e^{i\mathbf{Q} \cdot \mathbf{x}} f(\mathbf{x}) d\mathbf{x} \int e^{-i\mathbf{Q} \cdot \mathbf{x}'} f(\mathbf{x}') d\mathbf{x}' \quad (1.5)$$

$$S(\mathbf{Q}) = \int \int e^{i\mathbf{Q} \cdot (\mathbf{x} - \mathbf{x}')} f(\mathbf{x}) f(\mathbf{x}') d\mathbf{x} d\mathbf{x}' \quad (1.6)$$

Neutrons scatter only off the nucleus (in non-magnetic materials), and atomic nuclei are much smaller than the wavelength of thermal neutrons (the largest nuclei have diameters around 15 fm, compared to a typical wavelength for thermal neutrons of $1 \text{ \AA} = 100\,000 \text{ fm}$), so to a good approximation the integral can be expressed as the sum of scattering from discrete points — in other words, the scattering density $f(\mathbf{x})$ can be expressed as a set of delta functions whose size is given by the scattering length b_i at the positions \mathbf{x}_i of the atomic nuclei.

$$S_{\text{neutron}}(\mathbf{Q}) = \int \int e^{i\mathbf{Q} \cdot (\mathbf{x} - \mathbf{x}')} \sum_{i,j} b_i \delta(\mathbf{x} - \mathbf{x}_i) b_j \delta(\mathbf{x}' - \mathbf{x}_j) d\mathbf{x} d\mathbf{x}' \quad (1.7)$$

$$S_{\text{neutron}}(\mathbf{Q}) = \sum_{i,j} b_i b_j e^{i\mathbf{Q} \cdot \mathbf{r}_{ij}} \quad (1.8)$$

X-rays, on the other hand, scatter primarily off electrons, so the scattering density is proportional to the electron density, which is finite over the entire material, but has its highest values close to the atomic nuclei. The scattering density $f(\mathbf{x})$ can therefore be considered as the convolution of a set of discrete points at the positions of the atomic nuclei with a function (or functions, if there is more than one element) expressing the electron density surrounding each nucleus. The Fourier transform of a convolution is a simple product, so the scattered radiation is equal to that expected from an array of points at the nuclei, multiplied by the FT of the electron density function. Since the electron density around a nucleus is approximately spherically symmetric (and even closer to spherically symmetric where it varies most rapidly near the nucleus), its FT is also approximately spherically symmetric (with the approximation becoming even more accurate at high Q) and therefore depends only on the magnitude of \mathbf{Q} and not its direction.

$$S_{\text{X-ray}}(\mathbf{Q}) = \sum_{i,j} f_i(Q) f_j(Q) e^{i\mathbf{Q}\cdot\mathbf{r}_{ij}} \quad (1.9)$$

1.3.3 Polychromatic radiation

If many different energies (and thus different wavelengths λ) are present in the beam, the radiation at different energies will scatter at different angles 2θ for a given Q , according to the formulae:

$$Q = \frac{4\pi \sin \theta}{\lambda} \quad (1.10)$$

$$\theta = \sin^{-1} \left(\frac{Q\lambda}{4\pi} \right) \quad (1.11)$$

Summing up the detected intensity at all wavelengths will give a smeared-out scattering pattern which will be difficult to interpret. To avoid this, radiation from a polychromatic source can be passed through a monochromator to select a single wavelength. Alternatively, in some cases the wavelength of the scattered radiation can be measured as it is detected, either directly (e.g. energy-dispersive X-ray detectors) or indirectly (e.g. neutron time-of-flight measurements), or resolved by a secondary monochromator placed in the scattered beam. This is discussed in more detail in subsection 1.3.6.

1.3.4 Pair distribution function methods

As seen above, the measured intensity of the scattered radiation is the square modulus of its amplitude (*i.e.* the amplitude multiplied by its complex conjugate), and the amplitude is given by the the Fourier transform of the scattering density.

Multiplication by the complex conjugate in reciprocal space is equivalent to correlation

in real space. The inverse FT of the measured intensity is therefore the autocorrelation of the scattering density.

For single crystal diffraction this three-dimensional inverse FT is known as the Patterson function. For powder diffraction, where the measured scattering intensity is spherically averaged by the random distribution of crystals in the powder, and for amorphous materials where there are no preferred scattering directions in the first place, the scattering intensity depends only on the absolute value of the momentum transfer $Q = |\mathbf{Q}|$ and its inverse FT, which depends only on the absolute distance $r = |\mathbf{r}|$, is proportional to the pair distribution function (PDF).

$$2\pi G(\mathbf{r}) = \int F(\mathbf{Q}) e^{-i\mathbf{Q}\cdot\mathbf{r}} d\mathbf{Q} \quad (1.12)$$

$$= \int_0^\infty F(Q) \int_0^\pi \int_0^{2\pi} e^{-iQr \cos\theta} Q^2 \sin\theta d\phi d\theta dQ \quad (1.13)$$

$$= \int_0^\infty F(Q) \left[\frac{2\pi}{iQr} e^{iQr \cos\theta} \right]_{\theta=0}^\pi Q^2 dQ \quad (1.14)$$

$$= \int_0^\infty F(Q) \frac{2\pi Q}{r} \sin(Qr) dQ \quad (1.15)$$

(where θ and ϕ are the spherical polar angles between \mathbf{r} and \mathbf{Q} — note that this is not the same as the traditional use of θ and ϕ in crystallography).

Defining $D(r) = rG(r)$, this simplifies to:

$$D(r) = \int_0^\infty QF(Q) \sin(Qr) dQ \quad (1.16)$$

$$QF(Q) = \int_0^\infty D(r) \sin(Qr) dr \quad (1.17)$$

1.3.5 Total scattering

For an infinite ideal crystal with no defects and no thermal or zero-point motion, scattering only occurs at angles which correspond to points on the reciprocal lattice. The scattering at these angles is very intense, and the resulting peaks in a graph of intensity against angle or Q are known as Bragg peaks. These Bragg peaks will, for an ideal crystal, continue out to infinite Q . When the scattering pattern is measured, the physical limitations of the diffractometer (for example, the maximum possible 2θ and minimum λ that can be used) will mean that data can not be acquired beyond a certain maximum value of Q , and imperfections such as finite slit widths and polychromaticity of the beam will lead to broadening of the detected peaks.

When dealing with real crystals, however, even the ‘ideal’ scattering is not a perfect pattern of delta functions at the reciprocal lattice points extending to infinity. Thermal or

zero-point vibrational motion of the atoms, together with (in the case of X-rays or when considering magnetic scattering of neutrons) the finite size of the electronic orbitals, mean that the scattering density of individual atoms is smeared out rather than concentrated at a single point. This leads to a drop-off in the scattered intensity with increasing Q , with the extent of the scattering in Q being inversely proportional to the spatial extent of the smeared-out scattering density. Disorder which leads to atoms being displaced from their average crystallographic positions will give an equivalent drop-off in the intensity of the Bragg peaks with increasing Q but, if this disorder is not completely random but rather correlated with the displacements of nearby atoms, the scattered intensity will show up as diffuse scattering between the Bragg peaks rather than being lost entirely. If the crystal has a finite size, then the Bragg peaks in the ideal scattering will be have a finite width, inversely proportional to the spatial extent of the crystal. This ‘spatial extent’ does not necessarily correspond to the physical size of what is macroscopically seen as a crystal, but rather to the range around a typical atom inside which the relative positions of the surrounding atoms are given by the crystal lattice; this is also limited by, for example, crystal dislocations. If a powder diffraction sample contains several slightly different crystal structures, for example if some crystals are under strain and therefore have slightly different lattice parameters, this will also show up as a broadening of the peaks in the scattering pattern.

When only the long range average crystal structure is wanted, the scattered intensity between the Bragg peaks, and the shape of the Bragg peaks themselves, can be ignored. (The drop-off in intensity with increasing Q must still however be taken into account.) This influences diffractometer design, as accurately measuring the absolute intensity of non-Bragg scattering is not important.

When a slightly more precise model is needed, but the structure can still be described accurately as a crystal of finite size at a finite temperature, the Bragg peaks will have a finite width and their shape can be fitted through Rietveld refinement [104]. In this case the intensity in between the Bragg peaks is still unimportant. Many of the Bragg peaks will have intensities well above the background, so a rigorous measurement and subtraction of the background intensity is not necessary.

However, short-range correlations between atoms in a disordered crystal or a wholly amorphous structure show up as broad features in $F(Q)$ and often have intensities similar to those of confounding factors such as background signals. Therefore, when information about short-range correlations is sought, all of the information in the scattering pattern must be retained, and any background signal accurately subtracted.

1.3.6 Radiation sources

Neutron sources fall into two categories: reactor sources and spallation sources.

Reactor sources use the surplus neutrons from a nuclear chain reaction (usually ^{235}U fission), providing a continuous flux of neutrons. The reactor core will contain a moderator to ensure that the neutron energy spectrum is optimised for sustaining the chain reaction. If a different energy spectrum is required for the experiment, a secondary moderator held at a different temperature can be used. Because neutron detectors are unable to measure the energy or wavelength of the detected neutrons, a monochromator is needed to select an individual wavelength.

Spallation sources use neutrons knocked out of the nuclei of heavy metal atoms by the impact of high energy protons. The protons are accelerated by a synchrotron and arrive in bunches, meaning that the neutrons are emitted in pulses. Since a neutron's speed is inversely proportional to its wavelength, neutron energy can be resolved by measuring the time between the impact of the proton pulse and the arrival of the neutron at the detector. This means that a monochromator is no longer necessary and allows the whole neutron flux of the source to be used. Moderators are still used to alter the energy spectrum of the neutrons, and rotating neutron-absorbing disks known as 'choppers' can be used to select parts of the pulse.

All experiments presented here were carried out at the ISIS spallation source at the Rutherford Appleton Laboratory.

X-ray sources are either lab-based or synchrotron sources.

Lab X-ray sources accelerate electrons to energies of $\sim 50\text{ kV}$ and impact them into metal targets. Some of these electrons collide with and eject electrons from the core orbitals of atoms in the target. Electrons transitioning from higher orbitals to fill the vacant core orbitals emit X-rays with a characteristic energy. There is also a broad bremsstrahlung background, requiring the use of filters or even a monochromator to select only a narrow frequency range.

Synchrotron sources use the radiation emitted by electrons orbiting a synchrotron at relativistic speeds. Classical electrodynamics predicts that electrons orbiting a synchrotron at just under the speed of light would emit radio waves in all directions with a wavelength on the same order as the diameter of the synchrotron. However, relativistic blueshifting means that the emitted radiation is concentrated in the X-ray region of the spectrum and emitted in a very narrow cone around the direction of motion of the electrons. Adding so-called "insertion devices" ("wigglers" or "undulators") with rapidly alternating magnetic fields further increases the brilliance of the emitted radiation over that emitted simply as a consequence of keeping the electrons in a circular orbit. They also give control over the polarisation of the emitted radiation. Synchrotron X-ray sources typically use pairs of silicon crystals as monochromators.

1.3.7 Transformation to real space

Total scattering experiments produce data which show the scattered intensity as a function of scattering angle (and possibly also time of flight) sampled at regular intervals over a finite range. These data will be affected by background counts, errors due to malfunctioning detector elements, and scattering and attenuation by the sample environment. Correcting for these effects, and transforming from instrument-specific dimensions such as scattering angle and time-of-flight to instrument-independent dimensions such as Q , is typically done with programs such as `Gudrun` written and maintained by the instrument scientists at that facility, although there is now a project to build a data reduction program suitable for all facilities, `Mantid` [105].

However, these programs typically leave in the instrumental resolution function rather than attempting to deconvolve to obtain the true $S(Q)$ of the sample. This broadening of the $S(Q)$ leads to attenuation of the $G(r)$ at high r , hiding any long-range order. In general, the width and shape of the instrumental resolution function vary with Q , meaning that simple Fourier filtering methods of deconvolution will not work. Instead, optimisation algorithms such as Metropolis Monte Carlo are used to obtain a $G(r)$ which best fits the observed $S(Q)$, as implemented in `MCGR` [106] for neutron total scattering data from reactor sources and `MCGRtof` [107] for neutron time of flight (ToF) data. `ProfFitS`, a new software package for transformation to real space, is described in chapter 3.

1.4 Reverse Monte Carlo analysis

Even if an instrument could record the diffraction pattern of a material perfectly, there are still an infinite number of structures that could give rise to any scattering pattern. Once the possibility of experimental error is taken into account, the range of possible structures becomes even broader. However, many of the structures that are compatible with the observed diffraction pattern can be ruled out by prior knowledge about the properties of matter (*e.g.* two atomic nuclei should not come closer together than the sum of their atomic radii). In addition, many of the possible structures are sufficiently similar to each other that they can be considered identical.

1.4.1 Monte Carlo algorithms

“Monte Carlo” is a term coined by Metropolis and Ulam [108] used to describe any algorithm which uses random sampling to derive an approximate solution to a computationally hard problem. In the context of condensed matter research, it is most often used to refer to Markov chain Monte Carlo algorithms in which the transition probability includes some estimation of the Boltzmann factor given by a calculation of the energy

of the system according to some model. This kind of Monte Carlo algorithm was first proposed by Metropolis et al. [109] and is therefore known as “Metropolis Monte Carlo”.

The term “reverse Monte Carlo” (RMC) was coined by McGreevy and Pusztai [110] in analogy to the restricted use of the term “Monte Carlo” in condensed matter science. Standard “Monte Carlo” methods use internal calculations of energy to guide updates of the atomic configuration, then once the calculation is finished use comparisons with experimental data to validate the result. Reverse Monte Carlo methods use the goodness-of-fit to experimental data to guide updates to the configuration, thereby aiming to provide results that are not biased by the approximations made in energy calculations. RMC was initially used for neutron total scattering data [110], but has subsequently been used to fit atomistic models to other data sources such as extended X-ray absorption fine structure (EXAFS) [111] or diffuse electron diffraction [112].

1.4.2 Computational limits

RMC modelling calculates PDFs from atomistic models. It is not practical to use models containing the same number of atoms as a small droplet or crystallite, let alone an entire sample. Instead, a small volume is taken as representative, with correlations outside that volume calculated using periodic boundary conditions.

The periodic boundary conditions mean that calculated correlations beyond half the ‘box size’ are not reliable, so typically data are only calculated out to this range. For liquids and amorphous solids, this does not present much of a problem as there are no correlations further than a few nanometres. However, for disordered crystals where there is still some long-range order, this finite r range can give systematic distortions in the the calculated $S(Q)$. Truncating the $G(r)$ data at a given r value is equivalent to multiplying by a step function. The FT of a step function is a sinc function, so the calculated $S(Q)$ is effectively convolved with a sinc. In order not to distort the fit, the experimental $S(Q)$ must likewise be convolved with a sinc function.

Calculating an NMR spectrum for an atomic configuration of tens of thousands of atoms such as is used in RMC would take far too much time and computational resources to be done at every RMC iteration. Nevertheless, information derived from NMR spectra, such as the number of different atomic environments for each element, can be used as a constraint [113, 114]. This is known as invariant environment refinement technique (INVERT) and is particularly valuable for covalently bonded materials with a low packing fraction such as silica or buckminsterfullerene.

1.4.3 RMCprofile

The broadening of the experimental $S(Q)$ function to account for the finite r range allowed by the finite box size means that, in RMC simulations of disordered crystalline materials, the information about the long range average structure contained in the Bragg peaks is not retained. Tucker et al. [115] developed a method for including the data from the Bragg peaks by calculating the intensity that each peak would have for a crystal consisting of the RMC simulation box infinitely tiled in a primitive cubic lattice. Initially these peak intensities were compared with peak intensities extracted from the data by the method developed by Pawley [116], but this method is only applicable to non-overlapping peaks. Subsequent work led to the development of `RMCprofile` [117], which rather than extracting peak intensities from the data uses the calculated intensities to calculate a pattern (in the case of ToF instruments, a ToF profile — hence the name) which can be directly compared to the experimental data.

An alternative was proposed by Montfrooij et al. [118] — their `RMCPow` program calculates a three dimensional $S(Q)$ which includes all the Bragg peaks. However, this approach becomes computationally infeasible for data that extend to large values of Q , as a three-dimensional array with the required size and resolution would be too large to store in random access memory (RAM) and would take too long to calculate for each iteration.

1.5 Nuclear magnetic resonance

Both total scattering and nuclear magnetic resonance (NMR) provide information on the relative arrangement of atoms over short ranges. This information is often complementary: for example, total scattering sums up the contribution from all elements in the sample, whereas NMR allows selecting out individual elements or pairs of elements. This section describes the physical processes behind NMR spectroscopy.

1.5.1 Physical basis of NMR

Angular momentum is quantised in units of \hbar , with individual particles having angular momenta that are either integer or half-integer multiples of \hbar . Since nuclei are charged, any nucleus with non-zero angular momentum has a non-zero magnetic moment. (In fact, even the neutron has a magnetic moment despite being electrically neutral, as it is composed of electrically charged particles whose charges sum to zero but whose magnetic moments do not.)

In the absence of an external magnetic field, the $2I + 1$ spin states of a spin I nucleus will be degenerate but, if a magnetic field is applied, this field will interact with the intrinsic magnetic moment of the nucleus leading to changes in the energies of the different spin states. This difference between the energies of different spin states is known as the Zeeman splitting, and the corresponding frequency given by $E = hf$ is known as the Larmor frequency. For field strengths available from superconducting Nb-Ti and Nb₃Sn magnets (on the order of 10 T), Larmor frequencies for most nuclei are in the region of tens or hundreds of megahertz. Electromagnetic radiation in this frequency range can easily be generated and detected by simple electrical oscillators, although achieving high sensitivity and precision requires more sophisticated electronics. This coupling of nuclear spin states to electromagnetic radiation is known as nuclear magnetic resonance (NMR) and the use of this phenomenon to obtain chemical information is known as NMR spectroscopy.

The magnetic field experienced by a nucleus depends on its local environment — the other nuclei around it and the nature of the bonding between them. This means that nuclei in different chemical environments have different energy gaps between their spin states and therefore precess at different frequencies. This environment-dependent change in the frequency is known as the chemical shift and is defined relative to a standard reference material. For nuclei with an electrical quadrupole moment, this will couple to any electric field gradient at the nucleus, altering the energies of the different spin states further.

1.5.2 Effects of atomic motion

For a material to be usable as a LIB electrode, it must not only react with lithium but also allow Li^+ ions to diffuse in and out of the electrode under ambient conditions. It is therefore unsurprising that the effects of atomic motion are seen in Li NMR spectra of LIB electrode materials, and indeed that these ‘dynamical’ effects can be used to probe functionally relevant properties [119].

The motion of the lithium ions from site to site in the electrode tends to average out the effects due to the local environment differing in each individual site. Instead, the spectrum of a material in which Li motion is fast on the NMR timescale will reflect an average local environment. Given that individual sites in a crystal or amorphous material will often be highly anisotropic and thus will result in broadened peaks in the NMR spectrum due to chemical shift anisotropy and/or quadrupolar coupling, whereas the average environment is much more uniform, this motion is very helpful in ensuring clearly-defined peaks and facilitating interpretation.

1.5.3 Skin depth effects

The cells used in the *in situ* experiments described in chapter 5 use lithium metal as a counter electrode. Because lithium metal conducts electricity, the electrical field component of the radio frequency (RF) pulse from the NMR spectrometer will cause currents to flow. These currents will in turn generate a magnetic field, which will oppose the field from the RF pulse. The overall effect is that both the applied RF pulse and the emitted NMR signal are attenuated in amplitude, and retarded in phase, as they pass through the metal. The ‘skin depth’ δ , the depth at which the strength of the field falls to $\frac{1}{e}$ of its value at the surface, is given by the formula:

$$\delta = \sqrt{\frac{\rho}{\pi\mu f}} \quad (1.18)$$

where ρ is the resistivity of the metal, μ is its magnetic permeability, and f is the frequency of the RF pulse. For lithium metal and a frequency of 117 MHz (the Larmor frequency of ^7Li at the field strength of the magnet used in the experiments described in chapter 5) the skin depth is approximately 14 μm .

Because the lithium metal counter electrode is much thicker than the skin depth, only the lithium near the surface contributes to the NMR signal. Nevertheless, the majority of the emitted signal comes from lithium far enough inside the metal to have its phase somewhat retarded by the opposing eddy currents, so the signal is out of phase with signals from non-conducting material such as the lithium salts in the electrolyte. On the other hand, any microstructured lithium ‘moss’ or ‘dendrites’ on the surface of the metal

will be thin enough that the RF pulse can penetrate them without much loss of intensity [120], and with a smaller phase retardation.

1.5.4 In situ methods

Typically, when analysing a material by NMR, the material is isolated, packed into a container designed to fit a particular probe and inserted into the spectrometer. To follow the progress of a reaction, the reaction must be run several times, stopping and quenching each reaction after a different length of time. This is time consuming, potentially requires large quantities of materials, and can give misleading results if the initial conditions for each reaction are not exactly the same. An alternative is to create a modified reaction vessel (in this case an electrochemical cell) suitable for running the reaction inside the spectrometer and simultaneously acquiring NMR spectra. Spectra thus acquired are known as *in situ* spectra.

Chevallier et al. [121] were the first to measure *in situ* spectra of electrochemical cells, namely ^7Li spectra of lithium intercalating into disordered carbon. Key et al. [122] first applied these *in situ* techniques to silicon anode materials. However, silicon powder composite electrodes require an externally imposed pressure to retain electrical connectivity on delithiation [77], and limitations imposed on the cell construction by the requirements of the NMR experiment meant that this pressure could not be applied. They were therefore only able to obtain spectra for the initial lithiation process and not for subsequent cycles.

1.6 Analysis of NMR data

Data from an NMR experiment are acquired in the form of one or more free induction decays (FIDs). For a simple experiment, the FID will in principle consist of several superposed exponentially decaying oscillating functions, one for each atomic environment experienced by the nucleus being studied. It is hard for a human to analyse such a pattern by visual inspection.

Performing a Fourier transform on the time-domain FID will give a frequency-domain spectrum. The FT of an exponentially decaying oscillating function is a Lorentzian function whose width is inversely proportional to the decay constant and whose central frequency is equal to the frequency of oscillation. If the atomic environments corresponding to a given peak are not exactly identical but rather come from a distribution of similar environments, the resulting peak will have the shape of a Lorentzian convolved with a Gaussian — otherwise known as a Voigt function.

If the various peaks in a spectrum are separated by a sufficient distance, it is easy to analyse the spectrum by eye. However, if the peaks overlap significantly, it becomes necessary to use numerical fitting algorithms, especially if reproducible quantitative results are required. There are many proposed algorithms [123] for fitting NMR data either in the frequency domain or in the time domain.

Because it avoids the Fourier transform stage, fitting in the time domain has the potential to be more accurate than fitting in the frequency domain [124]. This is particularly true if the FID has been truncated as this distorts the spectrum [124]. Fitting a set of exponentially decaying oscillating functions to time domain NMR data, or a set of Lorentzian functions to frequency domain NMR data, is a nonlinear least squares optimisation problem. One problem with fitting in the time domain rather than the frequency domain is the difficulty of picking a good starting point for the fit. (In the frequency domain a simple peak-picking algorithm can be used.) The ‘linear prediction’ method of Barkhuijsen et al. [124] can be used for this. Although the overall fitting problem is nonlinear, the dependence of the model function on many of the parameters (such as the amplitudes and phases of individual signals) is linear. This means that the overall fitting process can be substantially speeded up by the ‘variable projection’ algorithm developed by Golub and Pereyra [125].

1.6.1 Decomposition into simpler spectra

In many cases an NMR spectrum can be expressed as the weighted sum of a number of simpler spectra. In the case of a mixture of different compounds or materials, the spectrum will be the sum of the spectra of each compound weighted by their respective amounts. Within each compound, if there are magnetically inequivalent nuclei, the spectrum will

be given by the sum of the spectra of each group of equivalent nuclei weighted by their number.

An NMR measurement only gives the resulting sum, however, and not the decomposition into components originating from different compounds or inequivalent nuclei. However, with *a priori* knowledge of the forms that the components are likely to take, a model can be fitted representing the measured spectral data as the sum of several components that fit the *a priori* expectations.

If the measured data consists of a single spectrum, the only way this can be done is by using *a priori* assumptions about the lineshape or other properties of the component spectra. However, if several spectra have been measured, with the amounts of the various compounds or materials in the sample varying from spectrum to spectrum, there is another option. The component spectrum originating from each compound or material should remain constant throughout the data acquisition process — only the weightings in the sum that gives the overall measured spectrum should change. Thus, at least in principle, it should be possible to fit a model to the spectral data using only this *a priori* knowledge, with no assumptions about the lineshape or other properties of the individual component spectra.

This model does however assume that the samples are in fact mixtures of different amounts of a relatively small number of compounds or materials with discrete spectra. If instead the system contains a ‘solid solution’ with continuously varying composition and spectrum, the ‘solid solution’ material in each sample will be different from that found in all the other samples and will thus have a different spectrum. The result is that, in order to reproduce the measured spectra, a separate additive component spectrum is needed for each measured spectrum, so the model is no simpler than the data it models. In fact, the existence of this problem can be used to discriminate between systems where a small number of discrete compounds or phases exist and systems with continuously variable phases. If a good fit to the data can be obtained with a small number of components, the system is likely to contain only discrete phases, whereas if many components are required then a solid solution phase is more likely.

1.6.2 Principal Component Analysis

Given an $m \times n$ matrix M whose elements sum to zero, principal component analysis (PCA) finds matrices U and V such that the first k columns of U multiplied by the first k rows of V give the best approximation of M for any pair of $m \times k$ and $k \times n$ matrices. (V is typically chosen so that its row vectors have unit norm, *i.e.* $VV^T = I$, this then determines U uniquely.) In other words, the first row of V is the basis vector which accounts for as much as possible of the variation between different rows of M , the second row accounts for as much as possible of the remaining variation, and so on.

For NMR data analysis, the matrix M is built by stacking spectra or FIDs in the rows, so that m is the number of spectra acquired and n is the number of data points in each spectrum or FID. Since the spectra or FIDs will not in general sum to zero, the mean must be subtracted before performing PCA. Most PCA libraries will do this automatically.

PCA was first applied to NMR data by Stoyanova et al. [126]. Since then it has mostly been used in metabolomics and magnetic resonance imaging (MRI). Initial implementations only handled the real part of the spectrum, but Elliott et al. [127] showed that using the full complex spectrum would not only improve the accuracy by a factor of $\sqrt{2}$ but also avoid spurious extra components caused by errors in phasing. In cases where each component only covers a limited range of the spectrum, even variations in first-order phase shift can be accommodated, as the effect of the first-order phase shift will be approximately equal to a constant phase offset (differing from component to component) in the region covered by each component.

If there are slight changes in NMR acquisition conditions between spectra (for example drift in the magnetic field of the spectrometer), then the spectra of the individual compounds will no longer remain perfectly constant from spectrum to spectrum — there will be changes in the lineshape or in the frequency offset. This will lead to spurious additional components appearing in the analysis. Wang et al. [128] discuss methods of correcting for frequency shifts by checking the principal components for the presence of these spurious features and using cross-correlation to determine the correct offset. With the methods developed by Witjes et al. [129], changes in frequency offset and even some lineshape variations can be corrected automatically.

1.6.3 Non-negative matrix factorisation

Non-negative matrix factorisation (NMF), like PCA, aims to approximate a matrix M by the product of two matrices (called W and H in NMF). However, as implied by the name, it restricts the values of W and H such that all the matrix elements are non-negative. Typically the elements of the matrix M will also be non-negative, although it is possible (*e.g.* in the case of the baseline of an NMR spectrum) for a zero or small positive ideal value plus Gaussian noise to give a negative measured value.

Unlike PCA where there exist algorithms to find the exact solution, NMF must be solved by an iterative optimisation algorithm [130]. Because iterative algorithms have a tendency to get stuck in local minima, it is important to use heuristics to ensure initialisation close to the global minimum. One method, particularly effective when only a few components are sought, is based on the singular value decomposition (SVD) of the data matrix M [131]. In some cases, such as when a particular feature is present in every sample, there is no unique solution [132]. However, the possible solutions will differ only in their assignment of that feature across the different components, so in practice the lack

of an unique solution does not matter.

Since the amount of any compound in the sample cannot be negative, and the real part of each compound’s NMR spectrum is also non-negative if the spectrum is correctly phased, NMF is intuitively a good choice for dimensionality reduction of NMR spectra. Although NMF is slower than PCA (indeed, solving for the optimal solution to NMF is NP-hard[†] [133]), it is still considerably faster than other methods of analysing NMR datasets — “four orders of magnitude faster than the Bayesian Markov chain Monte Carlo approach“ according to Sajda et al. [134]. NMF has been used on NMR time series [135], MRI image voxels [134] and the direct-dimension spectra of multidimensional NMR experiments [136].

The non-negativity of (the real part of) NMR spectra depends on correct phasing. With the narrow linewidths and stable spectrometer conditions found in solution NMR, this is a relatively easy condition to meet. For *in situ* NMR of electrochemical cells, however, it is much harder. Linewidths are wider and varying, and changes such as growth of dendrites on the lithium anode can affect the phase of the detected signal [137]. In any case, as shown by Elliott et al. [127] for PCA, fitting the entire complex signal rather than just the real part gives improved accuracy even if the phasing is correct to start with.

The Kramers-Kronig relations, which apply to the Fourier transform of any physical process where causality only operates forward in time, state that the imaginary part of the spectrum is uniquely determined by the real part and *vice versa*. Thus any given non-negative real spectrum has an associated imaginary spectrum which can be calculated and added to the real part to give an unique complex spectrum.

1.6.4 Implementation

Several software packages, both commercial and free/open-source, have PCA functionality, and many of these also support other matrix factorisations such as NMF. Some commercial NMR software packages such as MNova implement PCA, but in most cases authors do not seem to have used an NMR package. Some do not mention the software they are using (*e.g.* Stoyanova and Brown [138]), while others simply mention the programming environment used (*e.g.* Witjes et al. [129] use Matlab).

Open source software packages including PCA functionality include `scikit-learn`

[†]‘NP’ and ‘NP-hard’ are computational complexity classes. An ‘NP’ problem is a problem where a proposed solution can be checked in ‘polynomial time’ (*i.e.* in an amount of time that scales as a polynomial of the size of the problem *e.g.* $O(n)$ or $O(n^3)$). However, there is not in general a known method for finding a solution to the problem, or alternatively proving that there is no solution, in polynomial time. An ‘NP-hard’ problem is one which, if it can be solved in polynomial time, will allow all ‘NP’ problems to be solved in polynomial time. For NMF, this was demonstrated by converting a problem already known to be NP-hard into matrix form and showing that the NMF factorisation of that matrix can be used to solve the problem.

[139] and `MDP` [140] for Python, the `statistics` package for Octave [141], and the R language which has built-in PCA functionality [142]. Neither `scikit-learn` nor `MDP` is able to calculate PCA of complex-valued data, whereas the Octave package can. However, it was easier to modify the `scikit-learn` code to handle complex data than it would have been to port the code for reading the NMR data (see section C.3) to Octave or R, so an adapted and extended version of the `scikit-learn` code is used.

1.7 Research aims

As mentioned in subsection 1.2.1, published structures of lithium silicides (both model compounds and those formed electrochemically) have been derived solely from X-ray diffraction data, with no neutron diffraction data having been published. Lithium has a very low X-ray scattering cross-section compared to the heavier elements, but for neutron scattering there is less difference. In chapter 4, I describe the results of neutron scattering experiments on silicon-based battery materials, while in chapter 2 and chapter 3 I describe the development of new and improved software for analysing and processing these results.

NMR is a useful probe for local chemical structure, complementary to diffraction techniques. Because some of the phases formed during cycling of silicon against lithium are metastable and decay in the time required to prepare samples cycled *ex situ* [122], *in situ* experiments are needed to obtain information about these phases. Previous *in situ* NMR experiments with silicon-based electrode materials were unable to achieve even mediocre electrical capacity retention [122]. The use of electrodes based on silicon nanowires formed by CVD directly onto the current collector, together with improvements in cell construction, have allowed *in situ* NMR experiments (described in chapter 5) covering multiple electrochemical cycles. The ability to cover multiple electrochemical cycles is particularly important for silicon because the reaction profile in the first cycle differs from that in subsequent cycles (see subsection 1.2.2). These experiments not only required new software to analyse the data (described in subsection 1.6.4) but also required new code to be developed simply in order to open the data files (see Appendix C).

Chapter 2

Improvements to RMCprofile

RMCprofile uses RMC techniques to fit “big box” atom arrays to neutron and X-ray total scattering, EXAFS spectra, and other experimental data. Since anodes made from pure silicon without any binder or conducting filler show very poor electrochemical performance, the samples for the neutron diffraction experiments described in chapter 4 contained conducting carbon to increase conductivity. In addition, the SEI formed during cycling represents a third phase. The samples were therefore heterogeneous, with significant quantities of several different crystalline and non-crystalline structures.

The previous version of RMCprofile, version 6.5, could only model homogeneous samples, and extensive internal changes were needed to enable modelling heterogeneous mixtures (see section 2.5). At the same time, other changes were made to improve performance and to facilitate further development, following recognised software best practices (such as those proposed by Wilson et al. [143]) where feasible.

2.1 Profile-guided optimisation

The previous version of RMCprofile was run against some test data using the profiling tool `callgrind`, part of `Valgrind` [144]. Analysis of the output file with `KCacheGrind` showed that 92% of the central processing unit (CPU) time was spent in the `braggfunc` subroutine.

Moving as many of the calculations (especially the branch instructions) as possible outside of the inner loop made the subroutine, and therefore the whole RMCprofile program, run three times faster. However, even after this optimisation the `braggfunc` subroutine still accounted for the majority of the CPU time — the limiting factor after optimisation was the speed of transferring data between RAM and the CPU. Further optimisation would require reducing the amount of data to be transferred *i.e.* either the precision (using 32-bit instead of 64-bit floats), the number of data points for each Bragg peak, or the number of Bragg peaks.

2.2 Build system

The previous version of `RMCPprofile` used custom-written Makefiles to control the compilation and linking process. These files had to be maintained separately for every target platform (Linux, Mac, Windows *etc.*) and for every compiler.

`CMake` is a build system which allows automatically generating Makefiles for several platforms and compilers based on a single specification file. In most cases, it can automatically detect the dependencies between files, relieving the programmer of the responsibility of ensuring that the files are compiled in the right order.

`RMCPprofile` was changed to use `CMake` as a build system. `RMCCreate` (previously known as `data2config`) and the new `RMCanalysis` program were both included in the same build system, whereas they had previously been maintained separately.

2.3 Unit testing

In version 6 and earlier, the `RMCPprofile` codebase had no standardised testing procedures. The only way of checking that the program was functioning correctly was to run it on some known data and see if it gave sensible results. The classic article by Hatton [145], and much subsequent work, showed that this process is untrustworthy at best, and often amounts to no more than wishful thinking. Indeed, several bugs with the potential to cause silent data corruption were found in the previous version of `RMCPprofile` during the development process.

Several unit test frameworks were evaluated, but in the end it was decided that `CTest`, the testing framework built in to `CMake`, would be used. Some tests were written in Fortran and compiled as standalone executables. For increased productivity and comprehensibility of the test code, the more complicated tests were written in Python, using the `F2Py` interface generator [146] to make the Fortran code to be tested accessible from Python. This was especially helpful in the tests which required reading in test data and expected results from data files, as input/output is Fortran's weak point.

Hook and Kelly [147] points out that, while testing that individual units perform the calculations they are supposed to is relatively easy, integration testing of scientific software is often difficult because of the lack of 'oracles' (known correct results).

2.4 Modular architecture

While code for the previous version was split into modules, there was a lot of functionality duplicated in different modules (*e.g.* conversion from fractional coordinates to position in Angstrom was repeated in almost every module, sometimes with errors; calculation of

$G(r)$ and $S(Q)$ from the histogram was done in two or three different places, there were two routines to return the scattering length of an element, *etc.*). In addition, a lot of code made its way into the RMC main loop (as opposed to subroutines called from the main loop), making it over 2000 lines long and obscuring the most important parts.

`RMCprofile` version 7 has shared code concentrated in separate modules designed to maximise reusability. There is a `coordinates` module which handles all transformations between fractional and Cartesian coordinates, can determine distances (and bond and torsion angles) between pairs (triplets, quartets) of points while taking into account the effect of periodic boundary conditions, and also handles the conversion from Miller indices to a position in reciprocal space. The `atomtypes` module converts from character strings such as ‘7Li’ or ‘Fe2+’ to an internal representation which allows access to neutron scattering lengths, Q -dependent X-ray scattering factors, charges, atomic radii *etc.* The atomic data is contained in code automatically generated from a template Fortran source file and tabular data files published by international standards committees; it therefore allows easy updating if the published data is updated or the function interface has to be changed.

On the other hand, code which performs very specific functions and is not reused is also separated out. For example, there is a different module for each type of experimental data that `RMCprofile` can process. These modules only provide the functions that need to differ between experiment types; common routines such as reading in data files or calculating the χ^2 from the calculated function, the experimental data and the experimental errors are all shared. Because polymorphism with dynamic dispatch is a relatively recent feature in Fortran, not supported by many older compiler versions, I implemented “poor man’s dynamic dispatch” routines that look up the experiment number in an array that lists the type of each experiment then call the relevant routine from the appropriate module. For example, the `expt_calc_chi2` function will call `calc_gr` if the experiment is a ‘ $G(r)$ ’ (neutron real space data) experiment, but if it is a ‘Bragg’ experiment then `bragg_ycalc` is called. The `expt_calc_chi2` function then calls the `chi2` function to calculate the χ^2 before returning this to the RMC main loop.

Moving all this functionality to separate routines means that the RMC main loop subroutine itself is now just over 200 lines long, a tenfold decrease from version 6.

2.5 Multiple configurations

`RMCprofile` version 6 only supported single-phase systems. Because of the way in which functionality was duplicated throughout the codebase (see section 2.4), enabling support for multiple phases was not just a simple matter of changing a few lines but required rewriting most of the core code. In the end it was decided to reimplement the core

functionality in its entirety, which allowed increased modularisation (see section 2.4) and also meant that the authorship was more clear (development up until version 6.5 had been done without any kind of version control software, meaning that there was no consistent record of who had done what), which simplifies the process of obtaining permissions to release the code as open source.

The new internal representation of atomic configurations removed the requirement for atoms to be sorted by element. This therefore meant that ‘atom swap moves’ (used in modelling substitutional disorder in crystal or lattice structures) can be implemented by swapping the elements of the atoms concerned rather than their positions. This means that the spatial relationships (bond lists *etc.*) of atoms remain the same, facilitating interaction with external tools such as `GASP` [148].

2.6 Improved compatibility with Condor

`Condor` [149] is a scheduling system for high-throughput computing. Among other features, it allows submission of long-running jobs to a cluster, checkpointing jobs with rollback to the most recent checkpoint in the event of system failure, migration of jobs between nodes before scheduled shutdowns, and automatic forwarding of the job’s input and output to and from the submitting node. However, many of these features make certain restrictions on the behaviour of the program, particularly in order to ensure consistent behaviour when a file is processed twice because execution has been rolled back to a checkpoint before it was processed. `RMCprofile` version 6 did not obey these restrictions, and was therefore only able to use a restricted subset of `Condor`’s features. `RMCprofile` version 7 is fully compatible with `Condor`’s “standard universe”.

Additionally, to take full advantage of `Condor`, the program being submitted as a job must be recompiled using the special `condor_compile` wrapper, which can only be done if the source code is available to users. Since `RMCprofile` version 7 is (or rather will be) open-source, this is now possible for all users rather than just those with privileged access to the source code.

2.7 Explicit uncertainty information in data files

Measurements of $S(Q)$ do not have the same accuracy over the entire Q range. High count rates have a \sqrt{N} standard error, so the height of peaks will be less certain than the depth of the adjacent baseline. The high Q region, corresponding to high scattering angles (which have less solid angle) and higher energies (with much less flux than at longer wavelengths), will have a smaller denominator when normalising to b/atom/sr and thus the uncertainty in $S(Q)$ will be higher. This variation in uncertainty over the $S(Q)$ range

will feed through into the $G(r)$ data. To calculate an accurate χ^2 goodness-of-fit between the RMC model and the experimental data, it is therefore essential to take into account the variation in uncertainty over the data range.

Although it could read in data on the uncertainty (standard error) where the file format included that information, `RMCprofile` version 6 did not use that uncertainty data when calculating the χ^2 . When the file format did not contain uncertainty information, there was no way it could use that data even if it had the capability to. `RMCprofile` version 7 requires uncertainty data to be present in experimental data files (see subsection 2.8.2), with the exception of `.bragg` files, and uses that data when calculating χ^2 . This is made easier by having a single `chi2` function (see section 2.4) rather than different code calculating the χ^2 depending on which data type is being used and whether it is being calculated for the RMC Metropolis criterion or for saving files, as was the case in version 6.

2.8 Functionality that has been removed

2.8.1 Automatic calculation of neighbour lists

`RMCprofile` version 6 would automatically generate a neighbour list (`.neigh`) file if a `DISTANCE_WINDOWS` constraint was specified but no `.neigh` file was present. This caused problems when restarting long-running calculations from checkpoints (see section 2.6) because some second-nearest-neighbours had drifted inside the outer distance limit for first-nearest-neighbours and were therefore included in the list of first-nearest-neighbours, which prevented them from drifting back out again. Eventually the list of supposed ‘first-nearest-neighbours’ became so long that the hardcoded maximum was exceeded and `RMCprofile` crashed.

For this reason, generation of neighbour lists (and similar files such as lists of bond angle constraints) has been removed from the main `RMCprofile` program and must now be done with the `RMCcreate` suite of tools.

2.8.2 Automatic conversion of `DATA_TYPE` and `FIT_TYPE`

`RMCprofile` version 6 allowed its input data to be provided in a variety of formats, both in terms of the layout of the data within the file and whether the data represented $G(r)$, $D(r)$, $T(r)$, normalised or unnormalised and so on. It also allowed setting a `FIT_TYPE` different from the data in the file, requiring both the experimental and the calculated scattering patterns to be transformed. This led to an unnecessary profusion of possible code paths, which would have made unit testing much more laborious. In version 7, the `RMCprofile` executable will only accept a single file format for experimental data,

which must be represented as unnormalised $D(r)$ for real space data or unnormalised $Q_i(Q)$ for reciprocal space, and must include information on the statistical uncertainty of these data (see section 2.7). The `convertdata.py` script, part of the `RMCcreate` suite of tools, must be used to convert other file formats and other representations into these two. Taking advantage of Python being much better suited than Fortran for rapid development involving the processing of text files, support for additional file formats was added with ease — for example: adding support for the data files from the Spallation Neutron Source (including full metadata) required only five additional lines of code.

2.8.3 Temporarily removed functionality

Some functionality of `RMCprofile` version 6 was omitted from version 7.0 not because it was thought undesirable but because of insufficient developer time to convert the code to the new modular architecture (see section 2.4) and to handle multiple configurations. In particular, support for fitting to EXAFS spectra and diffuse electron diffraction patterns was removed, as were bond valence sum (BVS) constraints. This functionality, along with additional constraints, potentials and experimental data types, will be added in subsequent releases. It is hoped that the open source nature of `RMCprofile` version 7 will facilitate collaboration with external authors who will contribute new functionality.

2.9 Validation

To ensure that calculations with `RMCprofile` version 7 will give similar results to the same calculations done with `RMCprofile` version 6, trial jobs were run on two model systems based on synthetic data. The ‘version 6’ calculations were done with `RMCprofile` version 6.5.2, downloaded from the `rmcprofile.org` website as a compiled binary, as the source code for this version has not been made available to the version 7 developers. The ‘version 7’ binary was compiled from source, using revision 1338 of the QMUL subversion repository.

2.9.1 Atom swap moves

This experiment compares the abilities of the two `RMCprofile` versions to reconstruct clustering of atoms by ‘swap moves’ between crystallographic sites. Because clustering of elements with different scattering lengths leads to changes in the height of the $D(r)$ peaks relative to a random arrangement, an RMC fit to a $D(r)$ pattern can potentially be used to reconstruct this clustering.

To generate the synthetic data, a supercell of $10 \times 10 \times 10$ body-centred cubic (BCC) unit cells (2000 atoms), with lattice parameter 3.0 \AA was filled with a mixture of 90% cobalt atoms and 10% nickel atoms. (This is not meant to represent the structure of any

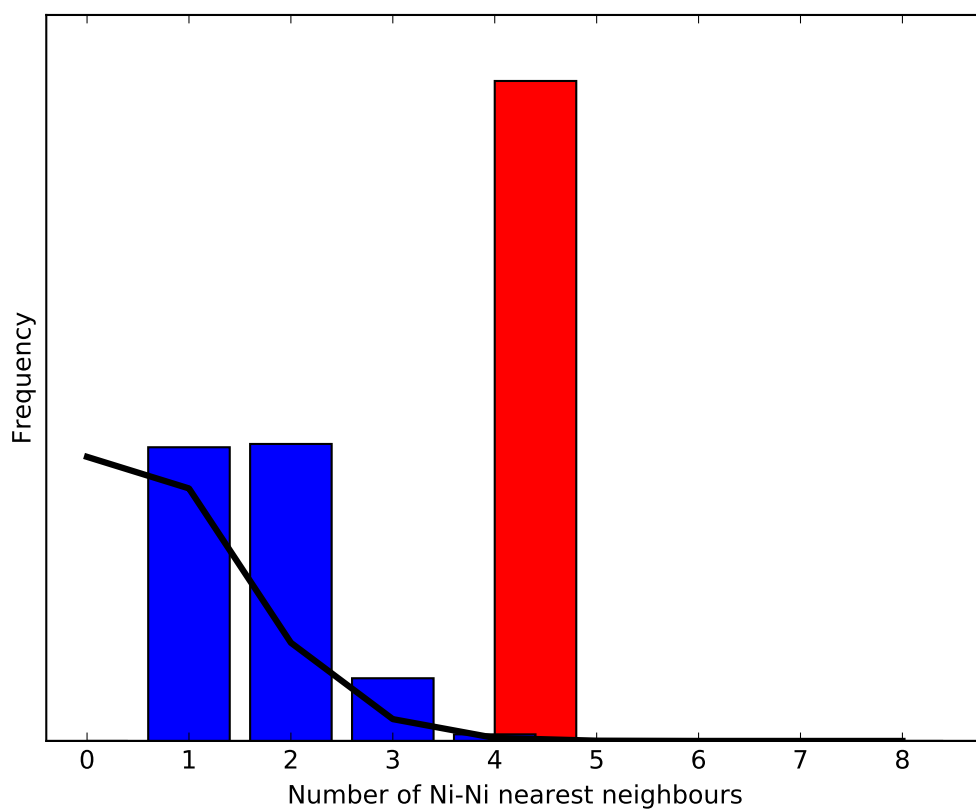


Figure 2.1: Histograms: for each nickel atom, how many of its nearest neighbours are also nickel? Blue: 'target' structure, red: initial structure for refinement, black line: expected distribution under random arrangement of atoms.

real cobalt-nickel alloy, these elements were only chosen because they have very different scattering lengths – 2.5 fm for Co *vs* 10.3 fm for Ni.) The nickel atoms were added in pairs, so that every nickel atom had at least one nearest neighbour that was also nickel. Each atom was then displaced in all three dimensions by random distances chosen from a uniform distribution over $\pm 0.1 \text{ \AA}$. The theoretical $D(r)$ from this ‘target’ structure was calculated by passing it to `RMCprofile` v7, “fitting” it against an arbitrary dataset but with an iteration limit of zero.

The starting structure for the fits with `RMCprofile` v6 and v7 was the ideal unrandomised BCC supercell, with all the nickel atoms together in the cells on one face of the cube. This starting structure was then fitted against the simulated $D(r)$ pattern, with distance window constraints used to maintain the overall lattice structure.

2.9.2 Bending distortions

This experiment compares the abilities of the two `RMCprofile` versions to reconstruct ‘bending’ distortion away from average lattice positions. A displacement in the plane normal to the vector between the average atomic positions will lead to an average bond length in the $D(r)$ longer than predicted by the crystal structure, and RMC can potentially be used to reconstruct this kind of disorder.

To generate the synthetic data, a supercell of $8 \times 8 \times 8$ perovskite-like unit cells (only the BX_3 of a cubic perovskite structure ABX_3 with B in the octahedral holes) with lattice parameter 4.0 \AA was created, with Sn in the B sites and O in the X sites (512 Sn atoms and 1536 O atoms). (Again, this is not supposed to represent the structure of any real-life material, merely as an example of a possible target problem.) Each O atom was displaced 0.5 \AA in a randomly chosen direction within the plane normal to the vector between its two neighbouring Sn atoms. The Sn atoms were then displaced from their lattice sites by a uniform random vector within the range $\pm 0.1 \text{ \AA}$. The theoretical $D(r)$ was then calculated as described in subsection 2.9.1.

`RMCprofile` v6 and v7 were then used to fit against the calculated $D(r)$, using the ideal unrandomised structure as the starting point for the optimisation. Distance window constraints were used to avoid disruptions to the overall lattice structure.

2.9.3 Heterogeneous mixture

To check `RMCprofile` v7’s ability to handle heterogeneous mixtures, a further fitting run was done, simultaneously fitting the two systems described in subsection 2.9.1 and subsection 2.9.2 against a single dataset calculated from the two ‘target’ configurations.

2.10 Results of validation runs

2.10.1 Atom swap moves

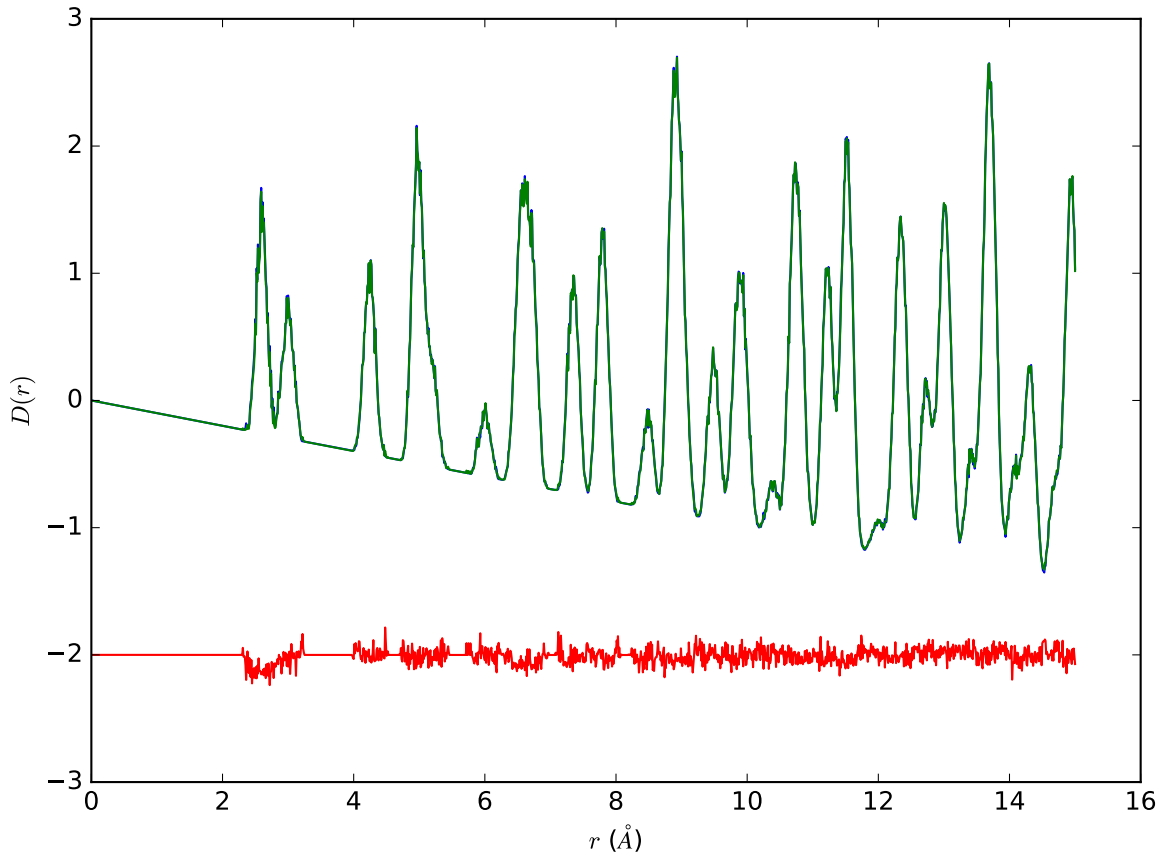


Figure 2.2: $D(r)$ fit for the BCC Cobalt-Nickel system with `RMCPProfile` version 6. Blue: ‘target’ $D(r)$, green: fitted $D(r)$, red: difference, scaled by a factor of five and offset.

The graphs of the $D(r)$ curves in Figure 2.2 and Figure 2.3 show that both versions of `RMCPProfile` were able to find close fits to the target pattern. However, since there are many possible structures that can give rise to any given $D(r)$ curve, it is also necessary to see whether the structural features of the ‘target’ structure can be reconstructed.

For each of the structures output by the simulation runs, the number of nearest neighbours of each element was calculated (*e.g.* for each nickel atom, how many of its nearest neighbours are nickel and how many are cobalt). These statistics are presented in Figure 2.4. Both fitted structures have broader histograms than the target structure, which is to be expected as the $D(r)$ only contains information about the average coordination.

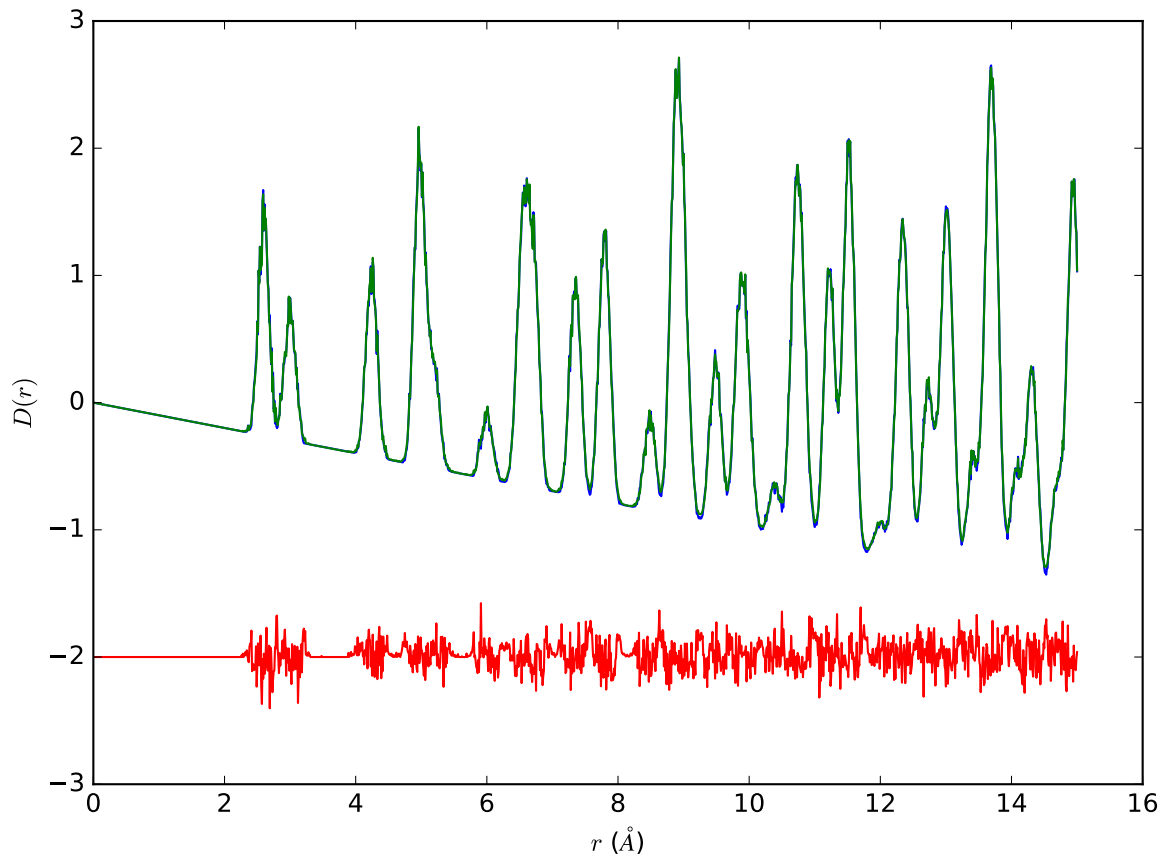


Figure 2.3: $D(r)$ fit for the BCC Cobalt-Nickel system with RMCProfile version 7. Blue: 'target' $D(r)$, green: fitted $D(r)$, red: difference, scaled by a factor of five and offset.

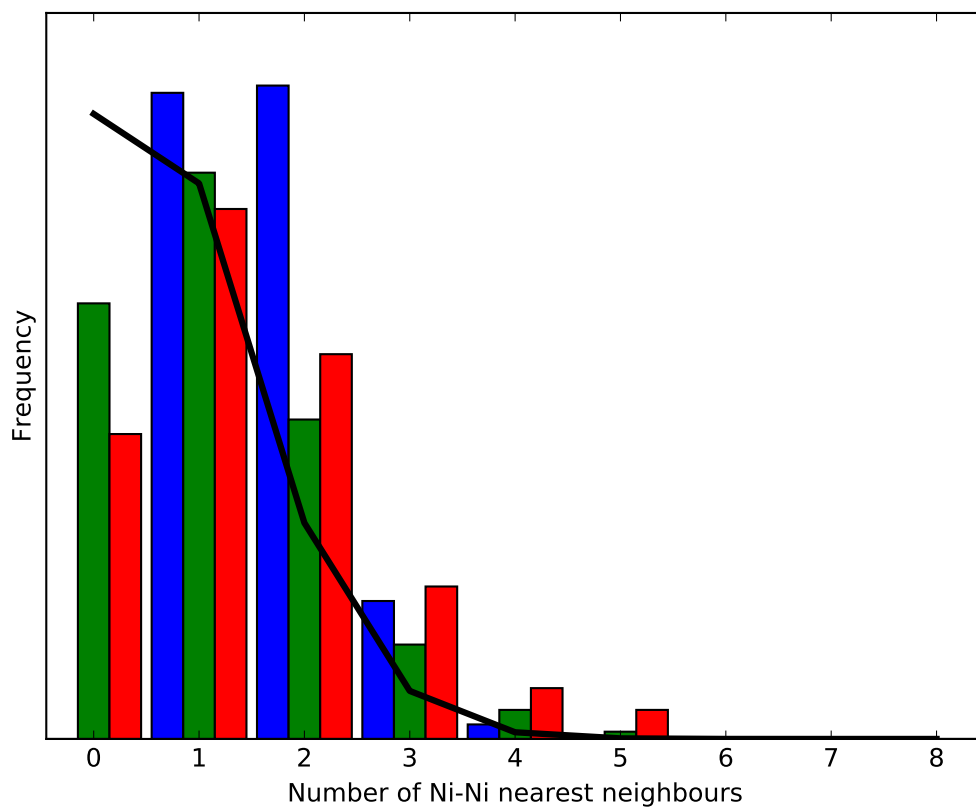


Figure 2.4: Histograms: for each nickel atom, how many of its nearest neighbours are also nickel? Blue: ‘target’ structure, green: refined with `RMCPProfile` version 6, red: refined with version 7, black line: expected distribution under random arrangement of atoms.

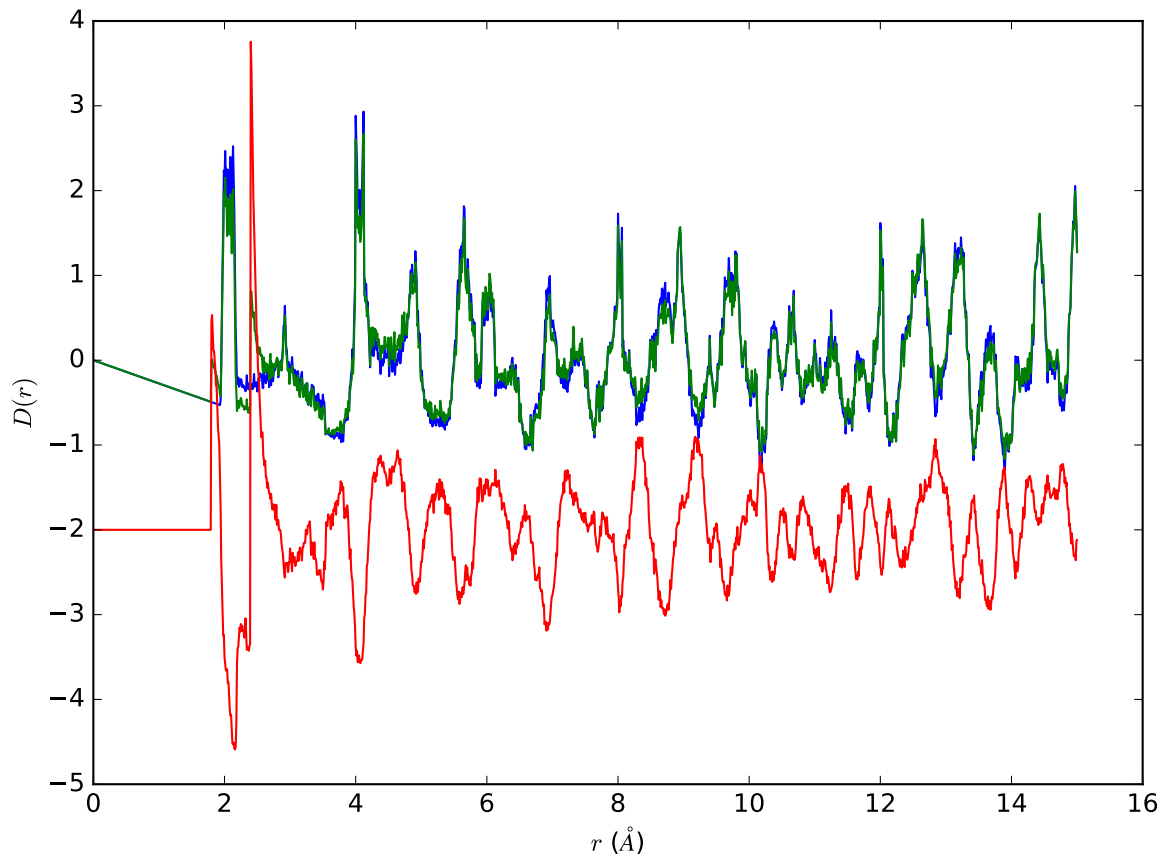


Figure 2.5: $D(r)$ fit for the perovskite-like system with RMCProfile version 6. Blue: 'target' $D(r)$, green: fitted $D(r)$, red: difference, scaled by a factor of five and offset.

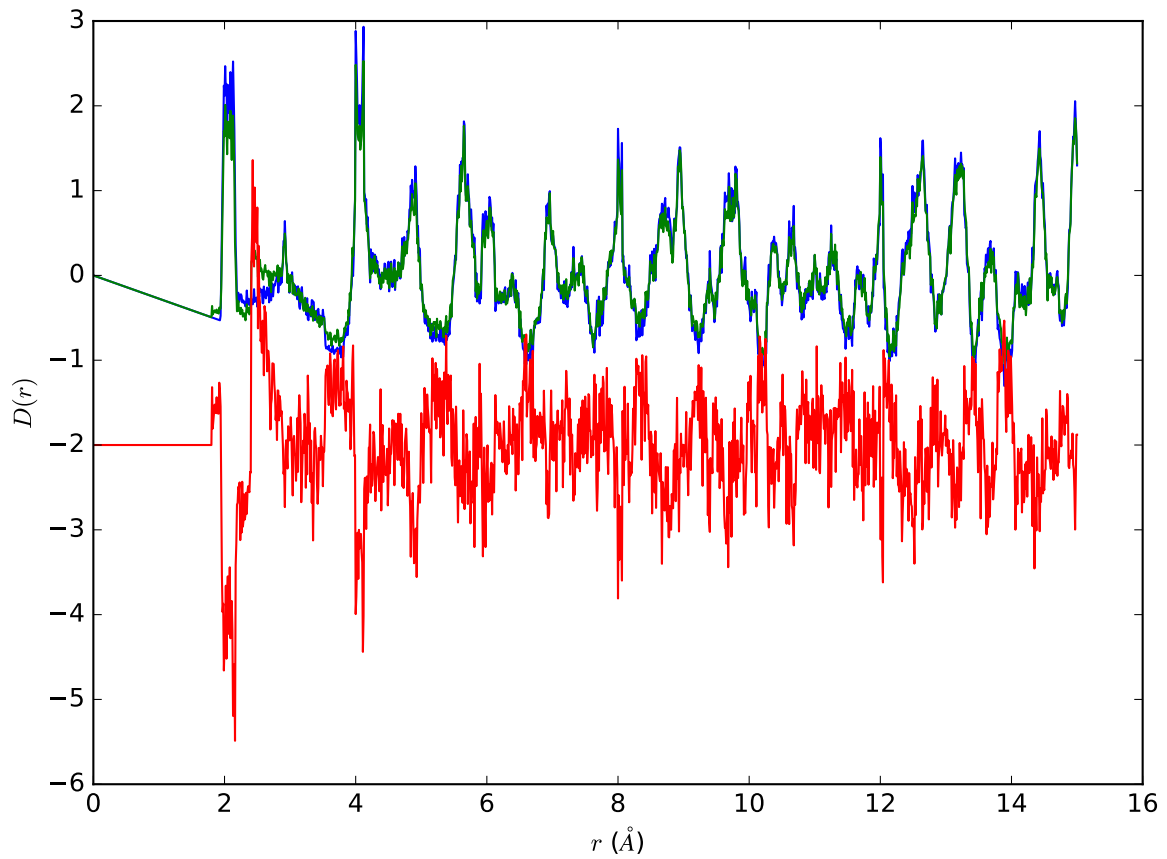


Figure 2.6: $D(r)$ fit for the perovskite-like system with RMCProfile version 7. Blue: 'target' $D(r)$, green: fitted $D(r)$, red: difference, scaled by a factor of five and offset.

2.10.2 Bending distortions

In this case both refinement runs (Figure 2.5 and Figure 2.6) showed worse fits, with the peaks being smeared out and intensity appearing in side peaks. A possible explanation is that this system had more empty space to allow freedom of movement despite the distance window constraints.

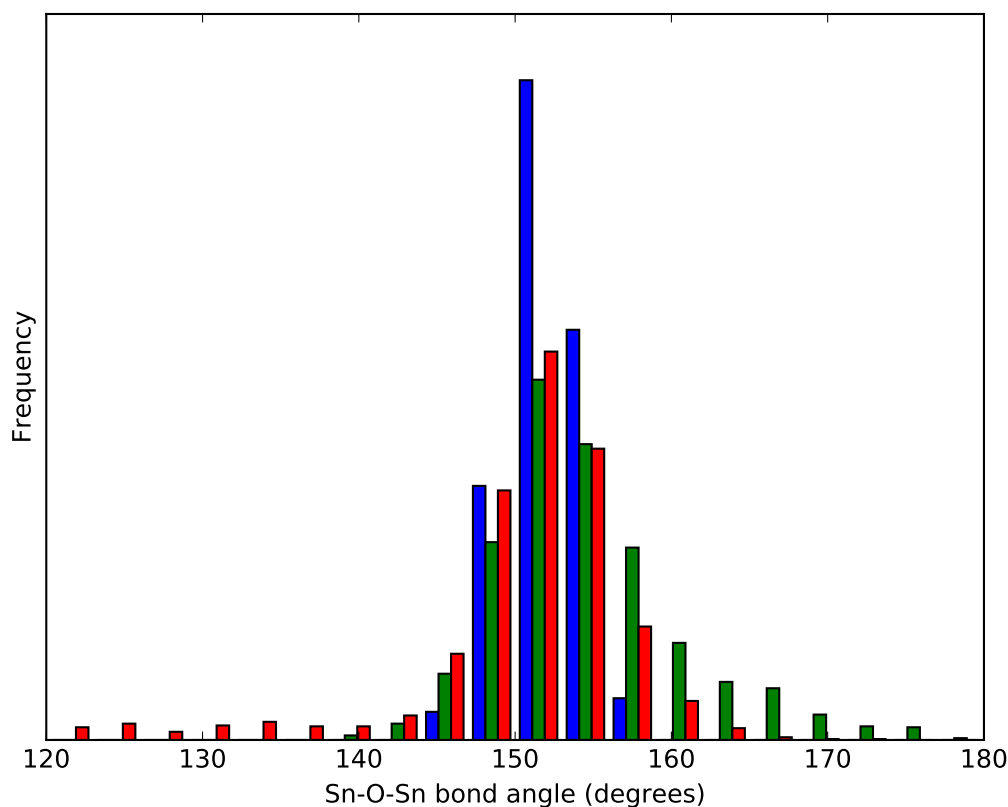


Figure 2.7: Sn–O–Sn bond angle distribution. Blue: ‘target’ structure, green: refined with RMCPProfile version 6, red: refined with version 7.

Figure 2.7 shows the Sn–O–Sn bond angle distribution in the ‘target’ and refined structures. Here again the histograms from the refined structures are broader than from the ‘target’ structure. Interestingly, the refinement with version 6 gives a long tail of angles larger than in the ‘target’ structure, whereas the refinement with version 7 gives a tail with narrower angles.

2.10.3 Heterogeneous mixture

Figure 2.8 shows the $D(r)$ fit for the heterogeneous mixture system described in subsection 2.9.3. (There is no graph for RMCPProfile version 6 because version 6 does not

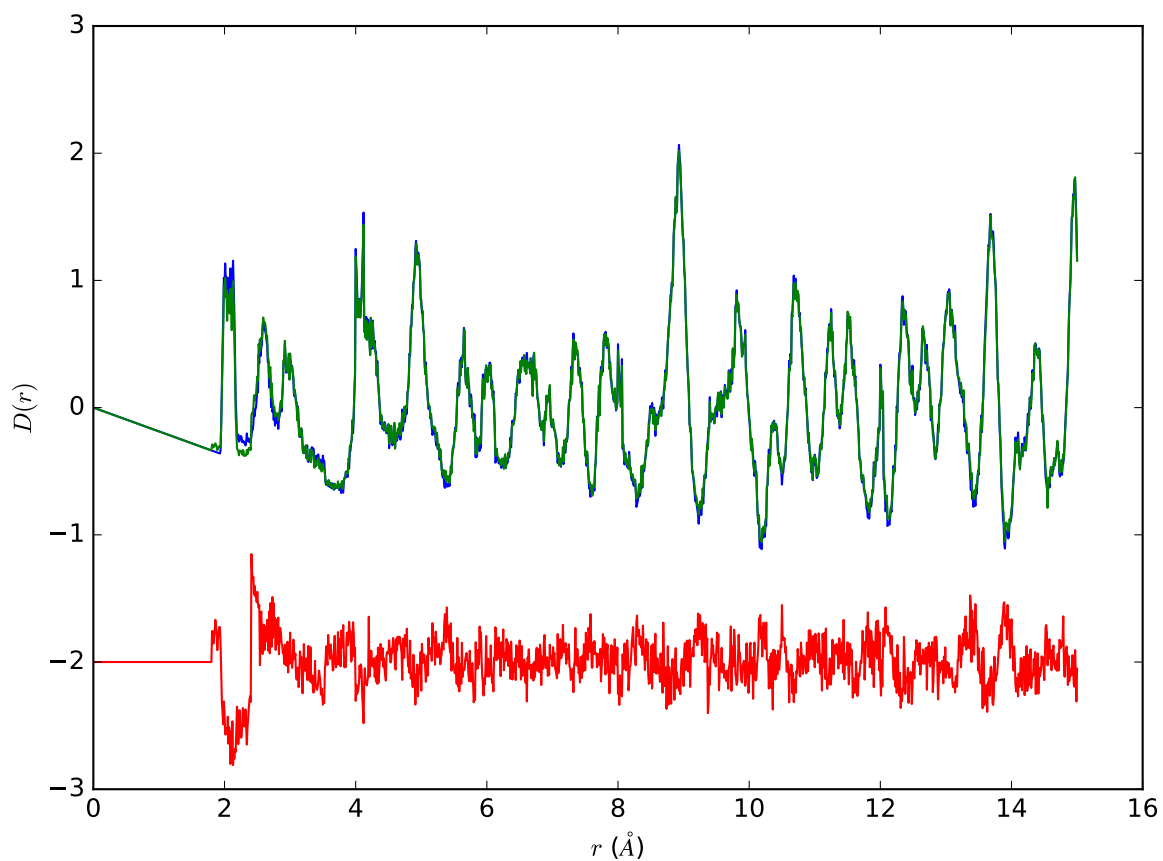


Figure 2.8: $D(r)$ fit for the mixture with RMCProfile version 7. Blue: ‘target’ $D(r)$, green: fitted $D(r)$, red: difference, scaled by a factor of five and offset.

support mixtures). The additional degrees of freedom allowed for a mostly very good fit, although there is still a problem with broadening around the first (Sn–O) peak.

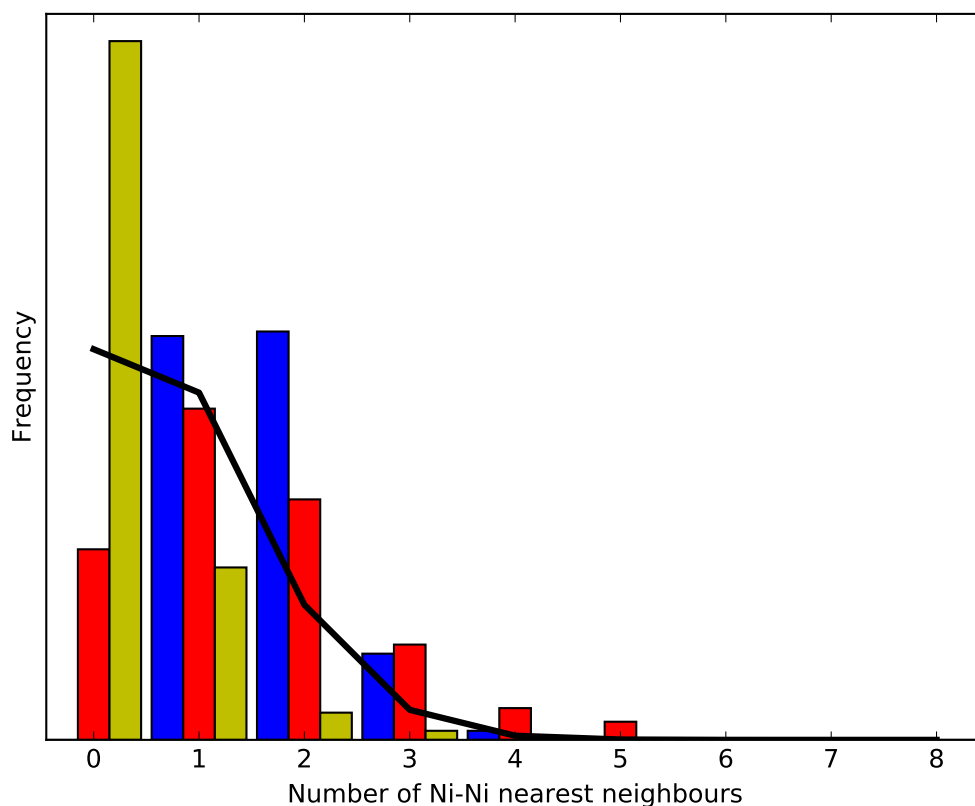


Figure 2.9: Histograms: for each nickel atom, how many of its nearest neighbours are also nickel? Blue: ‘target’ structure, red: single system refinement (same data as Figure 2.4), yellow: structure obtained by simultaneous refinement, black line: expected distribution under random arrangement of atoms.

For the ‘atom swap’ system, the results (Figure 2.9) from the combined “heterogenous mixture” refinement are clearly worse than from single structure refinement. In fact, they are even further from the ‘target’ structure than would be expected for a completely random arrangement of atoms. However, for the ‘bending distortions’ system the combined refinement has actually given better results, with the distribution of bond angles more closely centred on the ‘target’ structure. Possibly the interference with the results in the ‘atom swap’ system is due to the nearest neighbour peak in that system overlapping with the broad O–O peak in the ‘bending distortions’ system.

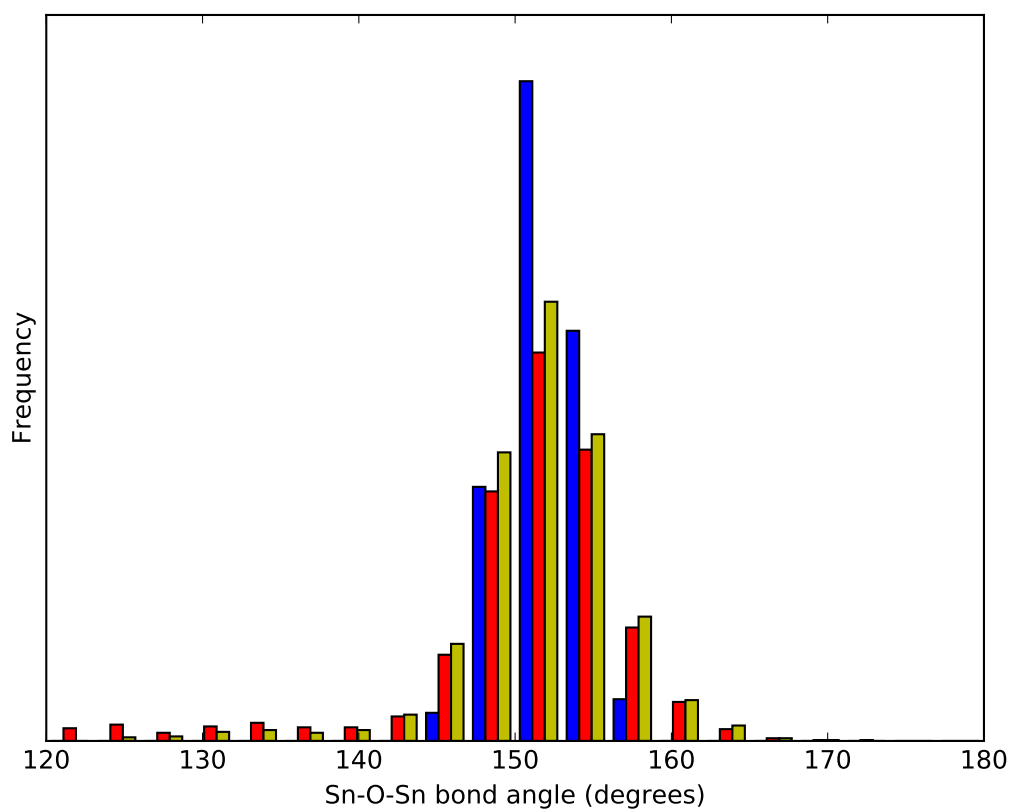


Figure 2.10: Sn–O–Sn bond angle distribution. Blue: ‘target’ structure, red: single system refinement (same data as Figure 2.7), yellow: structure obtained by simultaneous refinement.

2.11 Conclusions

The output of the new version 7 of `RMCprofile` on single component systems is broadly comparable to that of the most recent released version 6.5.2. This is unsurprising, as the algorithm used is essentially identical, but useful as a validation of the new version's functionality.

Refinement with heterogeneous mixtures seems however to be more hit-and-miss, especially when peaks from one system overlap with those from another system. For more reliable performance, additional constraints or restraints could be used, or multiple data-sets could disambiguate overlapping peaks.

Chapter 3

Deconvolution of the resolution function

Real instruments cannot measure an $S(Q)$ exactly (see subsection 1.3.7). Instead, the measured scattering intensity will have to be corrected for several effects, including detector noise, scattering from other parts of the instrument, multiple scattering, and many others. Some of these effects manifest as a background which can be subtracted, or a scaling factor which can be dealt with by multiplication. However, effects which tend to broaden or smear out the scattering cannot be fixed so easily. If the broadening is constant over the entire Q range, deconvolution can be done by a Fourier transform. However, this approach is no longer valid when the resolution function changes significantly from one part of the data to another. In the case of data from ToF diffractometers, the process is made even more complicated by the fact that different banks will have different resolution functions even at the same Q point.

Previous implementations of software to deconvolve this smearing effect have all used Metropolis Monte Carlo methods. Pusztai and McGreevy [106] created MCGR (Monte Carlo $G(r)$) to solve for a $G(r)$ matching a given $S(Q)$ using Metropolis Monte Carlo methods. Tucker et al. [107] modified MCGR to fit $S(Q)$ data acquired on ToF instruments, using the peak profile function from Ikeda and Carpenter [150] and the pseudo-Voigt function from Thompson et al. [151], as adapted by GSAS [152, pp 144–147]. The modified program is called MCGRtof.

Both these implementations can also add several other constraints, for example pre-defined values of $G(r)$ in the low r and high r limits, to guide the fitted $G(r)$ to a more physically realistic form.

3.1 Matrix formulation and linear least-squares solution

3.1.1 Ideal case

The transformation from $D(r)$ to an ideal $S(Q)$ is a Fourier transform – more specifically a sine transform. (Technically the result of the sine transform is $QF(Q)$, but the relationship between this and $S(Q)$ is linear). The continuous functions $D(r)$ and $S(Q)$ are typically represented in a computer by samples (represented below as D_j and S_i) of their values at regularly spaced r or Q points (r_j and Q_i) within a certain range. If the ranges and sampling intervals obey certain rules, the fast Fourier transform (FFT) algorithm can be used to perform the transform. Alternatively, and for arbitrary r and Q spacings, the calculation can be done directly (n_r is the number of r points and n_Q is the number of Q points):

$$S_i = S^0 + \sum_{j=1}^{n_r} D_j \frac{\sin(Q_i r_j)}{Q_i} \quad (3.1)$$

The value $\sin(Q_i r_j)$ can either be calculated every time or precomputed and stored in a matrix of size $n_Q \times n_r$.

3.1.2 Resolution function

To take into account the finite resolution and irregular Q -dependent peak shape, each data point in the $S_{\text{ideal}}(Q)$ array must be replaced with a broadened function which in general can be expressed as $P(Q_{\text{ideal}}, \Delta Q)$ (where $\Delta Q = Q_{\text{real}} - Q_{\text{ideal}}$), or equivalently as $P'(Q_{\text{ideal}}, Q_{\text{real}})$.

$$S_k = S^0 + \sum_{i=1}^{n_Q} \sum_{j=1}^{n_r} D_j \frac{\sin(Q_i r_j)}{Q_i} P'(Q_i, Q_k) \quad (3.2)$$

The values of $\sum_{i=1}^{n_Q} \sin(Q_i r_j) P'(Q_i, Q_k)$ can be precomputed and stored in a matrix M_{kj} such that $S_k = \sum_{j=1}^{n_r} M_{kj} D_j$ or, in matrix notation, $S = \mathbf{M}D$. This means the problem of finding a $D(r)$ such that the resulting calculated $S(Q)$ most closely matches a given measured $S(Q)$ is a linear least squares problem (ordinary least squares if all the S values are known to the same precision, otherwise a weighted least squares problem). Additionally, several typical constraints on physically realistic $D(r)$ values, such as fixed values below a particular minimum r , maximum peak sharpness, or tending to zero at high r , can be imposed or at least approximated in the form of a matrix, meaning that these constraints can also be taken into account by a linear least squares solver.

3.1.3 Linear least squares solvers

Linear least squares problems are typically solved computationally by a method based on the Moore-Penrose pseudo-inverse [153, 154].

I chose to use an implementation in the Python `statsmodels` package [155] (formerly known as `scikits-statsmodels`). The source code of `statsmodels`' weighted least squares solver cites Montgomery and Peck [156] as the source of the algorithm used.

3.2 Example: crystalline aluminium phosphate

To facilitate comparison, the same data were used as in the `MCGRtof` paper [107]: ToF neutron scattering data from crystalline AlPO_4 (see appendix A.2.1 for more details). In the `ProfFitS` fit, a minimum r constraint of 1.2 \AA (same as in the `MCGRtof` calculations) was used, together with a minimum Q of 1.0 \AA^{-1} and a weak smoothness constraint.

3.3 Results

A comparison of the results of fitting the AlPO_4 data with `MCGRtof` and with `ProfFitS` can be seen in Figure 3.1 and Figure 3.2.

In Figure 3.1 it can be seen that both `MCGRtof` and `ProfFitS` succeed in correcting for the drop-off in the $D(r)$ at higher r due to the instrumental broadening. (This effect also appears when the data from the higher-angle banks are used, but here the data from the lowest-angle bank were used to emphasise the effect.)

It was found that unphysical large-amplitude low-frequency oscillations would appear in the $D(r)$ towards high values of r unless the scattering at low Q was constrained to zero at a much higher density of Q points than were present in the rest of the data. An example of this large-amplitude oscillation can be seen in the `MCGRtof` $D(r)$ in the region $r > 60 \text{ \AA}$ of Figure 3.1 — the `MCGRtof` fit uses the same Q spacing for the projected low Q data as for the experimental data at higher values of Q . The oscillations that appear when fitting with `ProfFitS` are much larger, as they are not constrained by the fact that `MCGRtof`'s random walk process would take a very long time to reach large values of $D(r)$. However, when using a Q spacing of 0.002 \AA^{-1} for the zero scattering at low Q , one tenth of the Q spacing of the experimental data, these oscillations are no longer seen.

3.4 Discussion

The `MCGR` and `MCGRtof` programs were not used much because they took too much time to run (*e.g.* two days for the `MCGRtof` calculation in [107]). Doing the same calculation with

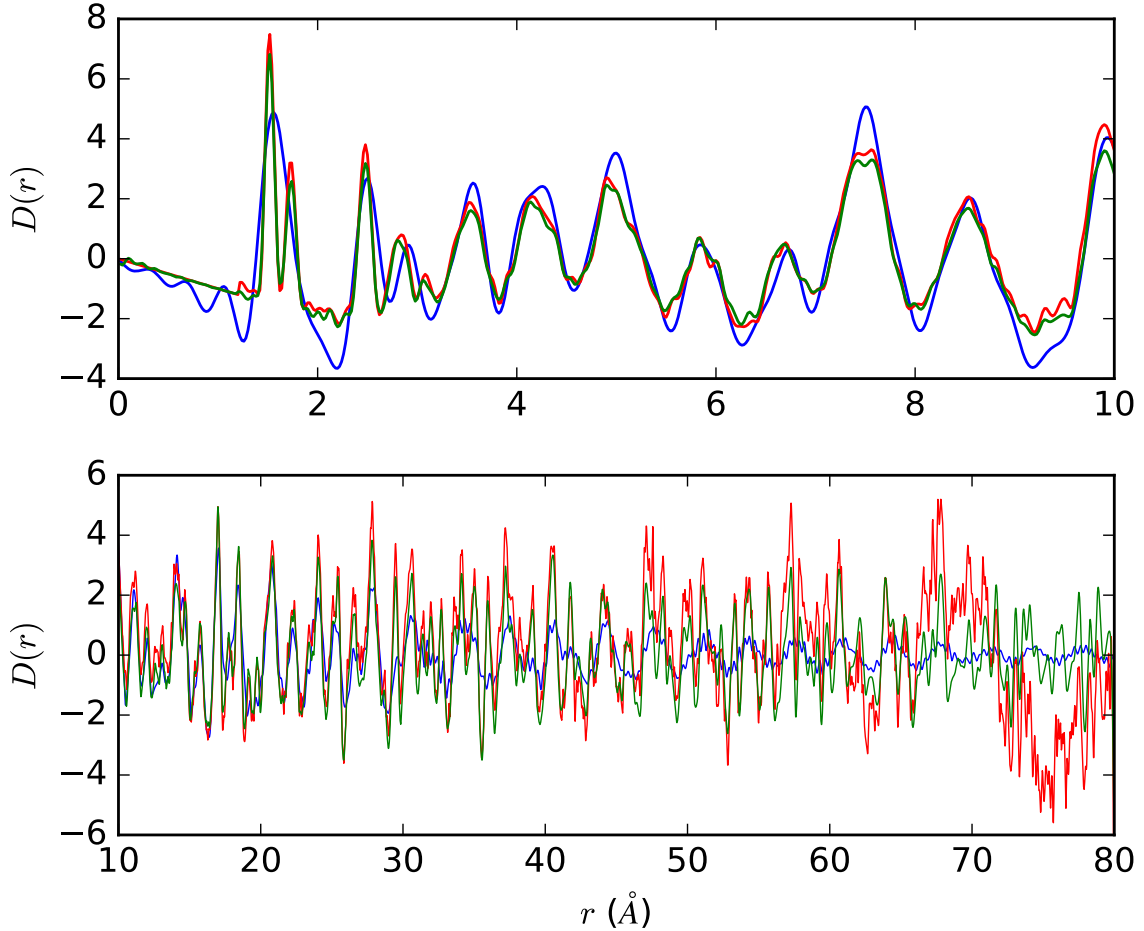


Figure 3.1: $D(r)$ — Direct transform from the bank 2 $S(Q)$ data (blue), fitted with MCGRtof (red) and with ProfFitS (green). The direct transform (blue) shows broadening of the peaks, due to the limited Q range of this bank of data, and a drop-off in intensity at higher r , due to the instrumental resolution function not having been corrected for.

ProfFitS takes 90s on a modern workstation with OpenMP parallelisation enabled and using optimised BLAS and LAPACK libraries [157], meaning it is now much more practical to use it as part of a workflow for analysing large numbers of scattering patterns. Its memory requirements (in the range 1 GB to 10 GB, depending on the number of r points, the number of Q points and the number of additional constraints) would have been prohibitive when MCGR was first published in 1999, but are now within the capabilities of recent desktop and laptop machines.

The ProfFitS code can also provide estimated uncertainties for the $D(r)$ data, which will allow programs such as RMCprofile which use the $D(r)$ data to calculate a more accurate χ^2 goodness-of-fit test when comparing model with experiment.

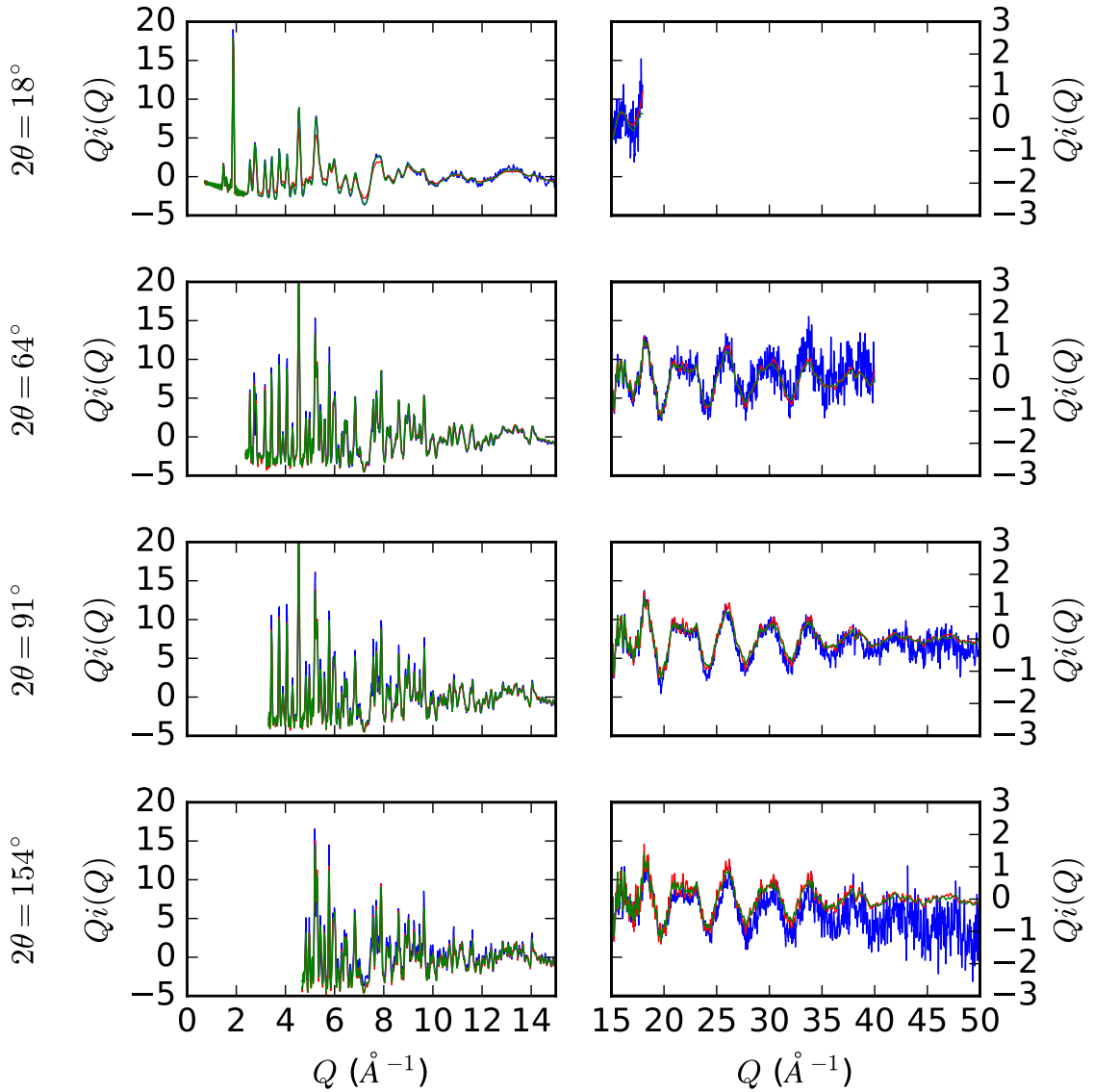


Figure 3.2: $Q_i(Q)$ — experimental (blue), MCGRtof (red) and ProfFitS (green). Each row of the figure corresponds to a detector bank at a different 2θ angle (namely banks 2, 4, 5 and 7 of GEM at ISIS — see appendix A.2.1 for details). The left and right columns show the low and high Q regions of the same $Q_i(Q)$ curves, but with differently scaled axes. The banks at lower angles can record data at lower values of Q but have a broader resolution function. The banks at higher angles can record data at higher values of Q and have, for a given Q , narrower resolution functions.

Chapter 4

Neutron diffraction and RMC studies on silicon anode materials

There have been many studies (*e.g.* [58] or [158]) taking X-ray powder diffraction patterns of lithium silicide based anode materials either *in situ* during the battery cycling process or *ex situ* at specific points in the cycle. However, many of the intermediate phases in the lithiation and delithiation process are amorphous, meaning that standard powder diffraction methods such as Rietveld refinement [104] do not provide useful information.

Real-space methods such as pair distribution function (PDF) analysis, on the other hand, can provide information about the atomic arrangements even in amorphous materials. Key et al. [159] took X-ray PDF patterns of silicon-based anode materials at several stages in the charge-discharge cycle. However, lithium scatters X-rays very weakly, particularly at the high Q ranges needed to obtain accurate PDFs. With neutrons, on the other hand, lithium's scattering length is of similar magnitude to that of heavier elements such as carbon or silicon. In addition, ^7Li scatters with the opposite phase from most other nuclides (expressed as a negative scattering length) meaning that peaks due to correlations between lithium and other atoms are particularly easy to spot in the PDF. Despite these advantages, no papers with neutron PDF data on lithium silicide anode materials have been published as of 30 June 2014.

This can possibly be explained by the difficulties in sample preparation. Because of its strong incoherent and inelastic scattering, samples containing normal ^1H hydrogen will not give a good-quality PDF. Any hydrogen-containing materials used in sample preparation must therefore be deuterated. The ^6Li isotope of lithium, which has a natural abundance of around 7.5%, absorbs neutrons and produces radioactive tritium, so depleted lithium (*i.e.* pure ^7Li) must be used. The requirement to use depleted lithium is not particularly onerous, but full deuteration is much more challenging.

Typical silicon-based electrode formulations will contain conductive carbon additives and an organic binder as the electrochemical performance of pure silicon electrodes is very

poor ([71] or see subsection 1.2.2). The conductive carbon does not contain significant amounts of hydrogen, but the organic binder does. In addition, the SEI formed during cycling will incorporate any hydrogen in the electrolyte.

Deuterated isotopologues of the organic components of the electrolyte, DMC and EC, are commercially available, with d4-EC being much more expensive at around £1000 per gram. The complex organic polymers used as binders, on the other hand, are not available in deuterated form. Indeed, the synthesis of deuterated isotopologues of biopolymers such as CMC would require deuterating the entire organism from which the polymer is extracted. Although this has been done for (partial) ^{13}C enrichment [160], the large kinetic isotope effect of deuterium disrupts metabolic reactions to such an extent that deuteration above 50 % is fatal to eukaryotic organisms (but not to prokaryotes and archaea, some of which can survive and grow in fully deuterated media [161]).

Consequently, no binder was used in the electrode formulation for these experiments. Instead, very low current densities were used so as to minimise the level of ‘electrochemical shock’ [42] experienced by the electrode material.

4.1 Methods

Note that, although silicon is considered an anode material, when cycling against a lithium metal counter electrode it acts as a cathode and will be referred to as such for the remainder of this chapter. Likewise ‘discharge’ refers to current flowing from the lithium metal anode to the silicon-based cathode, lithiating the silicon, and ‘charge’ refers to the delithiation process.

4.1.1 Preparation of active material

A 50:50 w/w silicon-carbon mixture was prepared by milling 325 mesh silicon powder (Aldrich) and Super P Li carbon (Timcal) in a stainless steel ball mill jar for 2×30 min at 300 rpm in a Retsch PM100 planetary ball mill. Note that, according to experiments by Gauthier et al. [162], ball milling for up to 20 h does not result in incorporation of measurable amounts of iron from the ball mill jar or balls into the product.

4.1.2 Assembly of Swagelok cells

Swagelok cells are constructed from a Swagelok[®] 180° pipe join with the following modifications:

- The neck in the middle of the join has been bored through, so the internal diameter is constant.

- Instead of pipes, solid cylindrical current collectors are inserted into each end of the join. One end of each current collector is in contact with its respective electrode, and the other end is connected via a crocodile clip to the battery cycler.
- The metal olives which grip the sides of the pipe/plunger have been replaced with non-conducting plastic olives (also known as ferrules).
- The interior of the connector is lined with a thin, electrically insulating Kapton® film (thickness either 50 µm or 25 µm depending on what best fits that particular plunger-connector combination).

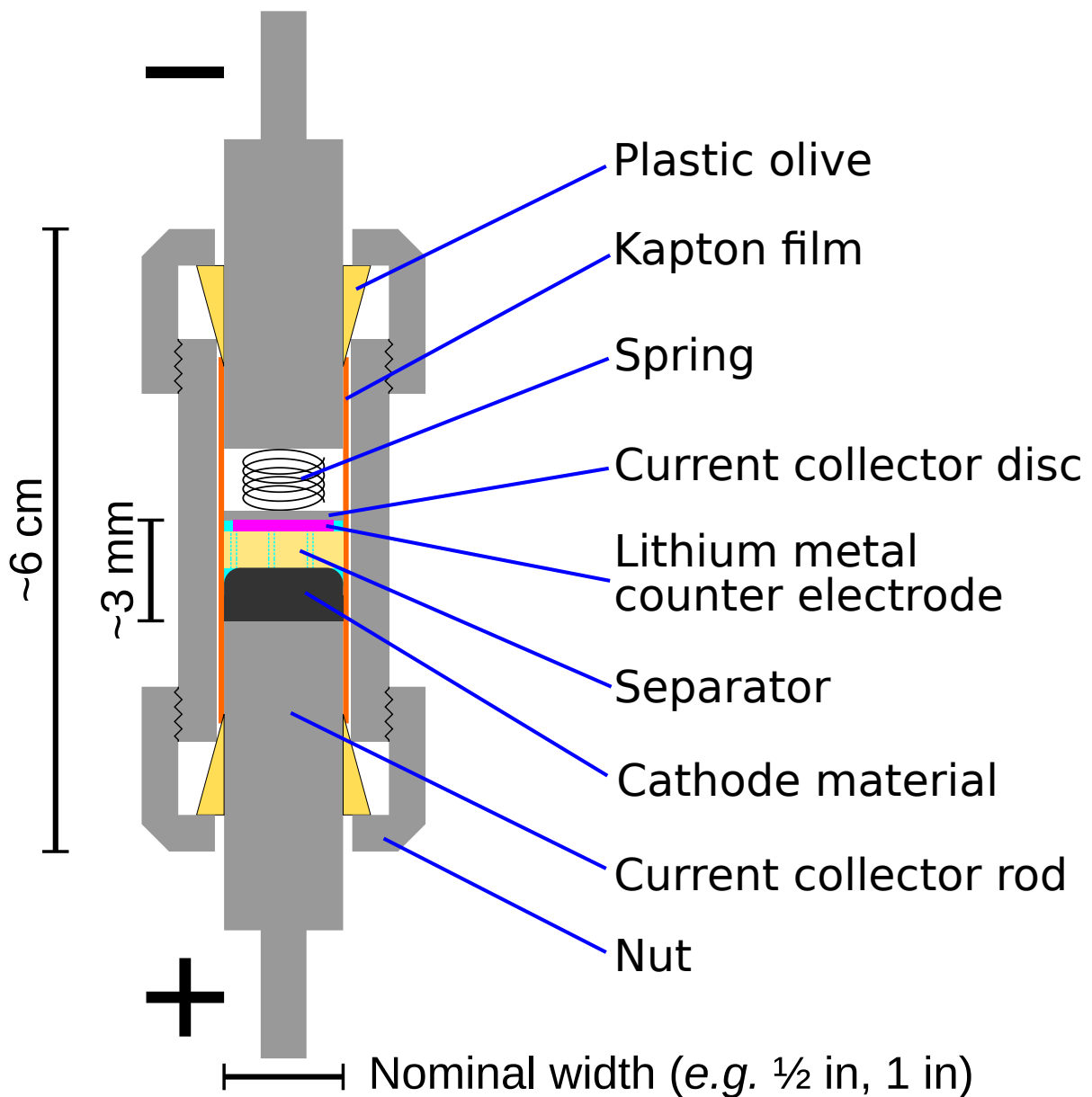


Figure 4.1: Assembled Swagelok cell

One-inch Swagelok cells were assembled as described below, using the 50:50 silicon-carbon mixture as the cathode (200 mg in each cell). (A diagram of a fully assembled cell can be seen in Figure 4.1.) A 1 mol dm⁻³ solution of LiPF₆ in a 1:3 mixture of d4-EC to d6-DMC was used as the electrolyte. ⁷Li metal was used as the anode. As mentioned above, no binder was used.

1. All the metal components are dried at 80 °C in an oven. The Kapton[®] film is dried in a desiccator. *
2. The interior of the connector is lined with a piece of Kapton[®] film, ensuring that the ends overlap by 2 mm to 5 mm. †
3. The shorter of the two plungers is inserted and fastened in place with the nut and insulating plastic olives. This plunger will form the current collector for the cathode.
4. The nut is labelled with the experimenter's initials, the sample identifier and the date of assembly. This also serves the purpose of marking which end of the cell is the cathode so that it can be connected to the battery cycler with the correct polarity.
5. The cell is fixed in an upright position and the silicon/carbon mixture is poured in.
6. A disc of glass fibre filter (Whatman) cut to fit the internal diameter of the cell is then placed on top of the cathode material, taking care not to disturb the powder. ‡
7. The partially assembled cell is transferred into the glove box. §
8. Electrolyte solution is pipetted onto the separator.
9. A disc of lithium ribbon, cut to be slightly smaller than the internal diameter of the cell, is placed on top of the separator. If using large quantities of cathode material, two discs may be needed. ⁷Li-enriched lithium was supplied as a solid block rather than ribbon, so it was first pressed to flatten it to an appropriate thickness.
10. The stainless steel current collector disc and the spring are added.
11. The anode rod is inserted and, while pressing on the rod to ensure that the spring is compressed, the plastic olives are added and the nut is tightened to fix the rod in place.

*The plastic components become brittle if kept at a high temperature for too long

†Too little overlap and there is a risk of a short circuit, too much and the plungers do not fit easily

‡If the disc does not fall into place easily, the metal rod that will subsequently form the current collector for the anode is used to push it gently into place.

§If the cathode material is air sensitive, the cell is transferred into the glove box before adding the cathode.

12. The cell is removed from the glove box and the nuts are tightened again to ensure a good seal.

4.1.3 Electrochemical cycling

The cells were discharged galvanostatically on an Arbin Instruments battery cycler at C/200 (approximately 1.8 mA) until a voltage limit was reached, and then held at that voltage for at least 100 h. Before and after the discharge steps the cells were ‘rested’ to measure the open circuit voltage (OCV). During cycling, the cells were stood cathode-end down in a stand made from a disposable plastic drinking cup to prevent electrolyte pooling at one side. Different voltage limits were used for different cells, to sample the structure at different stages in the cycling process (see Figure 1.3 and subsection 1.2.2 for a description of these different stages). A voltage limit of 500 mV was used to sample the SEI structure while leaving the silicon unreacted. A voltage limit of 75 mV was used to sample the amorphous, partially lithiated phase before crystallisation of $\text{Li}_{15}\text{Si}_4$. A voltage limit of 0 mV was used to sample the fully lithiated material. Several cells were cycled on each schedule, and only the best-performing (closest to the theoretical capacity) were used in the samples for neutron scattering.

4.1.4 Extraction of active material

The cells were disassembled in an argon glove box and the lithiated cathode material was removed and packed into sealed vials for transport to the neutron source. To avoid contamination with ^1H , no solvent wash was used. Because the amount of material from a single cell was not large enough to fill a sample container, the cathodes from two cells produced and cycled under the same conditions were combined to make a single sample for the neutron diffraction experiments.

4.1.5 Neutron scattering experiments

Neutron total scattering patterns were obtained on the GEM instrument at the ISIS neutron source, Rutherford Appleton Lab, UK.

The samples were transferred into vanadium cans for acquisition of the scattering patterns. For the battery samples, all handling was done inside an argon glove box, and an indium gasket was used to ensure an airtight seal on the lid of the can. Because a single Swagelok cell did not hold enough material to fill a can, the material extracted from the two best-performing cells at each voltage point (‘D10’ and ‘D11’ for 500 mV, ‘D01’ and ‘D03’ for 75 mV, and ‘D06’ and ‘D08’ for 0 mV) was combined into one sample. For the unreacted electrode material, packing was done on the open bench. Because this

material was not limited in quantity, a larger can (8 mm as opposed to 6 mm for the battery samples) was used

The vanadium cans holding the samples were mounted on a sample changer, together with empty cans so that the scattering from the container could be measured and subtracted. 8 hours each of data (in one hour slices) were acquired for each of the samples, for the empty cans, and a background count with neither sample nor can. The data for intensity normalisation (vanadium rod and empty chamber counts) were supplied by the instrument scientists, having been acquired two weeks earlier.

Preliminary analysis of each sample’s first hour’s data with `Mantid` [105] showed that the quality of the data from the 75 mV sample was unacceptably bad, so no further data were acquired from that sample and it was not included in the subsequent analysis.

4.1.6 Preliminary data processing

Each sample’s raw scattering data was normalised and corrected with `Gudrun` to give differential cross-section as a function of Q for each of the detector banks separately (for use as an input for `ProfFitS`), together with a merged $S(Q)$. `ProfFitS` (see chapter 3) was then used to obtain the $D(r)$ PDFs. `GSAS` was used to fit the crystalline silicon Bragg peaks.

`Gudrun` requires the composition of the sample to be supplied in the input file. The relative amounts of silicon and conductive ‘Super P’ carbon in the starting material were known, and the amount of lithium could be calculated from the electrochemistry data, but the amount of SEI was unknown. However, the relative areas of the first and second peaks in the $D(r)$ (at approximately 1.1 Å and 1.4 Å respectively) can be used to calculate the ratio of C–D bonds to C–C and C–O bonds in the sample. Assuming that the ratios in the SEI are the same as in DMC and that each carbon atom in the carbon Super P has three bonds to other carbon atoms (as in graphite), this can be used to calculate the ratio of SEI to conductive carbon and thus the overall composition. This new composition was then fed back into `Gudrun` and the process iterated until a self-consistent composition was obtained.

4.1.7 RMC calculations

`RMCprofile` was used to fit the structures of the various electrode components against the experimental $D(r)$ and $Qi(Q)$ data. When fitting the structures of the silicon and carbon in the starting material, the Bragg peaks (the ‘profile’ of `RMCprofile`) were also used. The $Qi(Q)$ data was obtained from the `Gudrun` ‘merged $S(Q)$ ’ output with `convertdata.py`, the ‘Bragg’ data was converted from the `GSAS` output using `rmccreate`, and the $D(r)$ data was generated using `ProfFitS` as mentioned above.

Since there is no way to refine phase fractions in the current version of `RMCprofile`, certain assumptions had to be made in order to specify the phase fractions of the various components. The SEI phase fraction was obtained from the peak ratios in the $D(r)$ as detailed in subsection 4.1.6. The silicon phase fraction in the 500 mV sample was obtained by assuming that none of the silicon had reacted, while in the 0 mV sample it was assumed that all the current passed through the cell had gone into forming $\text{Li}_{15}\text{Si}_4$ while the remaining silicon remained in its initial state. This assumption is supported by the continued presence of silicon Bragg peaks in the ‘fully discharged’ sample (see Figure 4.6). Also, since there is no way (in the current version) to fit structures against several experimental data sets with different weightings, the fit had to be done sequentially: first fitting the structures of the starting material, then holding those structures fixed while fitting the SEI structure against the 500 mV (starting material plus SEI) data, and finally holding the structures of the carbon Super P, SEI and unreacted silicon fixed while fitting against the data from the fully discharged sample.

First the scattering from the starting material (including the silicon Bragg peaks) was fitted with two configurations — one of silicon and one of carbon. The initial configuration for the silicon configuration was crystalline silicon ($10 \times 10 \times 10$ unit cells, 8000 atoms, 160 nm^3), while the carbon configuration was initialised as graphite ($21 \times 21 \times 8$ unit cells, 14112 atoms, 127 nm^3).

After running the first fit for 30 million iterations, the resulting configurations were used, together with a new configuration representing the SEI, to fit the scattering obtained from the 500 mV sample. The silicon and carbon configurations were held fixed — only the SEI configuration was allowed to vary. The initial configuration for the SEI was DMC molecules arranged on a lattice with the same density as liquid DMC (11664 atoms, 136 nm^3). The fit for the SEI was run for 20 million iterations.

Finally, the data from the 0 mV sample was fitted. The configurations for the carbon, the SEI and the unreacted crystalline silicon were taken from the results of fitting the other data sets and were not allowed to vary further. The initial configuration for the lithium silicide was crystalline $\text{Li}_{15}\text{Si}_4$ with the unit cell axes expanded by 3% in an attempt to stop the partial PDFs bunching up against the minima imposed by the `MINIMUM_DISTANCES` constraints ($4 \times 4 \times 4$ unit cells, 4864 atoms, 86 nm^3). The fit was run for 30 million iterations.

4.2 Results

4.2.1 Electrochemical performance

The ‘fully discharged’ samples were both held at 0 mV for over 200 h after discharging at a C/200 current, but nevertheless the two best-performing samples only reached 2532 mA h g^{-1} and 2672 mA h g^{-1} , compared to the theoretical capacity of 3579 mA h g^{-1} . However, given the lack of binder it is hoped that this results from some of the crystalline silicon remaining unreacted due to lack of electrical percolation rather than from any partial reaction. The fact that the neutron diffraction pattern of the fully discharged samples still contains obvious Bragg peaks from crystalline silicon supports this hypothesis (see subsection 4.2.2).

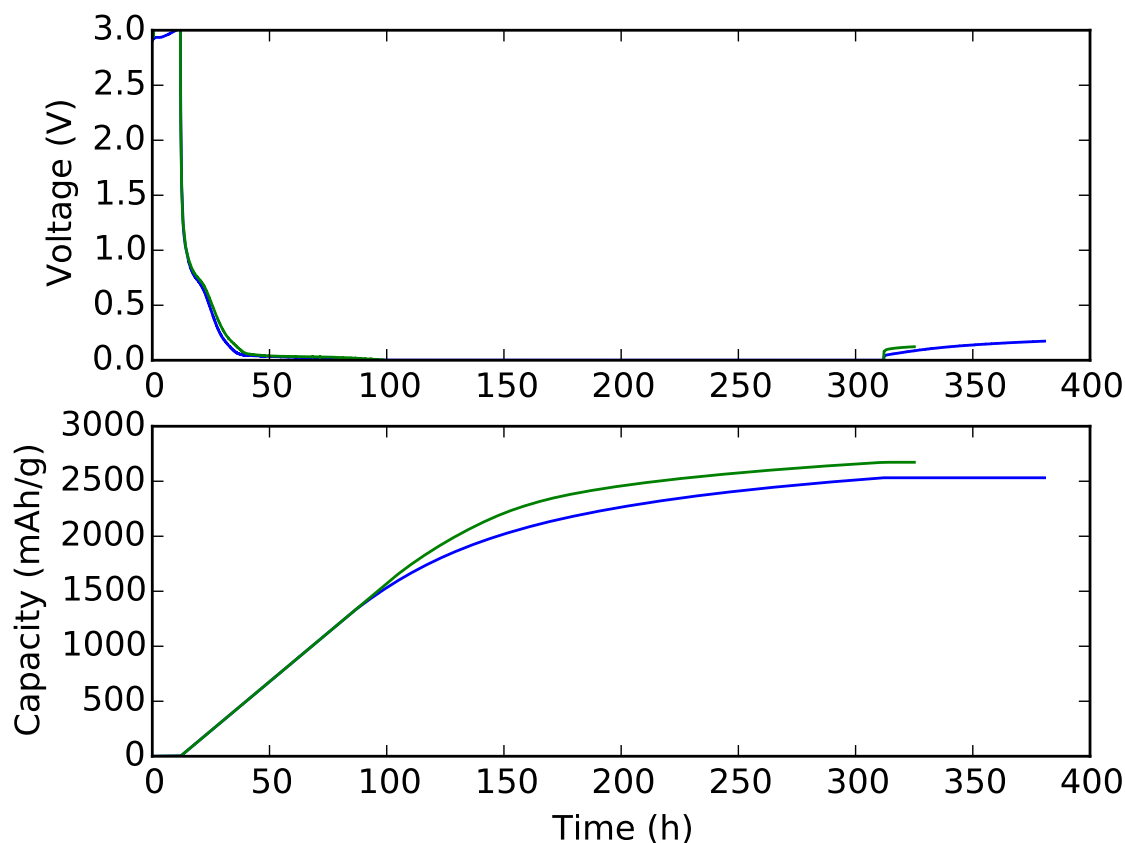


Figure 4.2: “Fully discharged” samples — ‘D06’ (blue) and ‘D08’ (green). The top graph shows the cell voltage, while the bottom graph shows the charge that had passed across the cell, normalised against the mass of silicon in the electrode. The initial 12 h and the period after 312 h are open-circuit ‘rest’, with the voltage being recorded but no current flowing. Between ~ 100 h and 312 h the voltage is being held at 0 (short circuit) which causes the voltage curve to overlap with the time axis.

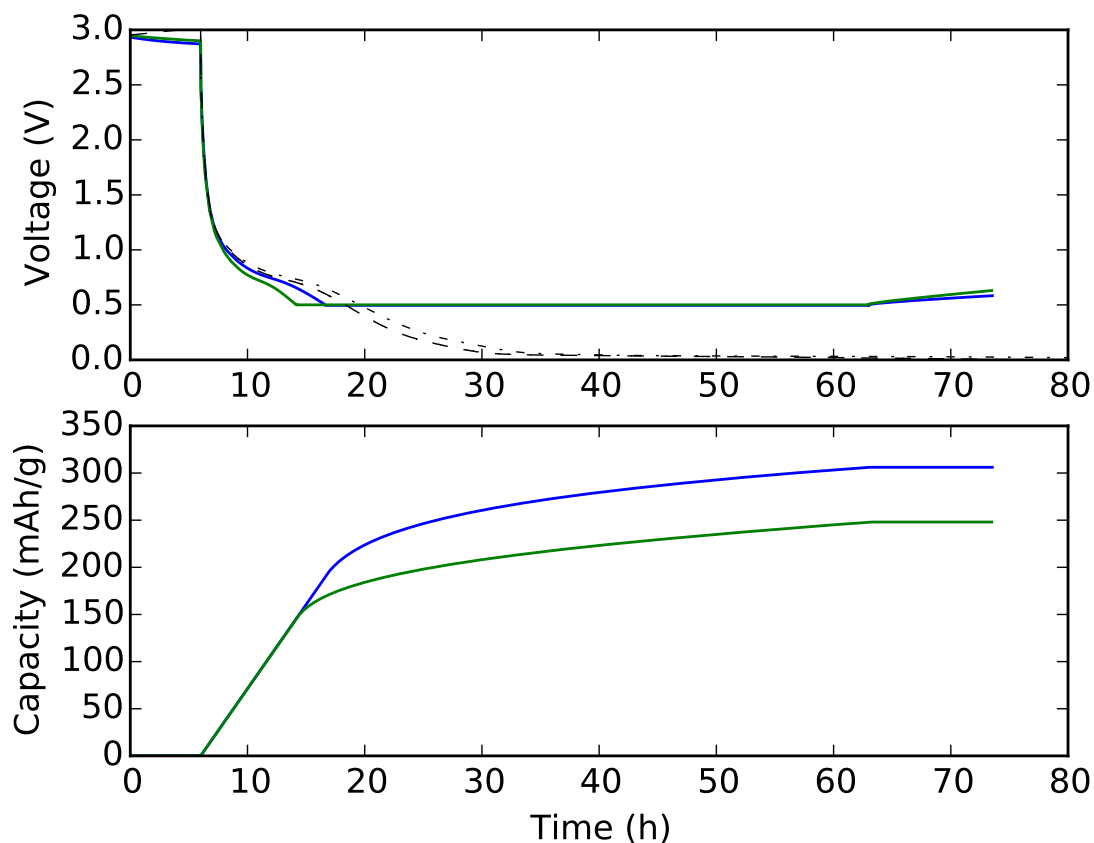


Figure 4.3: “SEI only” samples — ‘D10’ (blue) and ‘D11’ (green). The top graph shows the cell voltage, while the bottom graph shows the charge that had passed across the cell, normalised against the mass of silicon in the electrode. The voltage-time profiles of the “fully discharged” samples are shown in faint dashed lines for comparison. The periods before 6 h and after 63 h are open-circuit ‘rest’, with the voltage being recorded but no current flowing. The long flat part of the voltage graph is the voltage being held at 500 mV.

4.2.2 Raw scattering patterns

The scattering patterns output by Gudrun can be seen in Figure 4.4, Figure 4.5 and Figure 4.6. Theoretically, the results from each detector bank (the different coloured lines on each graph) should be identical, but clearly that is not the case. The discrepancy between the different banks is probably due to inelastic scattering, which is relatively stronger (for a given Q) at low detector angles, since a given Q at a lower detector angle means a higher speed and kinetic energy than the same Q at a higher angle. This interpretation is reinforced by the discrepancy being largest in the fully discharged sample (Figure 4.6), which has much more of the light nuclei ${}^7\text{Li}$ and ${}^2\text{H}$ and therefore stronger inelastic scattering.

The silicon Bragg peaks are slightly weaker in the 500 mV sample (Figure 4.5) than in the starting material (Figure 4.4), but this can be explained by the added SEI increasing the ‘number of atoms’ denominator in a graph of barn/steradian/atom). In the scattering pattern from the 0 mV sample (Figure 4.6), weak silicon Bragg peaks are still present, indicating that some unreacted crystalline silicon remains and thus that the failure to reach the theoretical capacity of 3579 mA h g^{-1} is more likely due to some of the silicon remaining unreacted than to the reaction stopping at some intermediate phase.

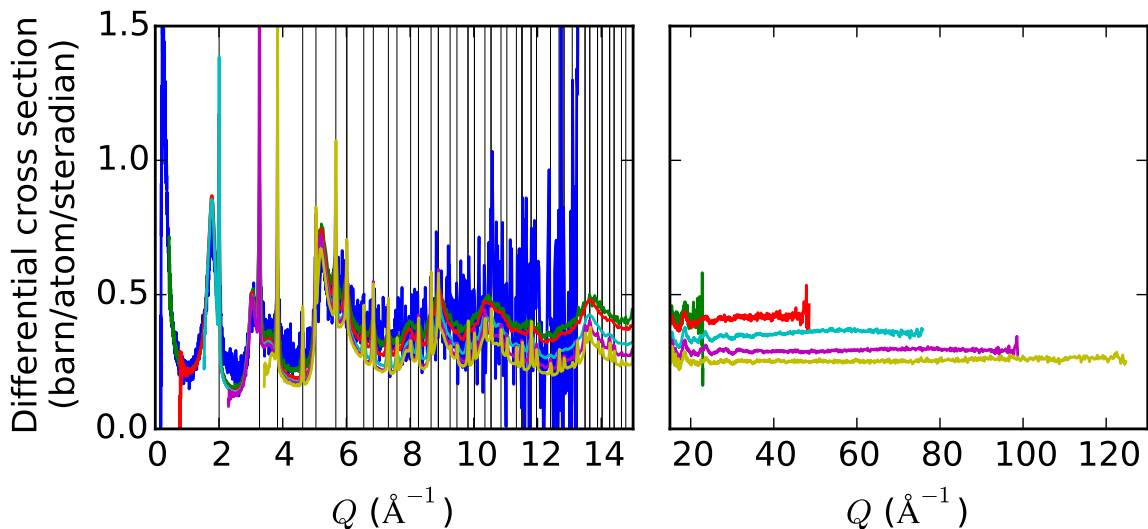


Figure 4.4: Scattering pattern of the silicon-carbon starting material, after processing with Gudrun but before any further changes. The different coloured lines are the patterns obtained by the different detector banks. (Bank 1 is omitted because it covers only the very low Q region.) The vertical black lines mark the locations of the Bragg peaks of crystalline silicon, and are omitted on the right hand graph ($Q > 15$) because they would be too close together and obscure the rest of the graph.

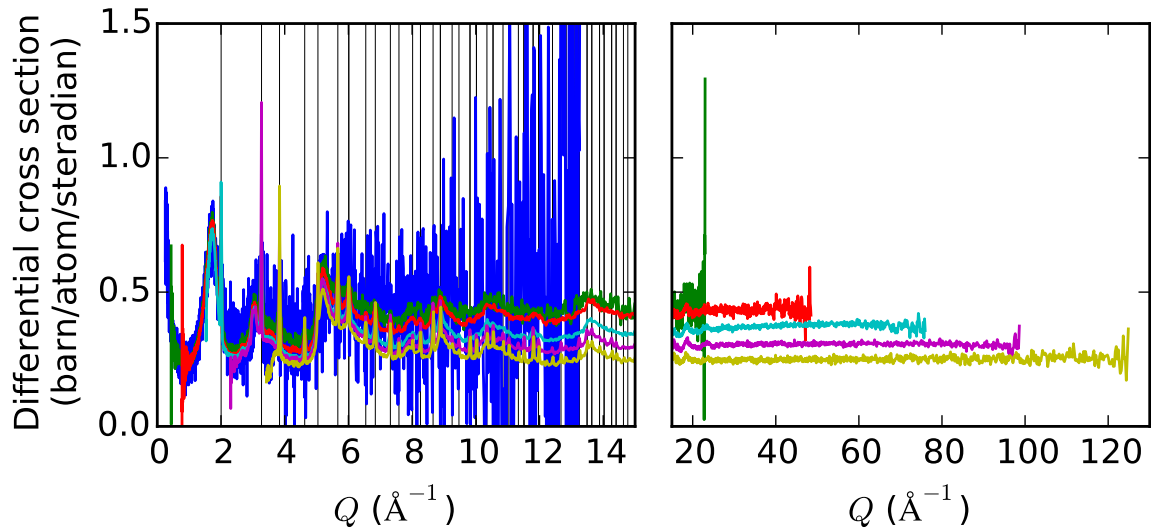


Figure 4.5: Scattering pattern of the “SEI only” sample, after processing with Gudrun but before any further changes. The different coloured lines are the patterns obtained by the different detector banks. (Bank 1 is omitted because it covers only the very low Q region.) The vertical black lines mark the locations of the Bragg peaks of crystalline silicon.

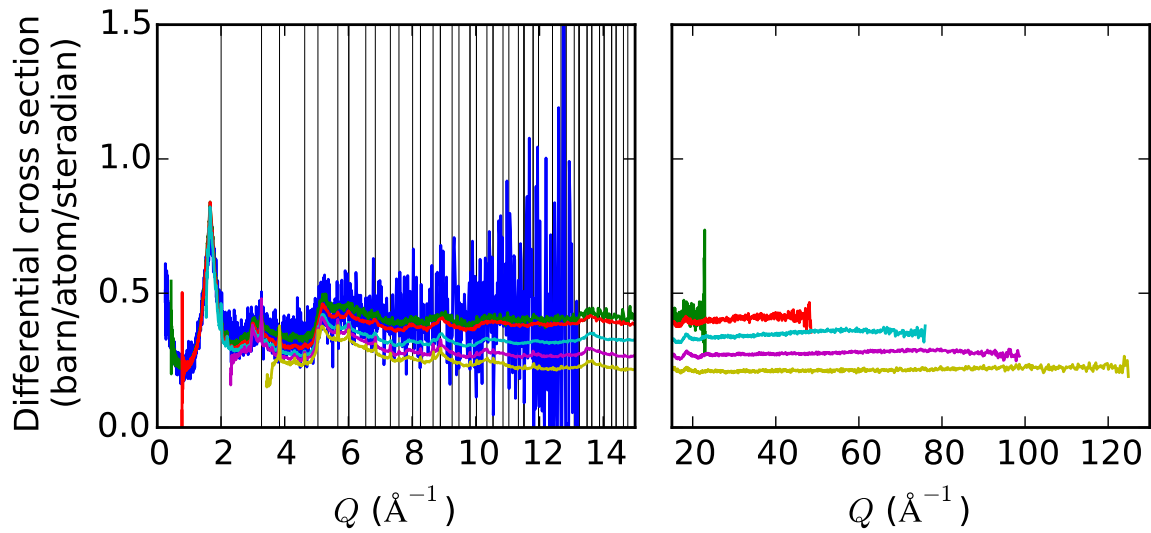


Figure 4.6: Scattering pattern of the “fully discharged” sample, after processing with Gudrun but before any further changes. The different coloured lines are the patterns obtained by the different detector banks. (Bank 1 is omitted because it covers only the very low Q region.) The vertical black lines mark the locations of the Bragg peaks of crystalline silicon.

4.2.3 RMC

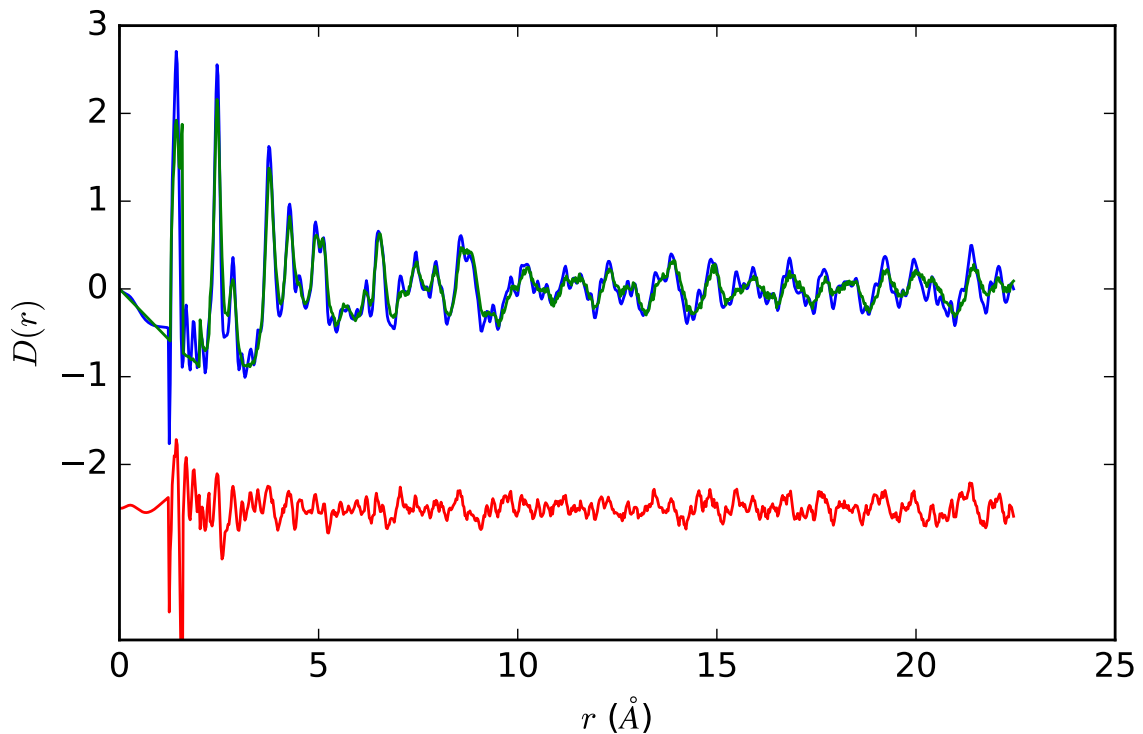


Figure 4.7: $D(r)$ (experimental in blue and calculated in green, difference in red) for the RMC fit of the starting material

The comparison of fitted and experimental $D(r)$ for the intermediate RMC runs can be seen in Figure 4.7 and Figure 4.8. In both cases, the experimental $D(r)$ displays what seems to be ringing artefacts, possibly due to incomplete compensation for the inelastic scattering at high Q during the `ProfFitS` calculations. In Figure 4.7 (the starting material) there is also a marked tendency for the peaks in the fitted curve to be shorter and broader than those in the experimental curve, particularly in the ranges $r < 5$ and $r > 16$. This could be explained by the weighting of the fit to experimental data in the RMC being too weak (*i.e.* too high ‘temperature’), so that the atomic positions are too strongly randomised.

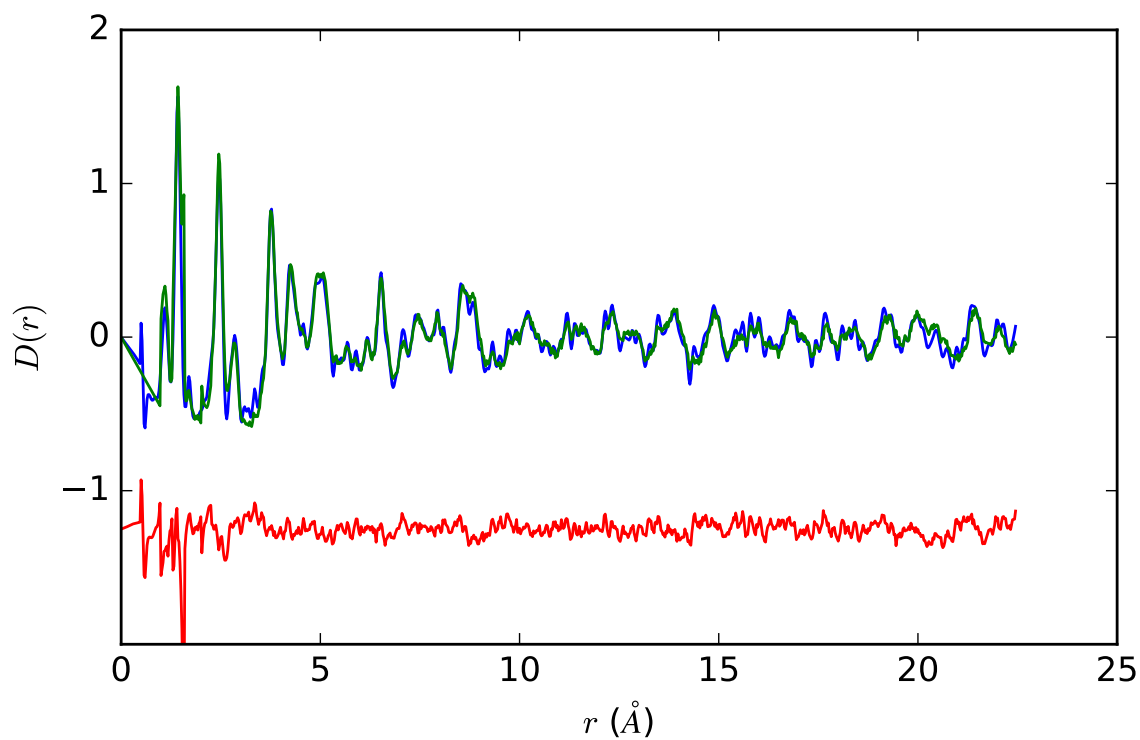


Figure 4.8: $D(r)$ (experimental in blue, calculated in green, difference in red) for the RMC fit of the partially discharged (SEI) sample

The RMC fit of the data from the fully discharged sample was run for 30 million iterations. The χ^2 decreased quickly and then levelled off after around 1 million iterations, as can be seen in Figure 4.9. The lowest value was observed after approximately 6 million iterations.

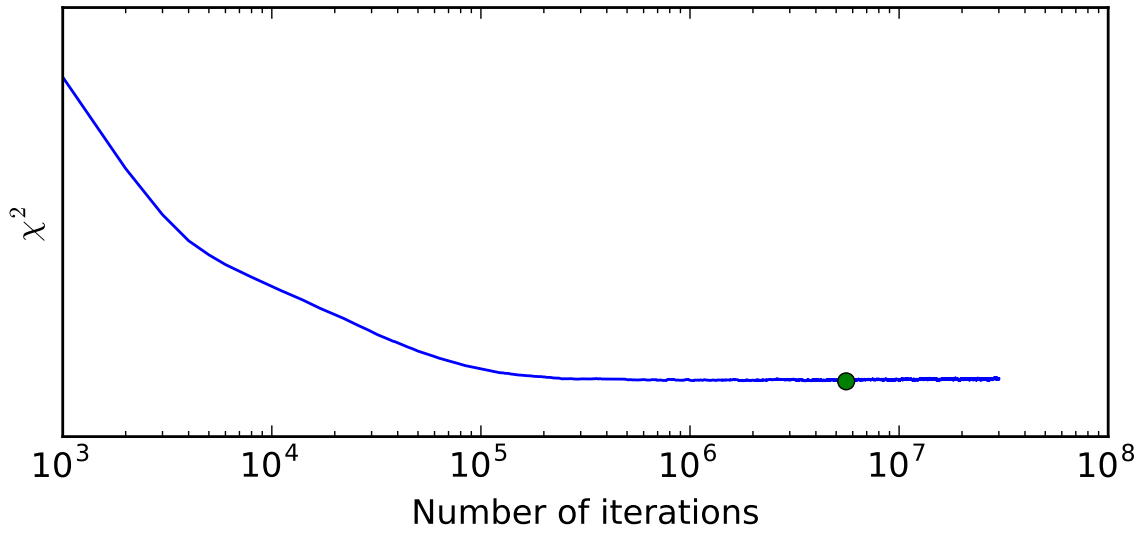


Figure 4.9: Improvement in χ^2 as the RMC fit of the fully discharged sample progresses. The lowest χ^2 is marked with a green dot.

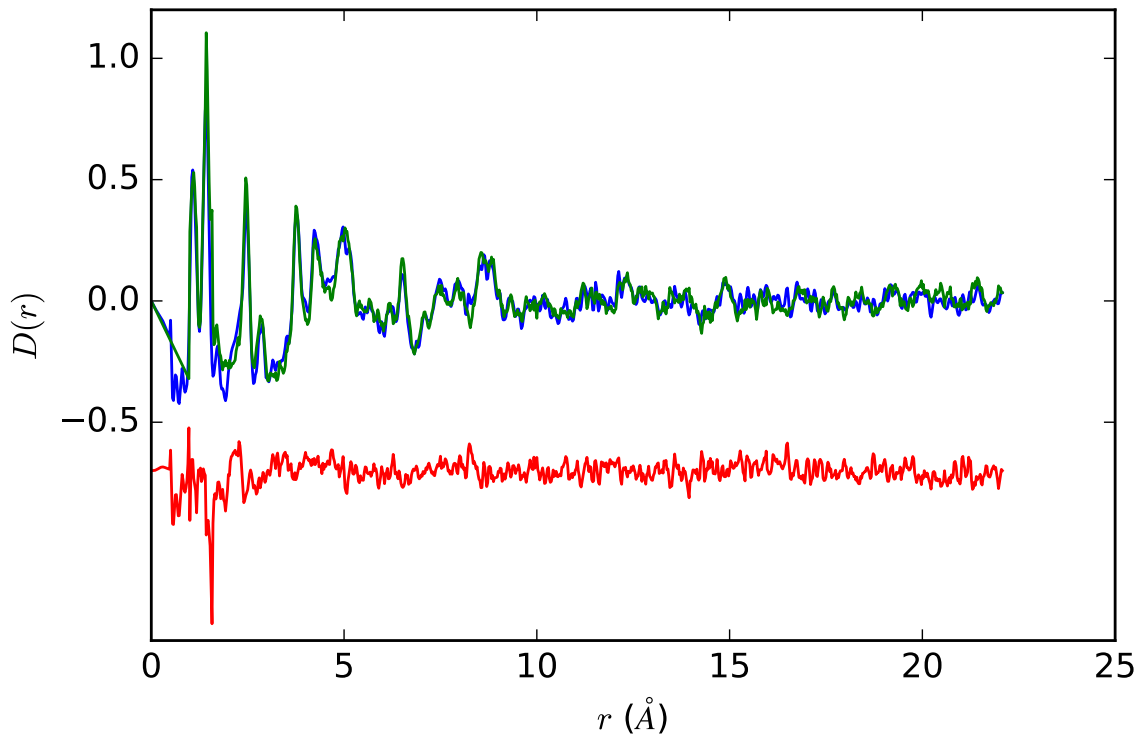


Figure 4.10: $D(r)$ (experimental in blue, calculated in green, difference in red) for the final configuration of the RMC fit of the fully discharged sample

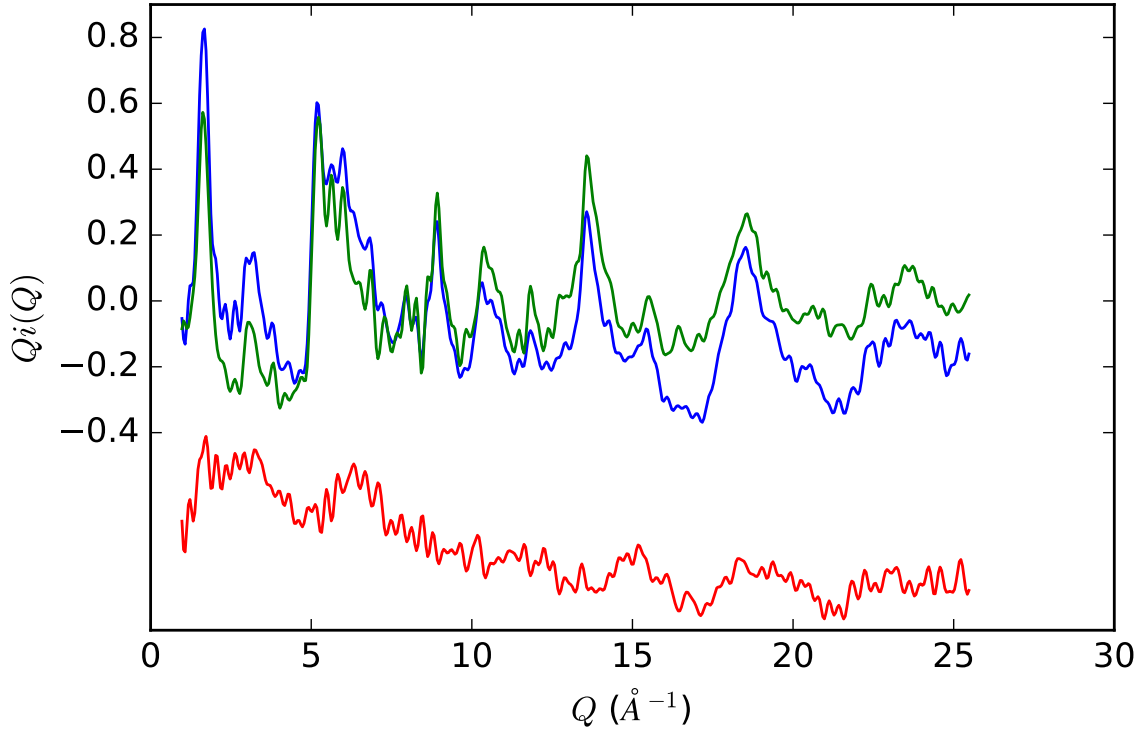


Figure 4.11: $Q_i(Q)$ (experimental in blue, calculated in green, difference in red) for the final configuration of the RMC fit of the fully discharged sample

The $D(r)$ and $Q_i(Q)$ of the final fitted calculation can be seen in Figure 4.10 and Figure 4.11 respectively. The $D(r)$ graph again shows signs of ringing artefacts in the experimental curve, particularly in low r region before the C–H peak at 1.1 Å but, unlike in Figure 4.7, any broadening of peaks in the calculated curve relative to the experimental one seems confined to high r values and the 1.4 Å C–C and 2.4 Å peaks.

The partial $G'(r)$ curves calculated for the $\text{Li}_{15}\text{Si}_4$ configuration after 30 million iterations are shown in Figure 4.12. The sharp dropoffs, particularly evident in the Li–Si curve, are due to the `MINIMUM_DISTANCES` constraints. This is despite the minimum distances being set well below the shortest distances found between those atoms in known lithium silicide crystal structures. This indicates that the ‘force’ on the atoms from trying to fit the experimental data is either not strong enough to prevent randomisation of the positions or possibly even acting in the wrong direction because of overcompensation for the confounding effects of the other materials in the heterogeneous mixture. This ‘wrong direction’ hypothesis is contradicted, however, by the fact that in the region 2.0 Å to 2.3 Å, where the Li–Si partial has a strong peak, the calculated $D(r)$ is actually lower than the experimental value. (Note that because of ${}^7\text{Li}$ ’s negative scattering length, the Li–Si peak will have a negative contribution to $D(r)$.)

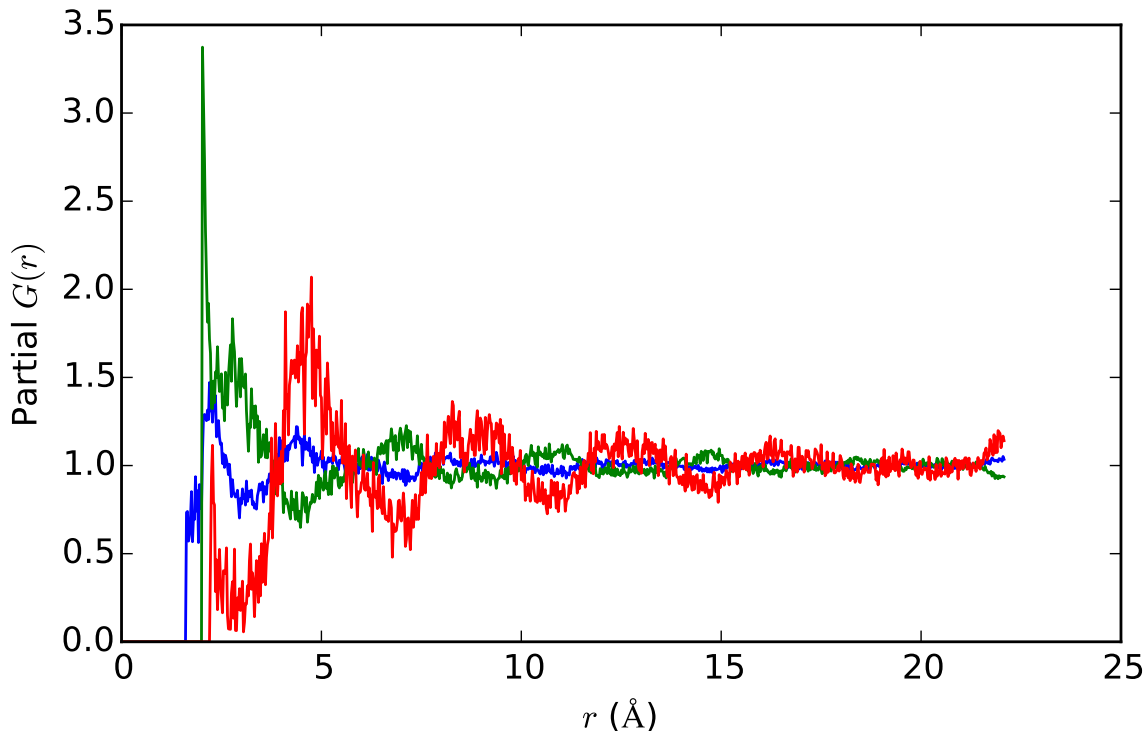


Figure 4.12: Partial $G'(r)$ (Li–Li in blue, Li–Si in green and Si–Si in red) for the final $\text{Li}_{15}\text{Si}_4$ configuration of the RMC fit of the fully discharged sample

4.3 Discussion

The validation work described in section 2.9 showed that RMC modelling of mixtures is possible in principle, but also that correct results are not a foregone conclusion even when the sample composition is known exactly and the experimental data are free from errors. Unfortunately, the practicalities of electrochemical cycling of silicon make it very difficult to determine the composition of the highly heterogeneous mixture collected from the cell cathode. In particular, cells containing the quantities of silicon needed to produce samples large enough for neutron diffraction work have worse electrochemical performance, leading to the presence of unreacted or incompletely reacted silicon in the obtained sample. Additionally, both the precise chemical makeup of the solid-electrolyte interphase and the quantity of SEI present are not feasible to measure. The presence of hydrogen or even, to a lesser extent, deuterium in the SEI leads to further difficulties, as inelastic scattering adds a systematic error to the experimental data used as input by the RMC algorithm. Had the implications of these problems been fully understood before commencing the present work, it is likely that the research would have taken a different path.

One additional confounding factor in the interpretation is that several of the key peaks present in the $D(r)$ patterns for the individual phases overlap with each other.

Most obviously, both the SEI and the conductive carbon filler have C–C bonds (and C–O in the SEI) at approximately 1.4 Å. Additionally, the second-nearest-neighbour C–C–C peak in the conductive carbon and the Si–Si bond distance in crystalline silicon both appear at approximately 2.4 Å, while the third-nearest neighbour in graphite at 2.8 Å is close to the Li–Li and Li–Si distances of approximately 2.7 Å in $\text{Li}_{15}\text{Si}_4$. All this makes qualitative interpretation of the results difficult, and will decrease the stability of a quantitative analysis. The decrease in the height of the 2.4 Å peak, and in the peaks in the high r range where ordered crystalline silicon will be the main contributor to the $D(r)$ function, from the starting material (Figure 4.7) to the lithiated product (Figure 4.10) shows that the silicon is being consumed during the reaction, as expected, but the continued presence of silicon $D(r)$ peaks in the final product also shows that some unreacted crystalline silicon remains. Likewise, the growth of the C–H (or rather C–D) peak at 1.1 Å is demonstrative of the presence of organic electrolyte material.

The original aim of the research presented in this chapter was to obtain structural insight into the chemical processes occurring during electrochemical lithiation and delithiation of silicon. This requires a reconstruction of the lithium silicide structures present at various stages of lithiation and delithiation which, if not perfectly accurate, at least preserves the relevant structural features. The most simple of these is the presence and nature of Si–Si bonded Zintl clusters or networks, which other work (*e.g.* Ogata et al. [60]) has suggested act as nucleation centres for the formation of other phases, decreasing the overpotential and thus increasing the efficiency of the cell and improving its high-power performance. A glance at Figure 4.12 shows that the Li–Si distances, and to a lesser extent the other partial $G'(r)$ distributions, are highly unphysical, with sharp drop-offs due to the `MINIMUM_DISTANCES` constraints. Since an accurate reconstruction of the pair distance distribution is a necessary condition for an accurate RMC model, this is clearly not helpful. While it might be possible, with enough tweaking of the various fitting parameters, to obtain a less obviously incorrect distribution, there would be no guarantee that the structure is in fact correct, given the numerous potential errors and uncertainties introduced by the experimental process.

For RMC analysis of electrochemically produced lithium silicides to give useful results in future, there will have to be less uncertainty about the experimental data and the other components present. A good start would be to avoid the systematic errors in the experimental data introduced by inelastic scattering (*e.g.* by using a different electrolyte or by some process which removes the SEI), or at least to have additional data where these errors are not present (*e.g.* X-ray scattering). Ideally, it would be possible to extract the pure lithium silicides from the heterogeneous electrode mixture and analyse them alone. Failing this, much more detailed information on the other components will be needed, so that they can be properly accounted for in the analysis. This could range

from the elemental composition (measured with *e.g.* inductively coupled plasma mass spectrometry (ICP-MS)) to complementary information on local order from NMR or EXAFS. This analysis would then have to be repeated for electrodes at several different stages of lithiation and delithiation, and compared with reference samples of lithium silicides synthesised via other routes (*e.g.* mechanochemistry), to show if and how the electrochemical reaction process gives unique chemical and structural results.

Chapter 5

In situ NMR experiments on SiNWs

As mentioned in subsection 1.2.6, SiNWs make an excellent model system for investigating the electrochemical reactions of silicon with lithium. In particular, unlike silicon powder, they do not need pressure to be applied in order to retain electrical connectivity during delithiation, thus avoiding the problems experienced by Key et al. [122] in their *in situ* NMR experiments with silicon powder electrodes.

5.1 Methods

SiNWs were synthesised on a carbon fibre (CF) substrate by Ken Ogata using the procedure described in appendix A.1.1. The reasons for this choice of substrate are explained in subsection 5.1.1. Plastic bag cells were assembled according to the procedure described in subsection 5.1.2. Note that, while silicon would be used as an anode material in a cell optimised for energy storage, it acts as a cathode when cycled against lithium metal.

5.1.1 Preliminary tests of substrate suitability

Four materials suggested by Ken Ogata as possible substrates for SiNW growth were evaluated for their compatibility with *in situ* NMR, in particular whether the magnetic susceptibility of the substrate would lead to distortions in the NMR spectrum. The possible substrates being evaluated were two different grades of stainless steel foil (SUS304 and SUS316), one type of stainless steel (SS) mesh (SUS304 grade), and a carbon-fibre-based gas diffusion layer (CFGDL) mat. Each sample was sealed into a plastic bag, of the same type as used for the bag cells for *in situ* NMR, together with a small quantity of the LiPF_6 -based electrolyte solution. (See subsection 5.1.2 for details of materials used.) NMR spectra of these partial bag cells were then acquired using substantially the same parameters as the eventual *in situ* NMR experiments. (See subsection 5.1.3 for details.)

Figure 5.1 shows that the CFGDL substrate gives moderate distortion of the spectrum,

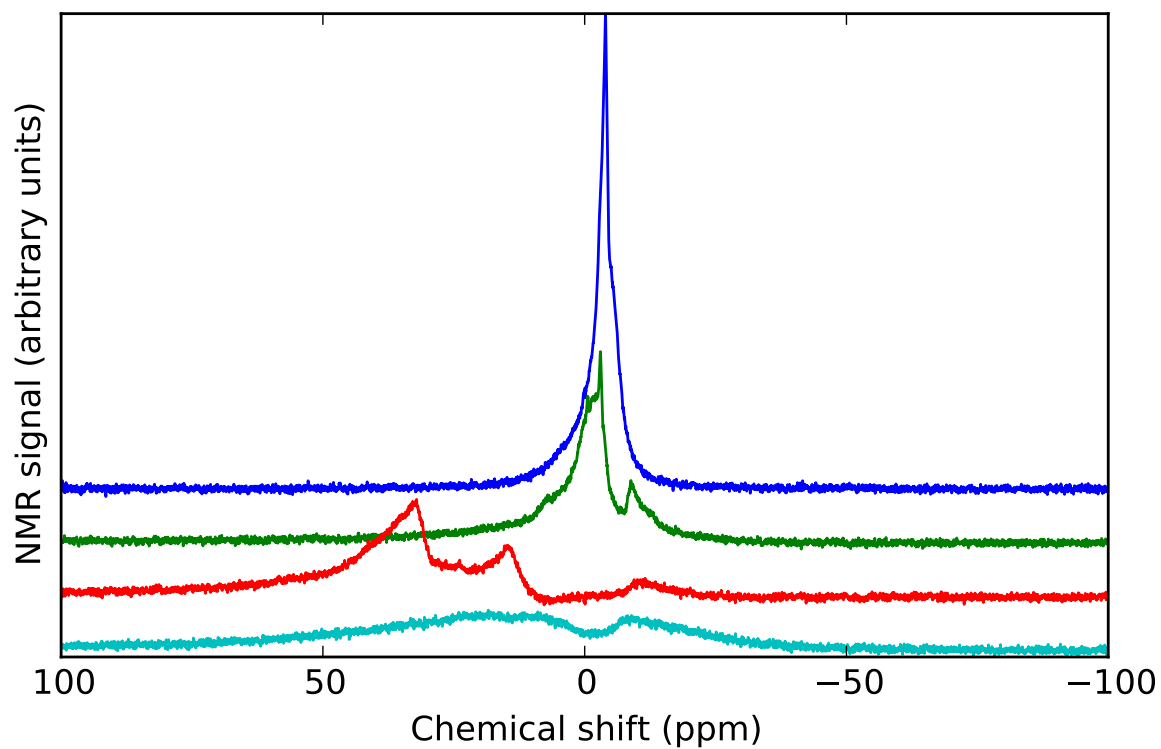


Figure 5.1: NMR spectra of the LiPF_6 -based electrolyte in the presence of different proposed SiNW-growth substrates: carbon fibre (blue), SUS316 foil (green), SUS304 foil (red), SUS304 mesh (cyan). Ideally the spectrum should be a single sharp Lorentzian peak.

while all the SS substrates (even the supposedly ‘non-magnetic’ SUS316 steel) severely distorted the spectrum of the nearby electrolyte. For the purposes of electrochemistry, SS substrates would be preferable, as they do not react electrochemically with lithium while CF does, but the distortion to the NMR spectra from the SS substrates was unacceptably high and therefore CF is preferred overall.

5.1.2 Assembly of bag cells

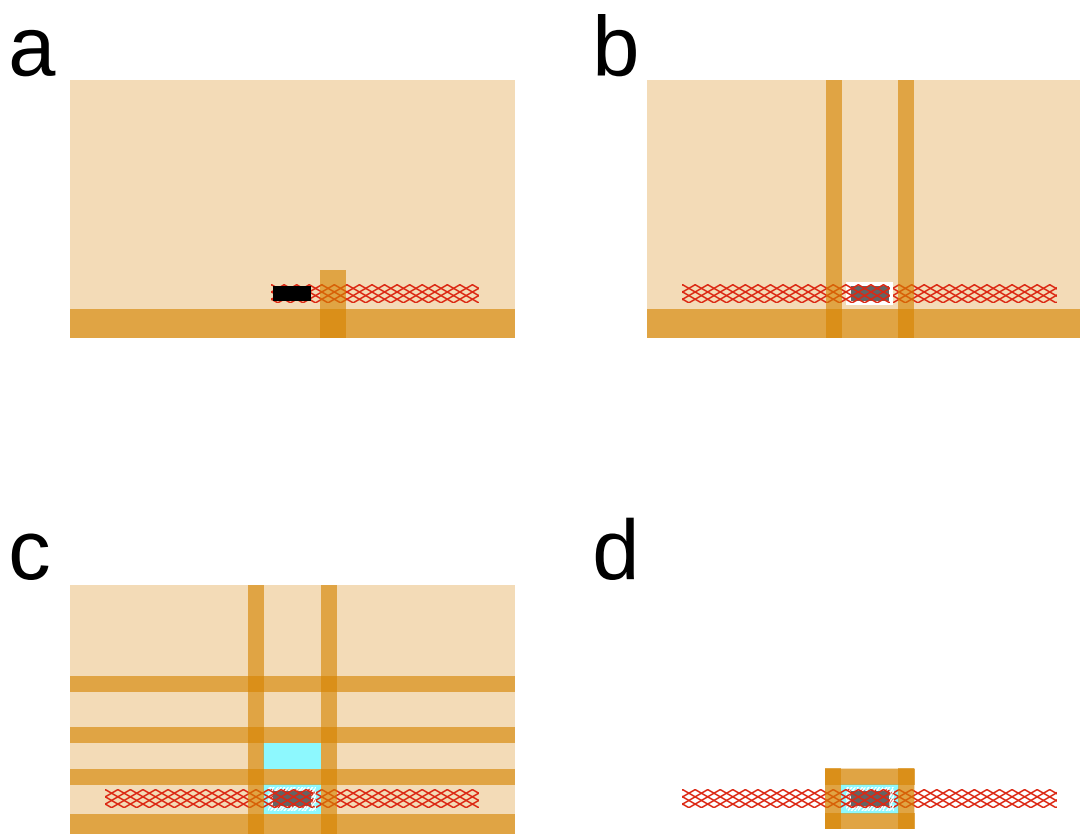


Figure 5.2: Various steps in the fabrication of a bag cell. (a) The cathode and its current collector are fixed in place before transferring into the glove box. (b) The separator, the lithium metal counter electrode and its current collector are added and heat seals are made all the way up the bag. (c) The electrolyte is added and sealed in. (d) After removing the cell from the glove box, the extra plastic is trimmed off, exposing the current collectors.

1. A sheet of copper mesh about 10 cm wide is impregnated with hot melt glue in a band about 1 cm wide and about 2 cm from one side.
2. The sheet is cut crosswise into strips approximately 4 mm wide.
3. The cathode is cut into pieces approximately 8 mm by 4 mm in size

4. The short end of one of these strips of copper is folded over the cathode so as to hold it in place.
5. A piece of polyester bag (3M Scotchpak[®]) is cut — at least 10 cm wide and at least 20 cm long, with the fold down the long edge.
6. The copper strip and cathode is placed in the centre of the fold of the piece of plastic bag.
7. A hand held bag sealer is used to fix the copper strip in place, with the fixing point being in the region of the copper that is impregnated with the hot melt glue. The cell now looks like Figure 5.2a.
8. The partially assembled bag cell is transferred into the glove box.
9. A piece of glass fibre separator approximately 10 mm by 5 mm in size is placed in the fold of the bag so as to completely cover one side of the cathode.
10. A section of lithium foil approximately 8 mm by 4 mm in size is attached to a strip of copper mesh in the same manner as described above for the cathode material.
11. The strip of copper mesh with lithium foil is placed in the bag so that the lithium foil is in contact with the separator on the opposite side from the cathode, and the current collector strip leads off in the opposite direction to that from the cathode.
12. The anode current collector strip is sealed in place in the same manner as the anode strip was. The cell now looks like Figure 5.2b.
13. Electrolyte solution is pipetted into the partially sealed bag from the side.
14. Taking care to expel all gas bubbles, the remaining unsealed side of the bag is sealed using the bag sealer. Initial sealing is done relatively far from the centre of the cell.
15. Additional seals are made, progressively further in from the initial seal, until the cell is sealed as close in as possible. The cell now looks like Figure 5.2c.
16. The cell is transferred out of the glove box, taking care not to short out the current collectors on the metal base of the glove box or on the transfer tray. (This should not be a problem as the bag should be large enough that the leads are entirely inside the bag.)
17. The extra plastic is trimmed so that the copper strips protrude out of the end of the cell. The cell now looks like Figure 5.2d.

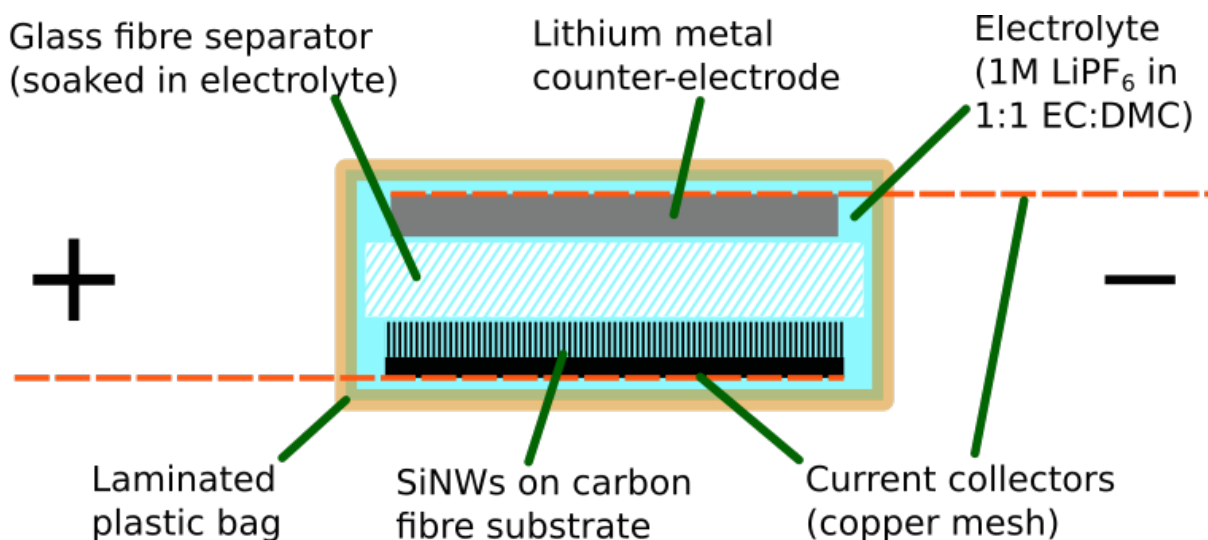


Figure 5.3: Cross section of an assembled bag cell (not to scale)

5.1.3 In situ NMR

The *in situ* NMR experiments were carried out in collaboration with Ken Ogata and occasionally also Elodie Salager; inserting the NMR probe into the magnet without disturbing the electrical connection to the battery cycler absolutely required two people, while many of the other steps were much easier and more convenient with two.

An Oxford Instruments 7.0 T (300 MHz proton frequency) magnet was used with a TecMag LapNMR spectrometer. The probe was a ChemMagnetics static probe with a hand-wound coil. To ensure consistency of bulk magnetic susceptibility effects (see Key [137]) the bag cell was sited horizontally in the coil and fixed in place with tape.

Electrochemical cycling was carried out using a Bio-Logic VMP battery cycler connected to the cell via a coaxial cable fed down from the top of the magnet bore. A 50 MHz low-pass filter was used inline with the cycler to prevent interference between the cycler and the NMR signal. Additional shielding from electrical interference was provided by wrapping the cable in aluminium foil.

The battery cycler and NMR spectrometer were controlled from separate computers on opposite sides of the room. Typically, the NMR data acquisition was started 10 s after the battery cycler, and an extra 10 s of open-circuit ‘rest’ was included at the beginning of the cycling schedule. This allowed a single experimenter to operate both the cycler and the spectrometer if necessary, although as mentioned above there were normally two present. In any case, both the NMR and electrochemistry data files include timestamps (see subsection C.2.3 and section C.3) so the internal time scales can be reconciled.

The recycle delay between pulses was 0.5 s, and 1200 pulses were summed to give each spectrum resulting in one spectrum acquired every 10 min.

5.2 Results

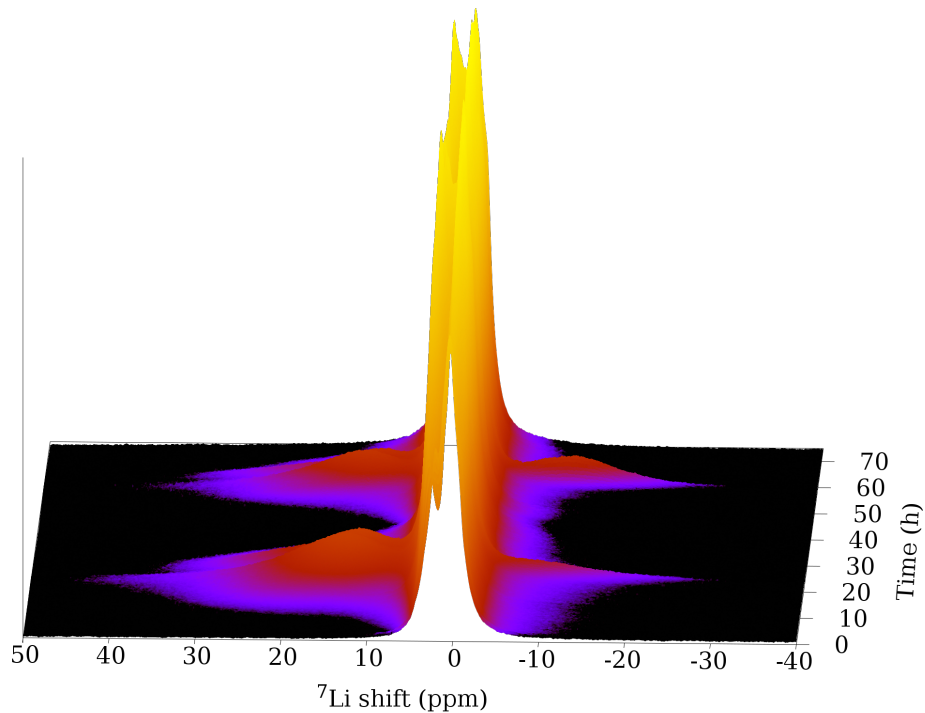


Figure 5.4: 3D surface plot of the *in situ* NMR spectra as they vary over time. The large central peak comes from the electrolyte and SEI. The small peaks to the side are lithium silicides. The peaks from the lithium metal (both bulk and dendrites) are off the scale to the left.

5.2.1 PCA analysis

Principal component analysis is much simpler than NMF, so the *in situ* NMR data was first processed using PCA as a preliminary investigation. The spectra of each component can be seen in Figure 5.6 and the changes in the weighting of each component over time can be seen in Figure 5.5.

The third principal component (red) varies strongly at the top of the charge (*i.e.* full delithiation, high voltages *vs* $\text{Li}|\text{Li}^+$). This is intriguing, because most previous work (*e.g.* Ogata et al. [60], Key et al. [122]) has focused on the highly lithiated states with the aim of selecting cutoff voltages which avoid the formation of stable crystalline lithiated phases and thus reduce hysteresis and increase cycle life.

By contrast, relatively few authors have considered the role of the cutoff voltage for delithiation. A 2011 review by Zhang [163] mentions the lower cutoff voltage several times

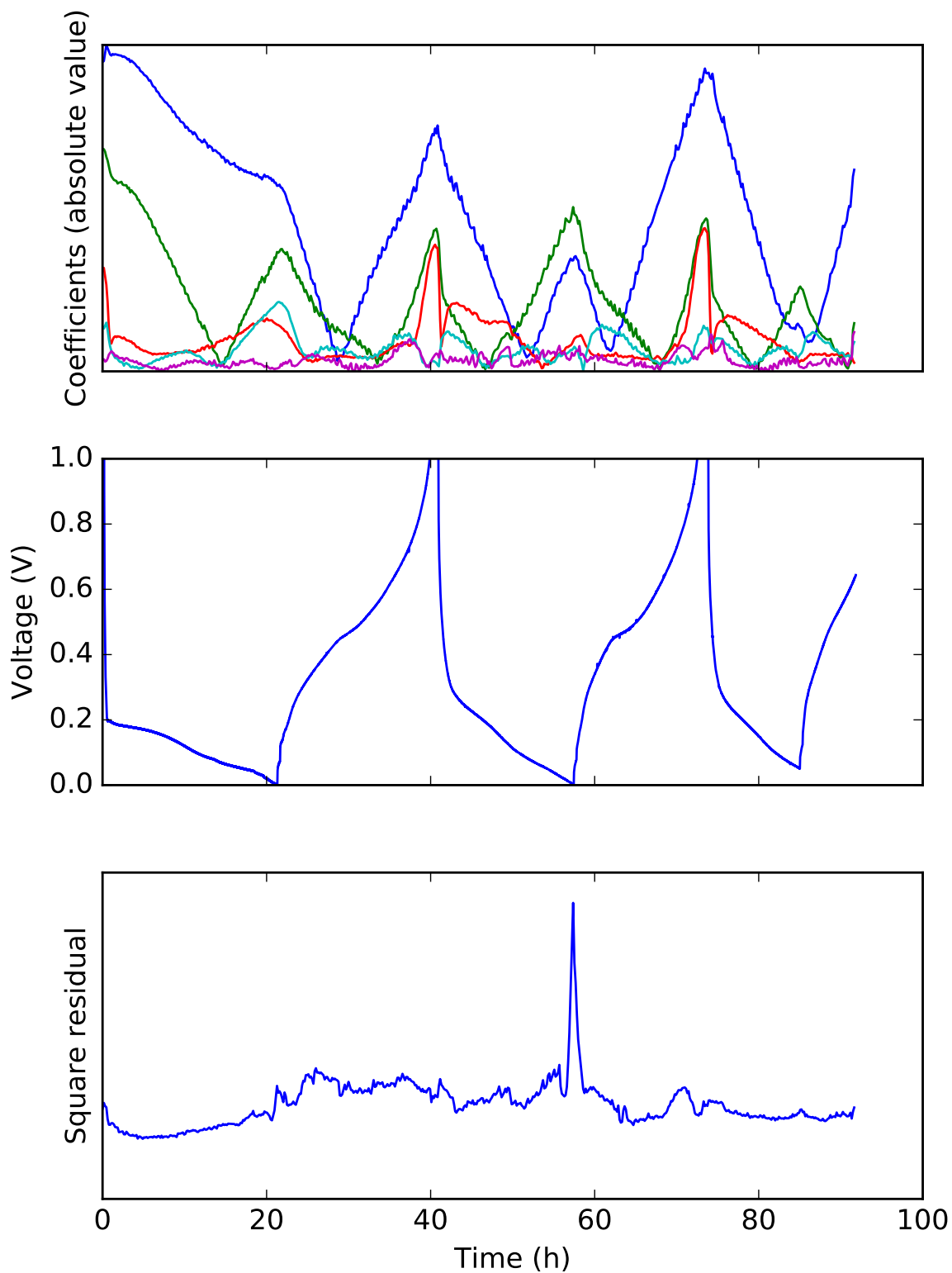


Figure 5.5: Coefficients of PCA components during *in situ* cycling. The top graph shows the absolute magnitude of each coefficient (colours are the same as in the graph of the components), the middle graph shows the voltage of the cell, and the bottom graph shows the squared residual (χ^2) — all on the same time axis.

but only has one citation for the upper cutoff voltage: a paper by Li et al. [62] from 1999. Quiroga-González et al. [164] says:

“On the other hand, setting the [upper] voltage limit above 1 V may cause undesired reactions that do not have anything to do with the delithiation of Si, producing parasitic currents.”

but it is unclear what led them to this conclusion. Ruffo et al. [99] demonstrate that the capacity from a cell cycled with an upper voltage limit of 0.7 V limit exceeding that from a cell with a 2 V limit after about 30 cycles.

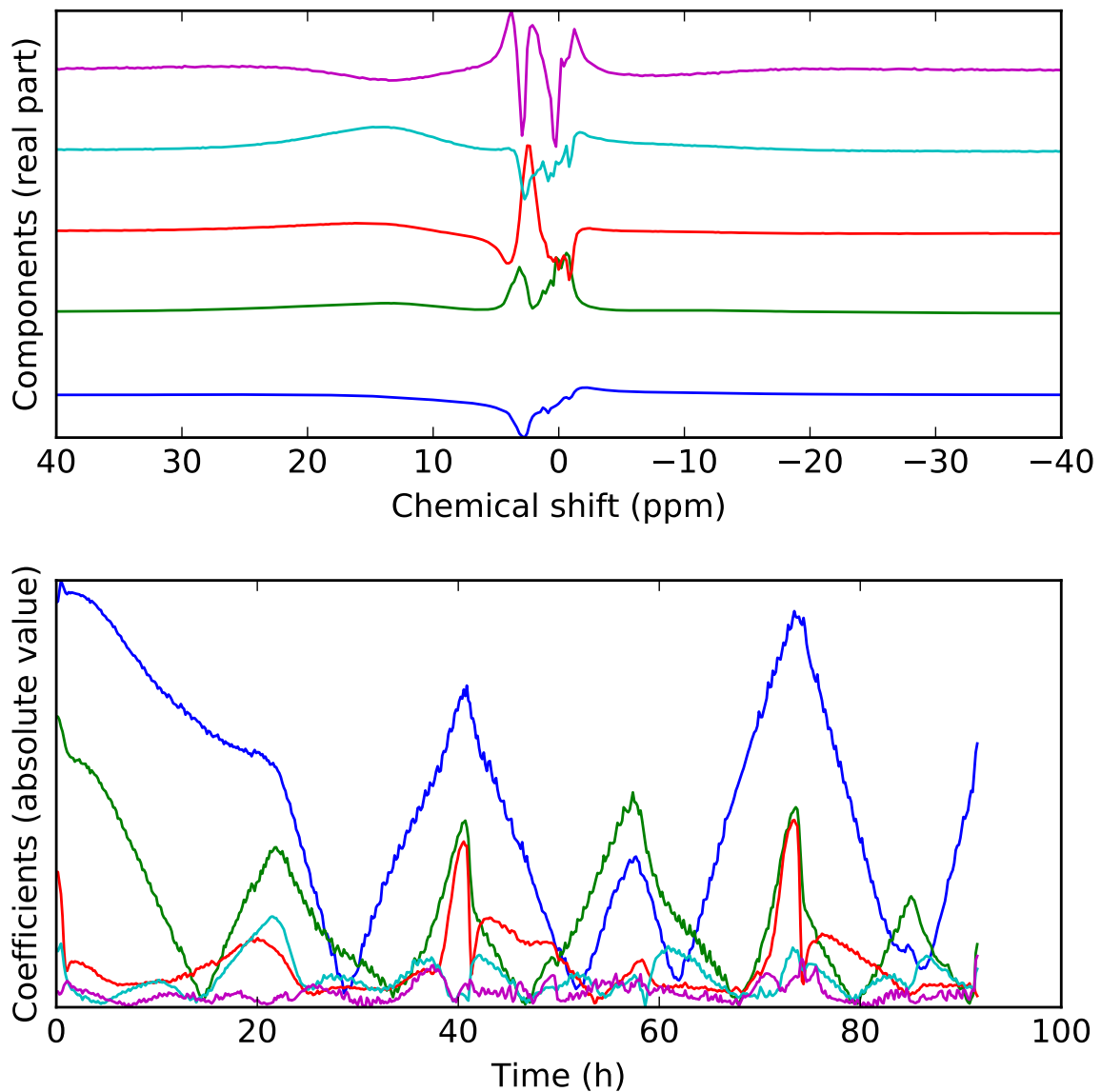


Figure 5.6: Real part of the central (diamagnetic Li region) of the PCA component spectra, with the graph of the coefficients reproduced from Figure 5.5 for easy comparison.

As can be seen in Figure 5.6, the third PCA component has a sharp peak around

3 ppm, in the region which is assigned to the electrolyte and SEI. It is certainly plausible that this component arises from changes in the SEI which occur at high voltages *vs* Li|Li⁺. However, the nature of PCA means that it is difficult to interpret this in any more detail, as the component is a mixture of several spectra, some of which will be weighted negatively (because one material is being formed as the other is consumed).

5.2.2 NMF analysis

The NMF-based model discussed in subsection 1.6.3 relies on all the components having the same phase, so that after phase correction the real part of the spectrum will be non-negative. However, due to the skin depth effect (discussed in subsection 1.5.3), the phase of the NMR signal from the lithium metal counter electrode is behind those from the electrolyte and lithium silicides — the difference is found to be approximately 45°. The dendrites have a different phase from the bulk metal, so this phase offset is not even constant but changes during cycling as dendrites are formed and consumed. To avoid this confounding factor, therefore, frequencies above 50 ppm were removed using a digital filter before performing the NMF analysis.

The most intense signal, coloured blue in the graphs, grows during the first discharge and then stays roughly constant except at the top of charge. This can be explained by it being a combination of electrolyte and SEI, and its spectrum is also consistent with that explanation. The component marked in purple appears during the lithiation process, before giving way to the component marked in green as full lithiation approaches, and then to the component marked in yellow during the delithiation process. Looking at the spectra, the ‘purple’ component has a large peak at around 5 ppm, previously assigned to Li near isolated Si [122]. The green and yellow components, on the other hands, have peaks at 15 ppm and 20 ppm respectively, which suggest either a weak Knight shift in overlithiated material or Li near Si–Si ‘dumbbells’ — overlithiation is the only one of those which is plausible for the ‘green’ component at the bottom of discharge, while ‘dumbbells’ could be present in the ‘yellow’ component as lithium is being removed. Both the ‘green’ and ‘yellow’ components also have signal at negative chemical shifts indicative of highly shielded Li in overlithiated material; these negative shifts have previously been noted as metastable states which decay quickly to give materials with positive shifts [122].

The ‘red’ component is most interesting, as it concerns the top of charge (full delithiation, up to 3 V *vs* Li|Li⁺), and its NMR spectrum is entirely within the central peak assigned to electrolyte and SEI. Previous analyses (*e.g.* Key et al. [122] or Ogata et al. [60]) have ignored both the top of charge (as uninteresting) and the electrolyte peak (because it has been difficult to deconvolve it reproducibly). A possible interpretation of the behaviour of the ‘blue’ and ‘red’ components is that, at potentials above ~ 0.7 V *vs* Li|Li⁺, Li⁺ ions are stripped out of the SEI into the electrolyte. This would presumably disrupt

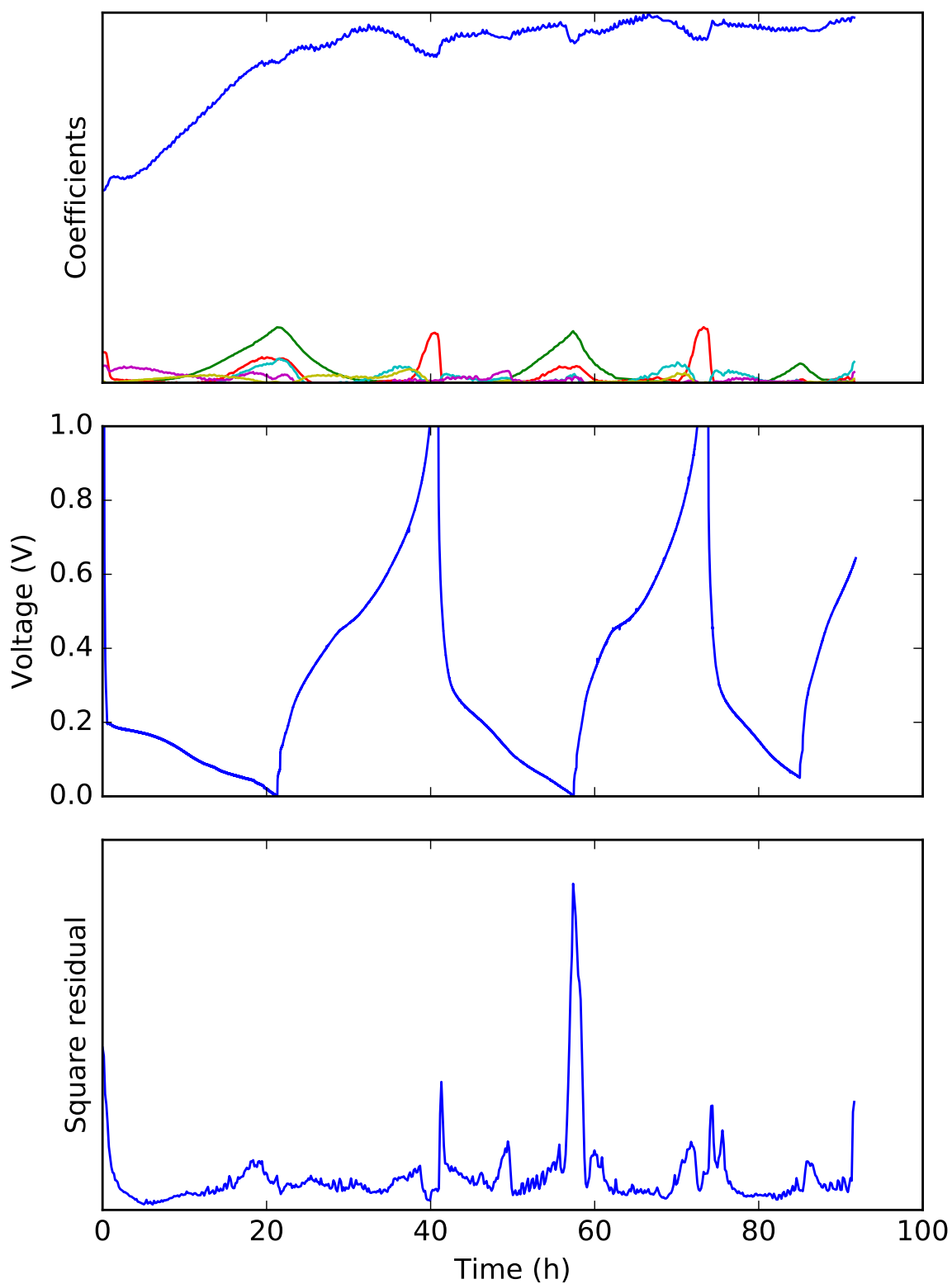


Figure 5.7: Coefficients of glsNMF components during *in situ* cycling. The top graph shows the absolute magnitude of each coefficient (colours are the same as in the graph of the components), the middle graph shows the voltage of the cell, and the bottom graph shows the squared residual (χ^2) — all on the same time axis.

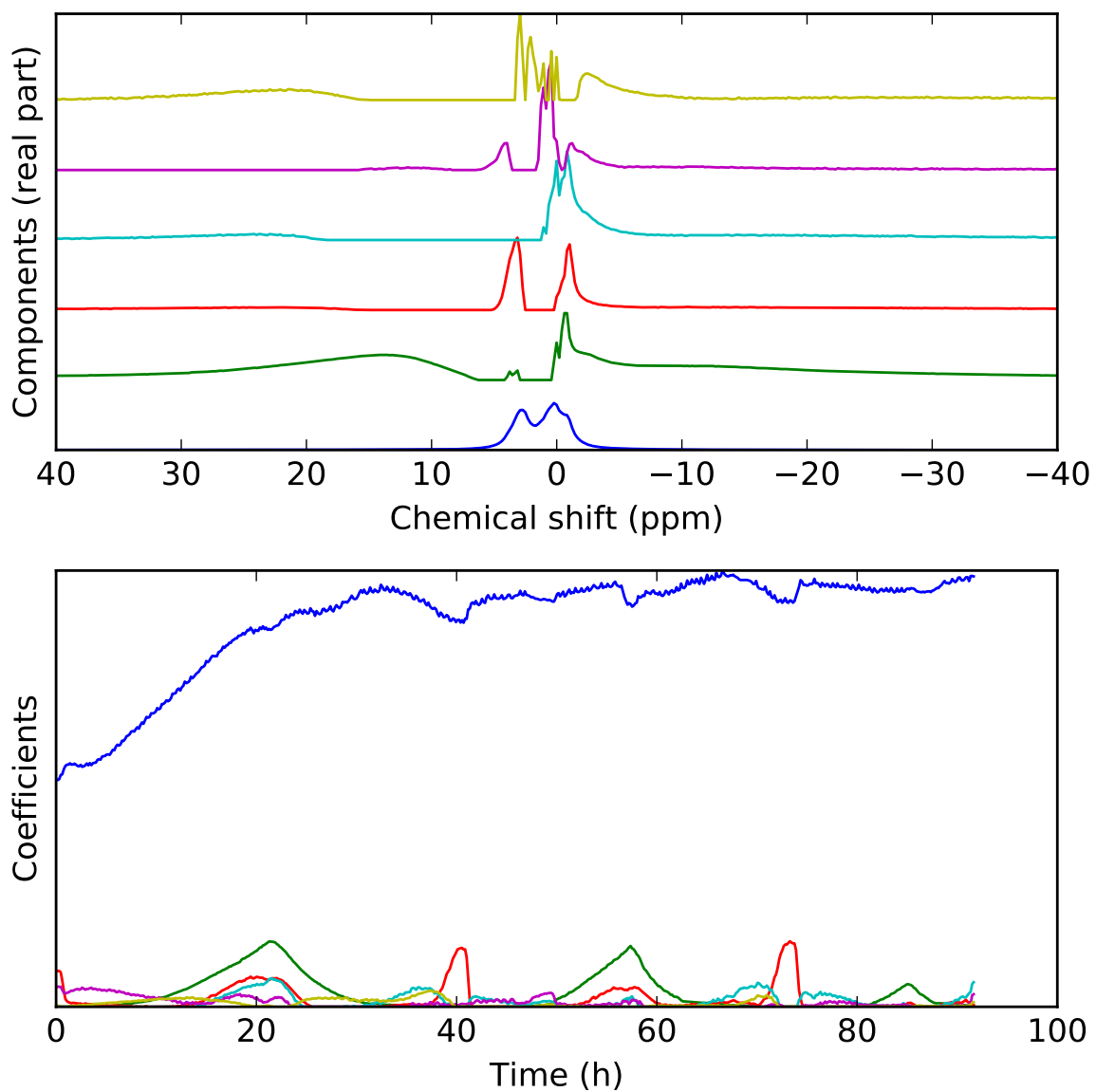


Figure 5.8: Real part of the central (diamagnetic Li region) of the glsNMF component spectra, with the graph of the coefficients reproduced from Figure 5.7 for easy comparison.

the structure of the SEI and lead to the effects noted by Quiroga-González et al. [164] and Ruffo et al. [99] of higher upper cutoff voltages leading to worse cycling performance.

5.2.3 Comparison of NMR and PCA results

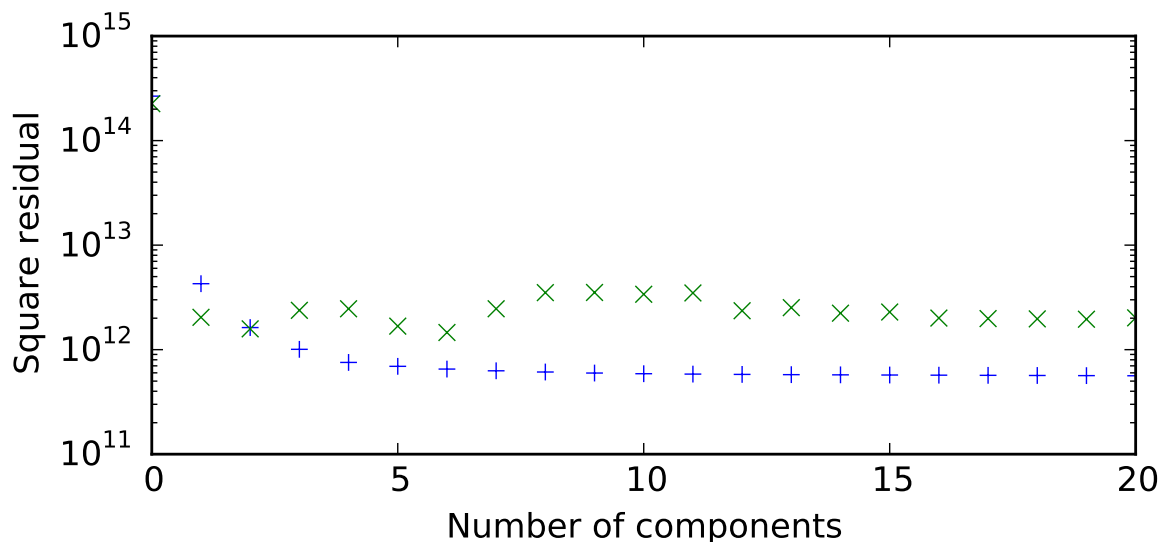


Figure 5.9: Goodness of fit (on a log scale) as a function of number of components for PCA (blue) and NMF (green).

Figure 5.9 shows how the agreement between calculated and experimental FIDs changes with the number of components used in the PCA and NMF fits. For the NMF, the residual starts increasing when the number of components goes above 6. Since it is always possible to get the same fit with 7 or more components as with 6 by setting the coefficient of the 7th and later components to 0, it is obvious that the NMF algorithm chosen does not always give optimal results. This is not all that surprising as the NMF problem has been shown to be NP-hard [133].

However, even if the NMF algorithm did produce optimal results, it would still give a worse fit than PCA with the same number of components as the PCA problem has fewer constraints on its solutions. The difference in fit quality between the optimal PCA decomposition and the optimal NMF decomposition can in fact be considered a metric of how well the assumptions embedded in the NMF constraints are valid for the experimental data in question — if there is little difference in the fit quality then NMF is a valid model. The question therefore remains open as to whether the difference in fit quality is primarily due to problems with the NMF algorithm used or to the assumed constraints not being justified.

Chapter 6

Conclusion

Unfortunately, none of the results of the experiments described in this dissertation have been as conclusive as I would have liked, and pressure of time has prevented me from following up all the leads or checking all possibilities. However, most of the software written during the course of my research is publicly available and will facilitate any attempts to continue this line of research and bring it to a more fruitful conclusion.

6.1 Summary of results

Linear least squares is a much more efficient algorithm than Metropolis Monte Carlo for fitting a $G(r)$ to experimental $S(Q)$ data which has been affected by a Q -dependent instrumental resolution function. `ProfFitS`' memory requirements are larger than those of `MCGRtof`, but not prohibitive on modern machines.

`RMCprofile` has been extended to cope with data from heterogeneous samples. Extensive refactoring and the addition of a suite of unit tests mean that the program will be easier to extend and enhance in the future. In addition to the unit tests, functional testing of both the old and new versions of `RMCprofile` against simulated data showed that the output of the two versions is broadly comparable. Using the newly added support for heterogeneous samples on synthetic data gave mixed results. A single set of experimental data may well be too ambiguous — refining against multiple datasets is to be recommended when possible.

However, analysis of experimental neutron scattering data from lithium silicide battery materials using `RMCprofile` gave inconclusive results. A major contributor to this is the fact that sample preparation was not reproducible enough to allow proper characterisation, and so it was not possible to take full advantage of the neutron scattering data.

Non-negative matrix factorisation is a model-free technique for separating *in situ* NMR data into additive components. It can provide insight not only into the well-resolved signals from the various lithium silicide phases but also into the behaviour of the central

electrolyte-plus-SEI peak. The combination of NMF and *in situ* NMR therefore represents a new avenue of investigation for the solid electrolyte interphase and its effects on cycling performance, not only for lithium silicides but for a wide range of electrode materials.

6.2 Future opportunities

As is perhaps to be expected, the research described in this dissertation has raised more new questions than it has answered. Some of these are detailed in this section.

6.2.1 Electrolytes

One of the greatest challenges in the neutron scattering experiments was the electrolyte. If natural abundance electrolyte was used, the incoherent scattering from ^1H nuclei in the SEI would have swamped the coherent scattering and made quantitative processing of the neutron scattering patterns almost impossible. Even the ^2H nuclei in the SEI formed by deuterated electrolyte caused enough incoherent scattering to be problematic. Usually, when preparing *ex situ* samples for NMR or XRD, the extracted material is washed with solvent (typically the same solvent used in the electrolyte) to remove the majority of the SEI. However, this was not feasible with the deuterated samples owing to the high cost of deuterated electrolytes. (Washing with natural abundance solvents would have risked small amounts of the washing solvent reacting with or being absorbed into the SEI and thereby introducing unwanted ^1H .)

The research by Wong et al. [32] into perfluoropolyether (PFPE) electrolytes presents a potential solution to this problem. PFPEs do not contain any hydrogen, so no expensive deuteration would be required for neutron scattering experiments, and the same solvent could be used for washing the extracted electrode material without the risk of introducing unwanted ^1H . Indeed, because there is no deuterium either, even the lower level of incoherent scattering caused by ^2H nuclei would be avoided.

Ideally a hydrogen-free binder material would also be required so that electrical connectivity can be maintained, avoiding the problems introduced by the presence of unreacted electrode material. Alternatively, scaling up a binder-free electrode material (such as the SiNWs on carbon fibre support used for *in situ* NMR experiments) to gram quantities would also give good electrochemical performance with a minimum of confounding scattering.

6.2.2 Improvements to RMCprofile

The RMC analysis in chapter 4 involved three consecutive RMC runs, each fitting the structures of different components of the mixture. If `RMCprofile` were able to fit to

different data sets with different weights simultaneously (*e.g.* samples with different phase fractions or samples with different isotope enrichment) then a single RMC calculation could have been done, obtaining a result that best accounts for all the experimental data. In cases where the phase fractions are not known, the ability to refine the phase fraction would also be useful. Implementing either of these ideas would require only modest changes to the internal structure of the program.

The process of preparing input data for `RMCprofile`, running the RMC calculations and then analysing the results is not particularly user-friendly at any stage. `RMCgui` and the `rmcanalysis` suite of tools promise to ameliorate this situation, but neither is yet in a functional state. If RMC is to be made more accessible then these projects will have to be completed and made available to users.

Bibliography

- [1] 2014 key world energy statistics. Technical report, International Energy Agency, Paris, 2014. URL <http://www.iea.org/publications/freepublications/publication/key-world-energy-statistics-2014.html>.
- [2] G. L. Barbose, S. Weaver, and N. Darghouth. Tracking the Sun VII: An historical summary of the installed price of photovoltaics in the United States from 1998–2013. Technical Report LBNL-6808E, E. O. Lawrence Berkeley National Laboratory, University of California, Sep 2014. URL <http://eetd.lbl.gov/publications/tracking-the-sun-vii-an-historical-su>.
- [3] N. L. Bindoff, P. A. Stott, K. M. AchutaRao, M. R. Allen, N. Gillett, D. Gutzler, K. Hansingo, G. Hegerl, Y. Hu, S. Jain, I. I. Mokhov, J. Overland, J. Perlwitz, R. Sebbari, and X. Zhang. *Climate Change 2013: The Physical Science Basis*, chapter Detection and Attribution of Climate Change: from Global to Regional. Fifth Assessment Report of the Intergovernmental Panel on Climate Change. Cambridge University Press, 2013. URL <http://ipcc.ch/report/ar5/wg1/>.
- [4] B. Scrosati. History of lithium batteries. *Journal of Solid State Electrochemistry*, pages 1–8, 2011. doi: 10.1007/s10008-011-1386-8.
- [5] B. Dunn, H. Kamath, and J.-M. Tarascon. Electrical energy storage for the grid: A battery of choices. *Science*, 334(6058):928–935, 2011. doi: 10.1126/science.1212741.
- [6] N. Armaroli and V. Balzani. Towards an electricity-powered world. *Energy & Environmental Science*, 4:3193–3222, 2011. doi: 10.1039/C1EE01249E.
- [7] E. K. Hart and M. Z. Jacobson. The carbon abatement potential of high penetration intermittent renewables. *Energy & Environmental Science*, 5:6592–6601, 2012. doi: 10.1039/C2EE03490E.
- [8] C. J. Barnhart, M. Dale, A. R. Brandt, and S. M. Benson. The energetic implications of curtailing versus storing solar- and wind-generated electricity. *Energy & Environmental Science*, 6:2804–2810, 2013. doi: 10.1039/C3EE41973H.

- [9] M. Contestabile, G. J. Offer, R. Slade, F. Jaeger, and M. Thoennes. Battery electric vehicles, hydrogen fuel cells and biofuels. which will be the winner? *Energy & Environmental Science*, 4:3754–3772, 2011. doi: 10.1039/C1EE01804C.
- [10] W. Tahlil. The trouble with lithium. Technical report, Meridian International Research, Jan 2007. URL http://www.meridian-int-res.com/Projects/Lithium_Problem_2.pdf.
- [11] T. G. Goonan. Lithium use in batteries. Technical Report 1371, United States Geological Survey, 2012. URL <http://pubs.usgs.gov/circ/1371/>.
- [12] DOE hydrogen and fuel cells program 2013 annual report. Technical report, United States Department of Energy, Dec 2013. URL http://www.hydrogen.energy.gov/annual_progress13.html.
- [13] M. Carmo, D. L. Fritz, J. Mergel, and D. Stolten. A comprehensive review on PEM water electrolysis. *International Journal of Hydrogen Energy*, 38(12):4901–4934, 2013. doi: 10.1016/j.ijhydene.2013.01.151.
- [14] S. P. S. Badwal, S. Giddey, C. Munnings, and A. Kulkarni. Review of progress in high temperature solid oxide fuel cells. *Journal of the Australian Ceramics Society*, 50(1):23–37, 2014. URL <http://www.austceram.com/JAC-2014-1/ACS-Journal-2014-v1-23>.
- [15] F. Béguin, V. Presser, A. Balducci, and E. Frackowiak. Carbons and electrolytes for advanced supercapacitors. *Advanced Materials*, 26(14):2219–2251, 2014. doi: 10.1002/adma.201304137.
- [16] É. T. Shapovalov and V. V. Gerasimov. The electrochemical behavior of beryllium in aqueous solutions. *Soviet Atomic Energy*, 26:578–581, 1969. doi: 10.1007/BF01218767.
- [17] A. Venugopal, D. D. Macdonald, and R. Varma. Electrochemistry and corrosion of beryllium in buffered and unbuffered chloride solutions. *Journal of The Electrochemical Society*, 147(10):3673–3679, 2000. doi: 10.1149/1.1393957.
- [18] Y. Ito and T. Goto. Electrochemistry of nitrogen and nitrides in molten salts. *Journal of Nuclear Materials*, 344(1–3):128–135, 2005. doi: 10.1016/j.jnucmat.2005.04.030.
- [19] M. Lerch, J. Janek, K. D. Becker, S. Berendts, H. Boysen, T. Bredow, R. Dronskowski, S. G. Ebbinghaus, M. Kilo, M. W. Lumey, M. Martin, C. Reimann, E. Schweda, I. Valov, and H. D. Wiemhöfer. Oxide nitrides: From oxides to solids

- with mobile nitrogen ions. *Progress in Solid State Chemistry*, 37(2–3):81–131, 2009. doi: 10.1016/j.progsolidstchem.2009.11.004.
- [20] Y. Marcus. Thermodynamic functions of transfer of single ions from water to non-aqueous and mixed solvents: Part 3 - standard potentials of selected electrodes. *Pure and Applied Chemistry*, 57(8):1129–1132, 1985. doi: 10.1351/pac198557081129.
- [21] R. Wibowo, L. Aldous, S. E. Ward Jones, and R. G. Compton. The electrode potentials of the group I alkali metals in the ionic liquid N-butyl-N-methylpyrrolidinium bis(trifluoromethylsulfonyl)imide. *Chemical Physics Letters*, 492(4–6):276–280, 2010. doi: 10.1016/j.cplett.2010.04.063.
- [22] T. Ohzuku, Y. Iwakoshi, and K. Sawai. Formation of lithium-graphite intercalation compounds in nonaqueous electrolytes and their application as a negative electrode for a lithium ion (shuttlecock) cell. *Journal of The Electrochemical Society*, 140(9):2490–2498, 1993. doi: 10.1149/1.2220849.
- [23] Y. Nishi. The development of lithium ion secondary batteries. *The Chemical Record*, 1(5):406–413, 2001. doi: 10.1002/tcr.1024.
- [24] K. Mizushima, P. C. Jones, P. J. Wiseman, and J. B. Goodenough. Li_xCoO_2 ($0 < x \leq 1$): A new cathode material for batteries of high energy density. *Solid State Ionics*, 3-4(0):171–174, 1981. doi: 10.1016/0167-2738(81)90077-1.
- [25] A. Herold. Recherches sur les composés d’insertion du graphite. *Bulletin de la Société Chimique de France*, 187:999, 1955.
- [26] R. Juza and V. Wehle. Lithium-Graphit-Einlagerungsverbindungen. *Naturwissenschaften*, 52(20):560–560, 1965. doi: 10.1007/BF00631568.
- [27] A. N. Dey and B. P. Sullivan. The electrochemical decomposition of propylene carbonate on graphite. *Journal of The Electrochemical Society*, 117(2):222–224, 1970. doi: 10.1149/1.2407470.
- [28] R. Fong, U. von Sacken, and J. R. Dahn. Studies of lithium intercalation into carbons using nonaqueous electrochemical cells. *Journal of The Electrochemical Society*, 137(7):2009–2013, 1990. doi: 10.1149/1.2086855.
- [29] B. Scrosati. Recent advances in lithium ion battery materials. *Electrochimica Acta*, 45(15–16):2461–2466, 2000. doi: 10.1016/S0013-4686(00)00333-9.
- [30] K. Xu. Nonaqueous liquid electrolytes for lithium-based rechargeable batteries. *Chemical Reviews*, 104(10):4303–4418, 2004. doi: 10.1021/cr030203g.

- [31] T. Sato, T. Maruo, S. Marukane, and K. Takagi. Ionic liquids containing carbonate solvent as electrolytes for lithium ion cells. *Journal of Power Sources*, 138(1–2): 253–261, 2004. doi: 10.1016/j.jpowsour.2004.06.027.
- [32] D. H. C. Wong, J. L. Thelen, Y. Fu, D. Devaux, A. A. Pandya, V. S. Battaglia, N. P. Balsara, and J. M. DeSimone. Nonflammable perfluoropolyether-based electrolytes for lithium batteries. *Proceedings of the National Academy of Sciences*, 111(9): 3327–3331, 2014. doi: 10.1073/pnas.1314615111.
- [33] A. S. Arico, P. Bruce, B. Scrosati, J.-M. Tarascon, and W. van Schalkwijk. Nanostructured materials for advanced energy conversion and storage devices. *Nature Materials*, 4(5):366–377, May 2005. doi: 10.1038/nmat1368.
- [34] W. Xu, J. Wang, F. Ding, X. Chen, E. Nasybulin, Y. Zhang, and J.-G. Zhang. Lithium metal anodes for rechargeable batteries. *Energy & Environmental Science*, 7:513–537, 2014. doi: 10.1039/C3EE40795K.
- [35] M. Ishikawa, S. Yoshitake, M. Morita, and Y. Matsuda. In situ scanning vibrating electrode technique for the characterization of interface between lithium electrode and electrolytes containing additives. *Journal of The Electrochemical Society*, 141(12):L159–L161, 1994. doi: 10.1149/1.2059378.
- [36] F. Ding, W. Xu, G. L. Graff, J. Zhang, M. L. Sushko, X. Chen, Y. Shao, M. H. Engelhard, Z. Nie, J. Xiao, X. Liu, P. V. Sushko, J. Liu, and J.-G. Zhang. Dendrite-free lithium deposition via self-healing electrostatic shield mechanism. *Journal of the American Chemical Society*, 135(11):4450–4456, 2013. doi: 10.1021/ja312241y.
- [37] M. Z. Mayers, J. W. Kaminski, and T. F. Miller. Suppression of dendrite formation via pulse charging in rechargeable lithium metal batteries. *The Journal of Physical Chemistry C*, 116(50):26214–26221, 2012. doi: 10.1021/jp309321w.
- [38] T.-F. Yi, L.-J. Jiang, J. Shu, C.-B. Yue, R.-S. Zhu, and H.-B. Qiao. Recent development and application of $\text{Li}_4\text{Ti}_5\text{O}_{12}$ as anode material of lithium ion battery. *Journal of Physics and Chemistry of Solids*, 71(9):1236–1242, 2010. doi: 10.1016/j.jpics.2010.05.001.
- [39] T. Ohzuku, A. Ueda, and N. Yamamoto. Zerostrain insertion material of $\text{Li}[\text{Li}_{1/3}\text{Ti}_{5/3}]\text{O}_4$ for rechargeable lithium cells. *Journal of The Electrochemical Society*, 142(5):1431–1435, 1995. doi: 10.1149/1.2048592.
- [40] J. Cabana, L. Monconduit, D. Larcher, and M. R. Palacín. Beyond intercalation-based Li-ion batteries: The state of the art and challenges of electrode materials re-

- acting through conversion reactions. *Advanced Materials*, 22(35):E170–E192, 2010. doi: 10.1002/adma.201000717.
- [41] H. Inoue. High capacity negative-electrode materials next to carbon: NEXELION. In *ECS Transactions*. ECS, 2006. Presented at the International Meeting on Lithium Batteries 2006, Biarritz, France, June 18-23, 2006. Abstract No. 228.
- [42] W. H. Woodford, W. C. Carter, and Y.-M. Chiang. Design criteria for electrochemical shock resistant battery electrodes. *Energy & Environmental Science*, 5: 8014–8024, 2012. doi: 10.1039/C2EE21874G.
- [43] D. Larcher, S. Beattie, M. Morcrette, K. Edstrom, J.-C. Jumas, and J.-M. Tarascon. Recent findings and prospects in the field of pure metals as negative electrodes for Li-ion batteries. *Journal of Materials Chemistry*, 17:3759–3772, 2007. doi: 10.1039/B705421C.
- [44] C. van der Marel, G. J. B. Vinke, and W. van der Lugt. The phase diagram of the system lithium-silicon. *Solid State Communications*, 54(11):917–919, 1985. doi: 10.1016/0038-1098(85)90155-3.
- [45] R. Nesper and H. G. von Schnering. $\text{Li}_{21}\text{Si}_5$, a Zintl phase as well as a Hume-Rothery phase. *Journal of Solid State Chemistry*, 70(1):48–57, 1987. doi: 10.1016/0022-4596(87)90176-9.
- [46] M. Zeilinger, D. Benson, U. Häussermann, and T. F. Fässler. Single crystal growth and thermodynamic stability of $\text{Li}_{17}\text{Si}_4$. *Chemistry of Materials*, 25(9):1960–1967, 2013. doi: 10.1021/cm400612k.
- [47] M. Zeilinger, I. M. Kurylyshyn, U. Häussermann, and T. F. Fässler. Revision of the Li–Si phase diagram: Discovery and single-crystal X-ray structure determination of the high-temperature phase $\text{Li}_{4.11}\text{Si}$. *Chemistry of Materials*, 25(22):4623–4632, 2013. doi: 10.1021/cm4029885.
- [48] L. A. Stearns, J. Gryko, J. Diefenbacher, G. K. Ramachandran, and P. F. McMillan. Lithium monosilicide (LiSi), a low-dimensional silicon-based material prepared by high pressure synthesis: NMR and vibrational spectroscopy and electrical properties characterization. *Journal of Solid State Chemistry*, 173(1):251–258, 2003. doi: 10.1016/S0022-4596(03)00045-8.
- [49] M. N. Obrovac and L. Christensen. Structural changes in silicon anodes during lithium insertion/extraction. *Electrochemical and Solid-State Letters*, 7(5):A93–A96, 2004. doi: 10.1149/1.1652421.

- [50] T. K.-J. Köster, E. Salager, A. J. Morris, B. Key, V. Seznéc, M. Morcrette, C. J. Pickard, and C. P. Grey. Resolving the different silicon clusters in $\text{Li}_{12}\text{Si}_7$ by ^{29}Si and $^{6,7}\text{Li}$ solid-state NMR spectroscopy. *Angewandte Chemie International Edition*, 50(52):12591–12594, 2011. doi: 10.1002/anie.201105998.
- [51] Yu Hong Xu, Ge Ping Yin, and Peng Jian Zuo. Geometric and electronic studies of $\text{Li}_{15}\text{Si}_4$ for silicon anode. *Electrochimica Acta*, 54(2):341–345, 2008. doi: 10.1016/j.electacta.2008.07.083.
- [52] Q. Zhang, W. Zhang, W. Wan, Y. Cui, and E. Wang. Lithium insertion in silicon nanowires: An *ab initio* study. *Nano Letters*, 10(9):3243–3249, 2010. doi: 10.1021/nl904132v.
- [53] A. J. Morris, R. J. Needs, E. Salager, C. P. Grey, and C. J. Pickard. Lithiation of silicon via lithium Zintl-defect complexes from first principles. *Physical Review B*, 87:174108, May 2013. doi: 10.1103/PhysRevB.87.174108.
- [54] Y. Kubota, M. C. Sison Escaño, H. Nakanishi, and H. Kasai. Crystal and electronic structure of $\text{Li}_{15}\text{Si}_4$. *Journal of Applied Physics*, 102(5), 2007. doi: 10.1063/1.2775999.
- [55] C. J. Wen and R. A. Huggins. Chemical diffusion in intermediate phases in the lithium-silicon system. *Journal of Solid State Chemistry*, 37(3):271–278, 1981. doi: 10.1016/0022-4596(81)90487-4.
- [56] W. J. Weydanz, M. Wohlfahrt-Mehrens, and R. A. Huggins. A room temperature study of the binary lithium-silicon and the ternary lithium-chromium-silicon system for use in rechargeable lithium batteries. *Journal of Power Sources*, 81-82(0):237–242, 1999. doi: 10.1016/S0378-7753(99)00139-1.
- [57] P. Limthongkul, Y.-I. Jang, N. J. Dudney, and Y.-M. Chiang. Electrochemically-driven solid-state amorphization in lithium-silicon alloys and implications for lithium storage. *Acta Materialia*, 51(4):1103–1113, 2003. doi: 10.1016/S1359-6454(02)00514-1.
- [58] T. D. Hatchard and J. R. Dahn. In situ XRD and electrochemical study of the reaction of lithium with amorphous silicon. *Journal of The Electrochemical Society*, 151(6):A838–A842, 2004. doi: 10.1149/1.1739217.
- [59] J. Danet, T. Brousse, K. Rasim, D. Guyomard, and P. Moreau. Valence electron energy-loss spectroscopy of silicon negative electrodes for lithium batteries. *Physical Chemistry Chemical Physics*, 12:220–226, 2010. doi: 10.1039/B915245H.

- [60] K. Ogata, E. Salager, C. J. Kerr, A. E. Fraser, C. Ducati, A. J. Morris, S. Hofmann, and C. P. Grey. Revealing lithium–silicide phase transformations in nano-structured silicon-based lithium ion batteries via in situ NMR spectroscopy. *Nature Communications*, 5, Feb 2014. doi: 10.1038/ncomms4217.
- [61] J. B. Goodenough. Electrochemical energy storage in a sustainable modern society. *Energy & Environmental Science*, 7:14–18, 2014. doi: 10.1039/C3EE42613K.
- [62] H. Li, X. Huang, L. Chen, Z. Wu, and Y. Liang. A high capacity nano-Si composite anode material for lithium rechargeable batteries. *Electrochemical and Solid-State Letters*, 2(11):547–549, 1999. doi: 10.1149/1.1390899.
- [63] X. H. Liu, L. Zhong, S. Huang, S. X. Mao, Ting Zhu, and J. Y. Huang. Size-dependent fracture of silicon nanoparticles during lithiation. *ACS Nano*, 6(2):1522–1531, 2012. doi: 10.1021/nm204476h.
- [64] M. Winter and J. O. Besenhard. Electrochemical lithiation of tin and tin-based intermetallics and composites. *Electrochimica Acta*, 45(1–2):31–50, 1999. doi: 10.1016/S0013-4686(99)00191-7.
- [65] R. A. Huggins and W. D. Nix. Decrepitation model for capacity loss during cycling of alloys in rechargeable electrochemical systems. *Ionics*, 6(1–2):57–63, 2000. doi: 10.1007/BF02375547.
- [66] L. Y. Beaulieu, T. D. Hatchard, A. Bonakdarpour, M. D. Fleischauer, and J. R. Dahn. Reaction of Li with alloy thin films studied by in situ AFM. *Journal of The Electrochemical Society*, 150(11):A1457–A1464, 2003. doi: 10.1149/1.1613668.
- [67] J. Graetz, C. C. Ahn, R. Yazami, and B. Fultz. Highly reversible lithium storage in nanostructured silicon. *Electrochemical and Solid-State Letters*, 6(9):A194–A197, 2003. doi: 10.1149/1.1596917.
- [68] B. A. Boukamp, G. C. Lesh, and R. A. Huggins. Allsolid lithium electrodes with mixedconductor matrix. *Journal of The Electrochemical Society*, 128(4):725–729, 1981. doi: 10.1149/1.2127495.
- [69] R. D. Deshpande, J. Li, Y.-T. Cheng, and M. W. Verbrugge. Liquid metal alloys as self-healing negative electrodes for lithium ion batteries. *Journal of The Electrochemical Society*, 158(8):A845–A849, 2011. doi: 10.1149/1.3591094.
- [70] M. N. Obrovac and L. J. Krause. Reversible cycling of crystalline silicon powder. *Journal of The Electrochemical Society*, 154(2):A103–A108, 2007. doi: 10.1149/1.2402112.

- [71] U. Kasavajjula, C. Wang, and A. J. Appleby. Nano- and bulk-silicon-based insertion anodes for lithium-ion secondary cells. *Journal of Power Sources*, 163(2):1003–1039, 2007. doi: 10.1016/j.jpowsour.2006.09.084.
- [72] J.-S. Bridel, T. Azais, M. Morcrette, J.-M. Tarascon, and D. Larcher. Key parameters governing the reversibility of Si/carbon/CMC electrodes for Li-ion batteries. *Chemistry of Materials*, 22(3):1229–1241, 2010. doi: 10.1021/cm902688w.
- [73] J.-S. Bridel. *Optimisation de composites silicium-polymère-carbone pour électrodes négatives d’accumulateurs lithium-ion: Synthèse et réactivité*. PhD thesis, Université de Picardie Jules Verne, Nov 2010.
- [74] I. Kovalenko, B. Zdyrko, A. Magasinski, B. Hertzberg, Z. Milicev, R. Burtovyy, I. Luzinov, and G. Yushin. A major constituent of brown algae for use in high-capacity Li-ion batteries. *Science*, 334(6052):75–79, 2011. doi: 10.1126/science.1209150.
- [75] C. Joyce, L. Trahey, S. A. Bauer, F. Dogan, and J. T. Vaughey. Metallic copper binders for lithium-ion battery silicon electrodes. *Journal of The Electrochemical Society*, 159(6):A909–A914, 2012. doi: 10.1149/2.107206jes.
- [76] J. W. Kim, J. H. Ryu, K. T. Lee, and S. M. Oh. Improvement of silicon powder negative electrodes by copper electroless deposition for lithium secondary batteries. *Journal of Power Sources*, 147(1–2):227–233, 2005. doi: 10.1016/j.jpowsour.2004.12.041.
- [77] J. H. Ryu, J. W. Kim, Y.-E. Sung, and S. M. Oh. Failure modes of silicon powder negative electrode in lithium secondary batteries. *Electrochemical and Solid-State Letters*, 7(10):A306–A309, 2004. doi: 10.1149/1.1792242.
- [78] A. K. Kercher, J. O. Kiggans, and N. J. Dudney. Carbon fiber paper cathodes for lithium ion batteries. *Journal of The Electrochemical Society*, 157(12):A1323–A1327, 2010. doi: 10.1149/1.3495711.
- [79] S. K. Martha, J. O. Kiggans, J. Nanda, and N. J. Dudney. Advanced lithium battery cathodes using dispersed carbon fibers as the current collector. *Journal of The Electrochemical Society*, 158(9):A1060–A1066, 2011. doi: 10.1149/1.3611436.
- [80] S. K. Martha, E. Markevich, V. Burgel, G. Salitra, E. Zinigrad, B. Markovsky, H. Sclar, Z. Pramovich, O. Heik, D. Aurbach, I. Exnar, H. Buqa, T. Drezen, G. Semrau, M. Schmidt, D. Kovacheva, and N. Saliyski. A short review on surface chemical aspects of Li batteries: A key for a good performance. *Journal of Power Sources*, 189(1):288–296, 2009. doi: 10.1016/j.jpowsour.2008.09.084.

- [81] J. F. Snyder, E. L. Wong, and C. W. Hubbard. Evaluation of commercially available carbon fibers, fabrics, and papers for potential use in multifunctional energy storage applications. *Journal of The Electrochemical Society*, 156(3):A215–A224, 2009. doi: 10.1149/1.3065070.
- [82] M. Holzapfel, H. Buqa, L. J. Hardwick, M. Hahn, A. Würsig, W. Scheifele, P. Novák, R. Kötz, C. Veit, and F.-M. Petrat. Nano silicon for lithium-ion batteries. *Electrochimica Acta*, 52(3):973–978, 2006. doi: 10.1016/j.electacta.2006.06.034.
- [83] Y. Zhao, X. Liu, H. Li, T. Zhai, and H. Zhou. Hierarchical micro/nano porous silicon Li-ion battery anodes. *Chemical Communications*, 48:5079–5081, 2012. doi: 10.1039/C2CC31476B.
- [84] A. Magasinski, P. Dixon, B. Hertzberg, A. Kvit, J. Ayala, and G. Yushin. High-performance lithium-ion anodes using a hierarchical bottom-up approach. *Nature Materials*, 9(4):353–358, Apr 2010. doi: 10.1038/nmat2725.
- [85] L.-F. Cui, Y. Yang, C.-M. Hsu, and Y. Cui. Carbon-silicon core-shell nanowires as high capacity electrode for lithium ion batteries. *Nano Letters*, 9(9):3370–3374, 2009. doi: 10.1021/nl901670t.
- [86] H. Kim, M. Seo, M.-H. Park, and J. Cho. A critical size of silicon nano-anodes for lithium rechargeable batteries. *Angewandte Chemie International Edition*, 49(12): 2146–2149, 2010. doi: 10.1002/anie.200906287.
- [87] S. R. Gowda, V. Pushparaj, S. Herle, G. Girishkumar, J. G. Gordon, H. Gullapalli, X. Zhan, P. M. Ajayan, and A. L. M. Reddy. Three-dimensionally engineered porous silicon electrodes for Li ion batteries. *Nano Letters*, 12(12):6060–6065, 2012. doi: 10.1021/nl302114j.
- [88] G. W. Zhou, H. Li, H. P. Sun, D. P. Yu, Y. Q. Wang, X. J. Huang, L. Q. Chen, and Z. Zhang. Controlled Li doping of Si nanowires by electrochemical insertion method. *Applied Physics Letters*, 75(16):2447–2449, 1999. doi: 10.1063/1.125043.
- [89] C. K. Chan, H. Peng, G. Liu, K. McIlwrath, X. F. Zhang, R. A. Huggins, and Y. Cui. High-performance lithium battery anodes using silicon nanowires. *Nature Nanotechnology*, 3(1):31–35, 2008. doi: 10.1038/nnano.2007.411.
- [90] C. K. Chan, X. F. Zhang, and Y. Cui. High capacity li ion battery anodes using ge nanowires. *Nano Letters*, 8(1):307–309, 2008. doi: 10.1021/nl0727157.
- [91] J. W. Choi, L. Hu, L. Cui, J. R. McDonough, and Y. Cui. Metal current collector-free freestanding silicon-carbon 1D nanocomposites for ultralight anodes in lithium

- ion batteries. *Journal of Power Sources*, 195(24):8311–8316, 2010. doi: 10.1016/j.jpowsour.2010.06.108.
- [92] C. K. Chan, R. Ruffo, S. S. Hong, and Y. Cui. Surface chemistry and morphology of the solid electrolyte interphase on silicon nanowire lithium-ion battery anodes. *Journal of Power Sources*, 189(2):1132–1140, 2009. doi: 10.1016/j.jpowsour.2009.01.007.
- [93] X. H. Liu, L. Q. Zhang, L. Zhong, Y. Liu, H. Zheng, J. W. Wang, J.-H. Cho, S. A. Dayeh, S. T. Picraux, J. P. Sullivan, S. X. Mao, Z. Z. Ye, and J. Y. Huang. Ultrafast electrochemical lithiation of individual Si nanowire anodes. *Nano Letters*, 11(6):2251–2258, 2011. doi: 10.1021/nl200412p.
- [94] X. H. Liu and J. Y. Huang. In situ TEM electrochemistry of anode materials in lithium ion batteries. *Energy & Environmental Science*, 4:3844–3860, 2011. doi: 10.1039/C1EE01918J.
- [95] X. H. Liu, H. Zheng, L. Zhong, S. Huang, K. Karki, L. Q. Zhang, Y. Liu, A. Kushima, W. T. Liang, J. W. Wang, Jeong-Hyun Cho, Eric Epstein, Shadi A. Dayeh, S. T. Picraux, Ting Zhu, Ju Li, J. P. Sullivan, John Cumings, Chunsheng Wang, S. X. Mao, Z. Z. Ye, S. Zhang, and J. Y. Huang. Anisotropic swelling and fracture of silicon nanowires during lithiation. *Nano Letters*, 11(8):3312–3318, 2011. doi: 10.1021/nl201684d.
- [96] C. K. Chan, R. N. Patel, M. J. O’Connell, B. A. Korgel, and Y. Cui. Solution-grown silicon nanowires for lithium-ion battery anodes. *ACS Nano*, 4(3):1443–1450, 2010. doi: 10.1021/nn901409q.
- [97] K. Peng, J. Jie, W. Zhang, and S.-T. Lee. Silicon nanowires for rechargeable lithium-ion battery anodes. *Applied Physics Letters*, 93(3):033105, 2008. doi: 10.1063/1.2929373.
- [98] X.-L. Wang and W.-Q. Han. Graphene enhances li storage capacity of porous single-crystalline silicon nanowires. *ACS Applied Materials & Interfaces*, 2(12):3709–3713, 2010. doi: 10.1021/am100857h.
- [99] R. Ruffo, S. S. Hong, C. K. Chan, R. A. Huggins, and Y. Cui. Impedance analysis of silicon nanowire lithium ion battery anodes. *The Journal of Physical Chemistry C*, 113(26):11390–11398, 2009. doi: 10.1021/jp901594g.
- [100] Y. F. Gao and M. Zhou. Strong stress-enhanced diffusion in amorphous lithium alloy nanowire electrodes. *Journal of Applied Physics*, 109(1):014310, 2011. doi: 10.1063/1.3530738.

- [101] R. Nesper. Structure and chemical bonding in Zintl-phases containing lithium. *Progress in Solid State Chemistry*, 20(1):1–45, 1990. doi: 10.1016/0079-6786(90)90006-2.
- [102] D. A. Keen. A comparison of various commonly used correlation functions for describing total scattering. *Journal of Applied Crystallography*, 34(2):172–177, Apr 2001. doi: 10.1107/S0021889800019993.
- [103] D. J. Vine, G. J. Williams, B. Abbey, M. A. Pfeifer, J. N. Clark, M. D. de Jonge, I. McNulty, A. G. Peele, and K. A. Nugent. Ptychographic Fresnel coherent diffractive imaging. *Physical Review A*, 80:063823, Dec 2009. doi: 10.1103/PhysRevA.80.063823.
- [104] H. M. Rietveld. A profile refinement method for nuclear and magnetic structures. *Journal of Applied Crystallography*, 2(2):65–71, Jun 1969. doi: 10.1107/S0021889869006558.
- [105] J. Taylor, O. Arnold, J. Bilheaux, A. Buts, S. Campbell, M. Doucet, N. Draper, R. Fowler, M. Gigg, V. Lynch, A. Markvardsen, K. Palmén, P. Parker, P. Peterson, S. Ren, M. Reuter, A. Savici, R. Taylor, R. Tolchenov, R. Whitley, W. Zhou, and J. Zikovsky. Mantid, a high performance framework for reduction and analysis of neutron scattering data. In *Bulletin of the American Physical Society*, 2012. doi: 10.5286/software/mantid.
- [106] L. Pusztai and R. L. McGreevy. MCGR: An inverse method for deriving the pair correlation function. *Journal of Neutron Research*, 8(1):17–35, Jan 1999. doi: 10.1080/10238169908200234.
- [107] M. G. Tucker, M. T. Dove, and D. A. Keen. MCGRtof: Monte Carlo G(r) with resolution corrections for time-of-flight neutron diffractometers. *Journal of Applied Crystallography*, 34(6):780–782, 2001. doi: 10.1107/S0021889801015345.
- [108] N. Metropolis and S. Ulam. The Monte Carlo method. *Journal of the American Statistical Association*, 44(247):335–341, 1949. URL <http://www.jstor.org/stable/2280232>.
- [109] N. Metropolis, A. W. Rosenbluth, M. N. Rosenbluth, A. H. Teller, and E. Teller. Equation of state calculations by fast computing machines. *The Journal of Chemical Physics*, 21(6):1087–1092, 1953. doi: 10.1063/1.1699114.
- [110] R. L. McGreevy and L. Pusztai. Reverse Monte Carlo simulation: A new technique for the determination of disordered structures. *Molecular Simulation*, 1(6):359–367, 1988. doi: 10.1080/08927028808080958.

- [111] J. Timoshenko, A. Kuzmin, and J. Purans. An efficient implementation of the reverse Monte Carlo method for EXAFS analysis in crystalline materials. *Journal of Physics: Conference Series*, 430(1):012012, 2013. doi: 10.1088/1742-6596/430/1/012012.
- [112] A. L. Goodwin, R. L. Withers, and H.-B. Nguyen. Real-space refinement of single-crystal electron diffuse scattering and its application to $\text{Bi}_2\text{Ru}_2\text{O}_{7-\delta}$. *Journal of Physics: Condensed Matter*, 19(33):335216, 2007. doi: 10.1088/0953-8984/19/33/335216.
- [113] M. J. Cliffe, M. T. Dove, D. A. Drabold, and A. L. Goodwin. Structure determination of disordered materials from diffraction data. *Physical Review Letters*, 104(12):125501, Mar 2010. doi: 10.1103/PhysRevLett.104.125501.
- [114] M. J. Cliffe and A. L. Goodwin. Nanostructure determination from the pair distribution function: a parametric study of the INVERT approach. *Journal of Physics: Condensed Matter*, 25(45):454218, 2013. doi: 10.1088/0953-8984/25/45/454218.
- [115] M. G. Tucker, M. T. Dove, and D. A. Keen. Application of the reverse Monte Carlo method to crystalline materials. *Journal of Applied Crystallography*, 34(5):630–638, Oct 2001. doi: 10.1107/S002188980100930X.
- [116] G. S. Pawley. Unit-cell refinement from powder diffraction scans. *Journal of Applied Crystallography*, 14(6):357–361, Dec 1981. doi: 10.1107/S0021889881009618.
- [117] M. G. Tucker, D. A. Keen, M. T. Dove, A. L. Goodwin, and Q. Hui. RMCPProfile: reverse Monte Carlo for polycrystalline materials. *Journal of Physics: Condensed Matter*, 19(33):335218, 2007. doi: 10.1088/0953-8984/19/33/335218.
- [118] W. Montfrooij, R. L. McGreevy, R. Hadfield, and N. H. Andersen. Reverse Monte Carlo analysis of powder patterns. *Journal of Applied Crystallography*, 29(3):285–290, Jun 1996. doi: 10.1107/S0021889896000908.
- [119] R. Böhmer, K. R. Jeffrey, and M. Vogel. Solid-state Li NMR with applications to the translational dynamics in ion conductors. *Progress in Nuclear Magnetic Resonance Spectroscopy*, 50(2–3):87–174, 2007. doi: 10.1016/j.pnmrs.2006.12.001.
- [120] R. Bhattacharyya, B. Key, H. Chen, A. S. Best, A. F. Hollenkamp, and C. P. Grey. In situ NMR observation of the formation of metallic lithium microstructures in lithium batteries. *Nature Materials*, 9(6):504–510, Jun 2010. doi: 10.1038/nmat2764.
- [121] F. Chevallier, M. Letellier, M. Morcrette, J.-M. Tarascon, E. Frackowiak, J.-N. Rouzaud, and F. Béguin. In situ ^7Li -nuclear magnetic resonance observation of

- reversible lithium insertion into disordered carbons. *Electrochemical and Solid-State Letters*, 6(11):A225–A228, 2003. doi: 10.1149/1.1612011.
- [122] B. Key, R. Bhattacharyya, M. Morcrette, V. Seznéc, J.-M. Tarascon, and C. P. Grey. Real-time NMR investigations of structural changes in silicon electrodes for lithium-ion batteries. *Journal of the American Chemical Society*, 131(26):9239–9249, 2009. doi: 10.1021/ja8086278.
- [123] J.-B. Pouillet, D. M. Sima, and S. Van Huffel. MRS signal quantitation: A review of time- and frequency-domain methods. *Journal of Magnetic Resonance*, 195(2): 134–144, 2008. doi: 10.1016/j.jmr.2008.09.005.
- [124] H. Barkhuijsen, R. de Beer, W. M. M. J. Bovée, and D. van Ormondt. Retrieval of frequencies, amplitudes, damping factors, and phases from time-domain signals using a linear least-squares procedure. *Journal of Magnetic Resonance (1969)*, 61(3):465–481, 1985. doi: 10.1016/0022-2364(85)90187-8.
- [125] G. H. Golub and V. Pereyra. The differentiation of pseudoinverses and nonlinear least squares problems whose variables separate. *SIAM Journal on Numerical Analysis*, 10(2):413–432, Apr 1973. URL <http://www.jstor.org/stable/2156365>.
- [126] R. Stoyanova, A. C. Kuesel, and T. R. Brown. Application of principal-component analysis for NMR spectral quantitation. *Journal of Magnetic Resonance, Series A*, 115(2):265–269, 1995. doi: 10.1006/jmra.1995.1177.
- [127] M. A. Elliott, G. A. Walter, A. Swift, K. Vandeborne, J. C. Schotland, and J. S. Leigh. Spectral quantitation by principal component analysis using complex singular value decomposition. *Magnetic Resonance in Medicine*, 41(3):450–455, 1999. doi: 10.1002/(SICI)1522-2594(199903)41:3<450::AID-MRM4>3.0.CO;2-9.
- [128] Y. Wang, S. Van Huffel, E. Heyvaert, L. Vanhamme, N. Mastronardi, and P. Van Hecke. Magnetic resonance spectroscopic quantitation via complex principal component analysis. In *5th International Conference on Signal Processing*, volume 3, pages 2074–2077, 2000. ISBN 0-7803-5747-7. doi: 10.1109/ICOSP.2000.893514.
- [129] H. Witjes, W. J. Melssen, H. J. A. in 't Zandt, M. van der Graaf, A. Heerschap, and L. M. C. Buydens. Automatic correction for phase shifts, frequency shifts, and lineshape distortions across a series of single resonance lines in large spectral data sets. *Journal of Magnetic Resonance*, 144(1):35–44, 2000. doi: 10.1006/jmre.2000.2021.
- [130] C.-J. Lin. Projected gradient methods for nonnegative matrix factorization. *Neural Computation*, 19(10):2756–2779, Aug 2007. doi: 10.1162/neco.2007.19.10.2756.

- [131] C. Boutsidis and E. Gallopoulos. SVD based initialization: A head start for non-negative matrix factorization. *Pattern Recognition*, 41(4):1350–1362, 2008. doi: 10.1016/j.patcog.2007.09.010.
- [132] D. Donoho and V. Stodden. When does non-negative matrix factorization give a correct decomposition into parts? In S. Thrun, L. K. Saul, and B. Schölkopf, editors, *Advances in Neural Information Processing Systems 16*, pages 1141–1148. MIT Press, 2004.
- [133] S. A. Vavasis. On the complexity of nonnegative matrix factorization. *SIAM Journal on Optimization*, 20(3):1364–1377, 2010. doi: 10.1137/070709967.
- [134] P. Sajda, S. Du, T. R. Brown, R. Stoyanova, D. C. Shungu, X. Mao, and L. C. Parra. Nonnegative matrix factorization for rapid recovery of constituent spectra in magnetic resonance chemical shift imaging of the brain. *IEEE Transactions on Medical Imaging*, 23(12):1453–1465, Dec 2004. doi: 10.1109/TMI.2004.834626.
- [135] Q. Zhao, R. Stoyanova, S. Du, P. Sajda, and T. R. Brown. HiRes — a tool for comprehensive assessment and interpretation of metabolomic data. *Bioinformatics*, 22(20):2562–2564, 2006. doi: 10.1093/bioinformatics/btl428.
- [136] S. Tikole, V. Jaravine, V. Rogov, V. Dotsch, and P. Guntert. Peak picking NMR spectral data using non-negative matrix factorization. *BMC Bioinformatics*, 15(1): 46, 2014. doi: 10.1186/1471-2105-15-46.
- [137] B. Key. *Solid State NMR and Pair Distribution Function Studies of Silicon Electrodes for Lithium-Ion Batteries*. PhD thesis, Stony Brook University, Dec 2010.
- [138] R. Stoyanova and T. R. Brown. NMR spectral quantitation by principal component analysis. *NMR in Biomedicine*, 14(4):271–277, 2001. doi: 10.1002/nbm.700.
- [139] F. Pedregosa, G. Varoquaux, A. Gramfort, V. Michel, B. Thirion, O. Grisel, M. Blondel, P. Prettenhofer, R. Weiss, V. Dubourg, J. Vanderplas, A. Passos, D. Cournapeau, M. Brucher, M. Perrot, and É. Duchesnay. Scikit-learn: Machine learning in Python. *Journal of Machine Learning Research*, 12:2825–2830, Oct 2011. doi: noDOI.jmlr/v12/pedregosa11a.
- [140] T. Zito, N. Wilbert, L. Wiskott, and P. Berkes. Modular toolkit for data processing (MDP): a Python data processing framework. *Frontiers in Neuroinformatics*, 2(8), 2009. doi: 10.3389/neuro.11.008.2008.

- [141] J. W. Eaton, D. Bateman, and S. Hauberg. *GNU Octave version 3.0.1 manual: a high-level interactive language for numerical computations*. CreateSpace Independent Publishing Platform, 2009. ISBN 1441413006. URL <http://www.gnu.org/software/octave/doc/interpreter>.
- [142] R Core Team. *R: A Language and Environment for Statistical Computing*. R Foundation for Statistical Computing, Vienna, Austria, 2014. URL <http://www.R-project.org>.
- [143] G. Wilson, D. A. Aruliah, C. T. Brown, N. P. Chue Hong, M. Davis, R. T. Guy, S. H. D. Haddock, K. D. Huff, I. M. Mitchell, M. D. Plumbley, B. Waugh, E. P. White, and P. Wilson. Best practices for scientific computing. *PLoS Biology*, 12(1): e1001745, 01 2014. doi: 10.1371/journal.pbio.1001745.
- [144] N. Nethercote and J. Seward. Valgrind: A framework for heavyweight dynamic binary instrumentation. *SIGPLAN Notices*, 42(6):89–100, June 2007. doi: 10.1145/1273442.1250746.
- [145] L. Hatton. The T experiments: errors in scientific software. *Computational Science & Engineering*, 4(2):27–38, Apr 1997. doi: 10.1109/99.609829.
- [146] P. Peterson. F2PY: a tool for connecting Fortran and Python programs. *International Journal of Computational Science and Engineering*, 4(4):296–305, 2009. doi: 10.1504/IJCSE.2009.029165.
- [147] D. Hook and D. Kelly. Testing for trustworthiness in scientific software. In *ICSE Workshop on Software Engineering for Computational Science and Engineering, 2009 (SECSE '09)*, pages 59–64, May 2009. doi: 10.1109/SECSE.2009.5069163.
- [148] S. Wells. *Real-space Rigid Unit analysis of framework structures using Geometric Algebra*. PhD thesis, University of Cambridge, February 2003.
- [149] M. Litzkow, M. Livny, and M. Mutka. Condor – a hunter of idle workstations. In *Proceedings of the 8th International Conference of Distributed Computing Systems*, June 1988.
- [150] S. Ikeda and J. M. Carpenter. Wide-energy-range, high-resolution measurements of neutron pulse shapes of polyethylene moderators. *Nuclear Instruments and Methods in Physics Research Section A: Accelerators, Spectrometers, Detectors and Associated Equipment*, 239(3):536–544, 1985. doi: 10.1016/0168-9002(85)90033-6.
- [151] P. Thompson, D. E. Cox, and J. B. Hastings. Rietveld refinement of Debye-Scherrer synchrotron X-ray data from Al_2O_3 . *Journal of Applied Crystallography*, 20(2):79–83, Apr 1987. doi: 10.1107/S0021889887087090.

- [152] A. C. Larson and R. B. von Dreele. General structure analysis system (GSAS). Technical Report LAUR 86-748, Los Alamos National Laboratory, 2000. URL <https://subversion.xray.aps.anl.gov/EXPGUI/gsas/all/GSAS%20Manual.pdf>.
- [153] E. H. Moore. The fourteenth western meeting of the american mathematical society. *Bulletin of the American Mathematical Society*, 26(9):394–395, 06 1920. doi: 10.1090/S0002-9904-1920-03322-7.
- [154] R. Penrose. A generalized inverse for matrices. *Mathematical Proceedings of the Cambridge Philosophical Society*, 51:406–413, 7 1955. doi: 10.1017/S0305004100030401.
- [155] J. S. Seabold and J. Perktold. Statsmodels: Econometric and statistical modeling with Python. In *Proceedings of the 9th Python in Science Conference*, 2010. URL <http://statsmodels.sourceforge.net/>.
- [156] D. C. Montgomery and E. A. Peck. *Introduction to linear regression analysis*. Wiley series in probability and statistics. Wiley, 2nd edition, 1992. ISBN 9780471315650. URL <http://books.google.co.zw/books?id=GFIZAQAIAAJ>.
- [157] R. C. Whaley and J. Dongarra. Automatically tuned linear algebra software. Technical report, University of Tennessee, December 1997. URL <http://www.netlib.org/lapack/lawns/lawn131.ps>.
- [158] J. Li and J. R. Dahn. An *in situ* X-ray diffraction study of the reaction of Li with crystalline Si. *Journal of The Electrochemical Society*, 154(3):A156–A161, 2007. doi: 10.1149/1.2409862.
- [159] B. Key, M. Morcrette, J.-M. Tarascon, and C. P. Grey. Pair distribution function analysis and solid state NMR studies of silicon electrodes for lithium ion batteries: Understanding the (de)lithiation mechanisms. *Journal of the American Chemical Society*, 133(3):503–512, 2011. doi: 10.1021/ja108085d.
- [160] W. Y. Chow, R. Rajan, K. H. Muller, D. G. Reid, J. N. Skepper, W. C. Wong, R. A. Brooks, M. Green, D. Bihan, R. W. Farndale, D. A. Slatter, C. M. Shanahan, and M. J. Duer. NMR spectroscopy of native and in vitro tissues implicates polyADP ribose in biomineralization. *Science*, 344(6185):742–746, 2014. doi: 10.1126/science.1248167.
- [161] J. J. Katz and H. L. Crespi. Biologically important isotope hybrid compounds in NMR: ^1H Fourier transform NMR at unnatural abundance. *Pure and Applied Chemistry*, 32(1–4):221–250, 1972. doi: 10.1351/pac197232010221.

- [162] M. Gauthier, D. Mazouzi, D. Reyter, B. Lestriez, P. Moreau, D. Guyomard, and L. Roue. A low-cost and high performance ball-milled Si-based negative electrode for high-energy Li-ion batteries. *Energy & Environmental Science*, 6:2145–2155, 2013. doi: 10.1039/C3EE41318G.
- [163] W.-J. Zhang. A review of the electrochemical performance of alloy anodes for lithium-ion batteries. *Journal of Power Sources*, 196(1):13–24, 2011. doi: 10.1016/j.jpowsour.2010.07.020.
- [164] E. Quiroga-González, J. Carstensen, and H. Föll. Optimal conditions for fast charging and long cycling stability of silicon microwire anodes for lithium ion batteries, and comparison with the performance of other Si anode concepts. *Energies*, 6(10): 5145–5156, 2013. doi: 10.3390/en6105145.
- [165] K. Ogata. Growth mechanism and post-growth processing of silicon nanowires for electrical and optical applications. Master’s thesis, Department of Engineering, University of Cambridge, Dec 2009.
- [166] B. Bruns et al. MDB tools, 2001–2013. URL <https://github.com/brianb/mdbtools>.
- [167] F. W. H. Kossebau and A. Richardson. Okteta, 2008–2013. URL <http://userbase.kde.org/Okteta>.
- [168] J. J. Helmus and C. P. Jaroniec. Nmr glue: an open source Python package for the analysis of multidimensional NMR data. *Journal of Biomolecular NMR*, 55(4): 355–367, 2013. doi: 10.1007/s10858-013-9718-x.
- [169] T. E. Oliphant. Python for scientific computing. *Computing in Science & Engineering*, 9(3):10–20, 2007. doi: 10.1109/MCSE.2007.58.

Appendix A

Methods for samples and data provided by others

A.1 Materials synthesis

A.1.1 CVD-synthesised silicon nanowires and amorphous silicon

Silicon nanowires and amorphous silicon were provided by Dr Ken Ogata. They were synthesised by CVD using the following procedures, which are mostly the same as those described in Ogata et al. [60]:

Au (~ 50 nm, as measured by a quartz crystal balance) was evaporated onto 200- μm -thick CFGDL support (SGL group, GDL24AA, 99.9% carbon). The CFGDL substrate was transferred to a cold-wall CVD system (10 mbar base pressure), where they were heated in H_2 or Ar and subsequently exposed to H_2 or Ar-diluted SiH_4 for 10 min. An Ar or H_2/SiH_4 ratio of 200/20 sccm was used at 15 mbar (total pressure) at 450°C , resulting in crystalline SiNWs of ~ 60 nm in average diameter and >50 μm in length. The growth temperature values refer to pyrometer measurements (IMPAC IGA 8 Plus, single band 1.6 μm) using a carbon nanotube forest reference sample for which an emissivity of 1 is assumed. Upon air exposure for subsequent cell assembly, a ~ 2 nm native oxide layer forms on the SiNW surfaces. The mass of the SiNWs and Au catalyst loading of the support were measured using a calibrated microbalance (Sartorius, SE2-F) with a precision of 0.1 μg .

Further information can be found in Ogata [165].

A.2 Experimental procedures for data

A.2.1 MCGRtof data for aluminium phosphate

Neutron total scattering patterns for crystalline AlPO_4 were measured on the GEM instrument at the ISIS spallation neutron source. Banks 2, 4, 5 and 7 were used as input for MCGRtof. See Tucker et al. [107] for more information.

Appendix B

Methods for selected experiments not discussed in this dissertation

There were several experiments carried out by me singly or in collaboration with others which have not been included in this dissertation. Nevertheless, it was represented to me that including details of the methods used for those experiments would form a useful reference for others attempting similar work in the future.

B.1 Preparation of active materials

B.1.1 Slurry with CMC binder

1. Equal quantities of Silicon nanopowder <100 nm 633097-10G (Aldrich), Timcal super P Li carbon and carboxymethyl cellulose (CMC) (Aldrich) were weighed out into a stainless steel ball mill jar.
2. Deionised water was added at a ratio of 1 ml to every 20 mg of solid.
3. The jar was shaken on a Spex SamplePrep 8000M Mixer/Mill for 5 min.
4. Using a Pasteur pipette, a few drops each of the slurry were placed on to pre-weighed stainless steel disks.
5. The disks were dried in an oven at 80 °C.
6. When the first application had dried, the slurry was re-homogenised by milling for a further 1 min and reapplied on top of the first coating. This was repeated twice more for a total of 4 applications.
7. The disks were then dried overnight at 80 °C before weighing.

B.1.2 Mechanosynthesis of lithium silicide model compounds

1. The stainless steel ball mill jar and milling balls were dried in an oven at 80 °C.
2. Stoichiometric quantities of lithium metal * and silicon powder (325 mesh, Aldrich) were placed in the jar together with two milling balls. The jar was sealed before being removed from the Argon glove box.
3. The jar was shaken for 100 min using a Spex SamplePrep 8000M Mixer/Mill
4. The jar was brought back into the glove box and opened. A spatula was used to break up any aggregated material.
5. The jar was milled for a further 380 min to give a total of 8 h.

B.2 Cell assembly

B.2.1 Coin cells

CR2025 coin cells were assembled using the following procedure:

1. The metal components and the glass fibre separator are dried in air at 80 °C.
2. The base (cathode end) of the cell is labelled with the date and sample ID.
3. The plastic grip ring is inserted into the base.
4. The cathode material is added, taking care not to get any underneath the plastic grip ring.
5. A disc of glass fibre is added, to act as a separator.
6. If the cathode is not air sensitive, the preceding steps are done outside of the glove box and the partially assembled cell is now transferred in. Otherwise the entire assembly procedure is carried out in the glove box.
7. Electrolyte solution is pipetted onto the separator.
8. A disc of lithium ribbon, cut to be slightly smaller than the internal diameter of the cell, is placed on top of the separator.
9. The stainless steel current collector disc and the spring are added.
10. The top cover of the cell is added and the cell is sealed using the coin cell press.

*The ^7Li metal was supplied under oil. To remove this oil it was immersed in DMC and shaken vigorously to wash off the oil. The DMC was then poured off and the metal pieces dried *in vacuo*.

Appendix C

Open source programs for file formats used in my research

Many brands of NMR spectrometer and battery cycler (including all those used in the Grey group lab) save their data in proprietary file formats. While the manufacturers all provide programs which can access these files and analyse the data inside, these programs are costly, buggy, only run on certain operating systems and have limited features.

The manufacturers' software usually supports exporting to a (poorly documented) text format. However, when working with large datasets, the use of text files is very inefficient because they take up more disk space and RAM, and must be parsed whenever they are read in. Accessing slices, such as a single spectrum from a time series, from a dataset stored in a free-form text file cannot be done without reading in the whole file or at least a significant portion of it. Finally, often the text format omits important information which is present in the original file.

The files used by Bruker spectrometers for their NMR data are understood by many third party open source tools. However, none of the free or open source NMR data processing packages included in major directories of NMR software at the start of my research listed TecMag NMR data files among its capabilities. For electrochemical data the situation was even worse — no free software was available (or at least easily findable on internet search engines) for reading data files from any kind of battery cycler, and there was no available documentation on the file formats used by the Arbin and Bio-Logic software.

C.1 Arbin file format

The control software for Arbin battery cyclers is known as `MITS Pro` and runs on Windows PCs only. Its saved data files have the file extension `.res`. Arbin provide a macro for Microsoft Excel, called “Arbin Data Pro”, which can load `.res` files and import them into

Excel spreadsheets. Since Excel has a limit of 65535 rows in a single worksheet, any data file with more than 65534 data points (since one row is taken up by the column headers) is split across multiple sheets, which complicates plotting or exporting the data. This macro is only installed on the computers responsible for controlling the battery cyclers, meaning that whenever a bug in the macro, or even just running out of memory while trying to open a large data file, causes the computer to crash, data acquisition is interrupted for all the samples running on that cycler. Sometimes, these crashes cause data files to be corrupted so that the Arbin macro cannot open them.

Running the standard Unix `file` utility on a `.res` file reports that it is a “Microsoft Access Database”. The open source `mdbtools` package [166] allows reading of Access databases on Unix systems, so it was chosen as the basis of my code to read `.res` files. When a `.res` file has been corrupted by the cycler console crashing, MDBtools is usually able to open it and extract the uncorrupted portion of the data even when Arbin’s macro is unable to open the file.

However, the `mdbtools` package has relatively few features and is difficult to access from programming languages other than C, so the first step in processing the `.res` files is to pass the data directly from `mdbtools` into a `sqlite` database. The `sqlite` database is set up to have the same schema as the Access database in the `.res` file, with the addition of some extra tables to assist further processing. The view ‘`Capacity_View`’ uses the helper table ‘`Capacity_Sum_Table`’ to add the capacities and energies of individual discharge and charge steps to give overall net and gross capacities and energies. In certain cases the `.res` format does not store data points in the correct order, so the `sqlite` database also adds an index to ensure the correct ordering. The conversion from `.res` file to `sqlite` database is performed by the script `res2sqlite.py`.

C.2 Bio-Logic MPR format

The control software for the Bio-Logic VMP and VSP battery cyclers is called `EC-Lab` and, like the Arbin `MITS Pro` software, runs on Windows PCs only. Its saved data files have the file extension ‘`.mpr`’. The `EC-Lab` program allows exporting the data in a tab-separated text format with the extension ‘`.mpt`’. Depending on the version of `EC-Lab` used, the exported text file may or may not contain metadata such as the sample ID and the date and time when the data were recorded. The titles used in the column headings and the order of the columns in the exported data vary depending on the experimental setup and the version of the software used — for example, one version of the software will put the current in column 12 with the header “`<I>/mA`” while another has it in column 10 with the header “`I/mA`”. This variability complicates the writing of code to process the exported text.

Running the `file` utility on a `.mpt` file reports that it is “data” — in other words that it is an unrecognised binary file format. I could not find any documentation on the Bio-Logic website or elsewhere describing the file format, so the next step is to open it in a binary viewer and see if there are any obvious patterns. The `Okteta` binary editor [167] was used, as it has a helpful utility which displays the value of the data at the current cursor position when interpreted as any of several common integer or floating point representations.

C.2.1 Header and “VMP settings” block

Every `.mpr` file starts with the ASCII text “`BIO-LOGIC MODULAR FILE`”, followed by the ASCII substitute character (character number 26, which has the effect of stopping processing by some MS-DOS utilities which would otherwise treat the file as a text file), then 24 space characters and four null characters. After that comes a series of data blocks or ‘modules’, marked by the ASCII text “`MODULE`”, a descriptive name in ASCII (e.g. “`VMP settings`”), a 32-bit integer length, a 32-bit integer which is presumably a format version number, and a date in ASCII “`MM/DD/YY`” format, followed by the data contents of the ‘module’. See Figure C.1 for an example of the beginning of a `.mpr` file.

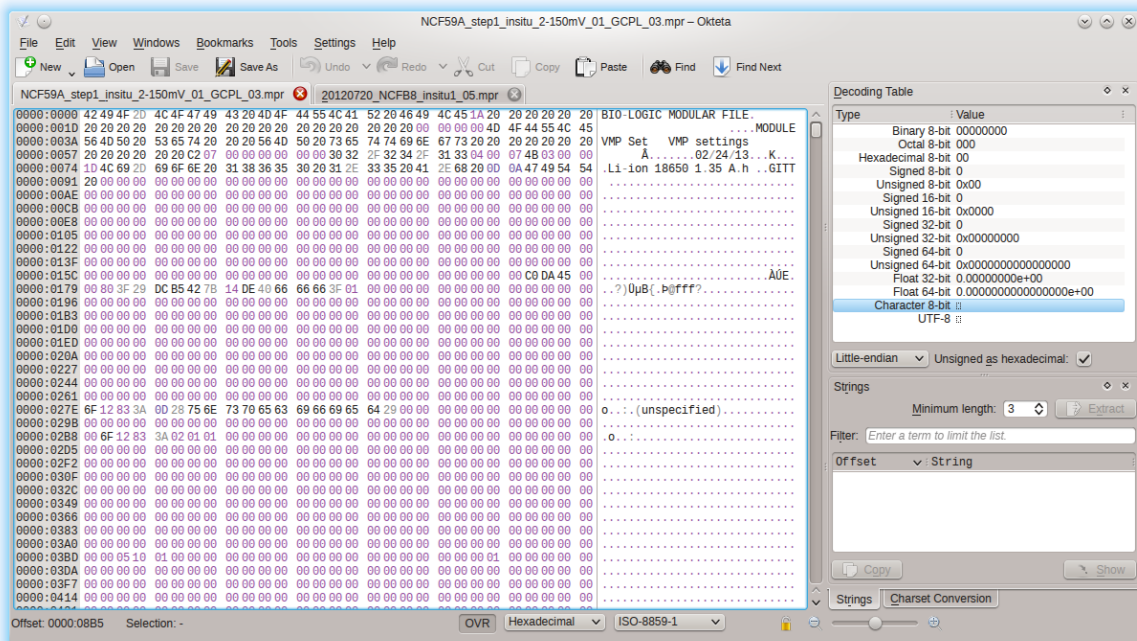


Figure C.1: The start of a `.mpr` file, viewed in `Okteta`, showing the “`BIO-LOGIC MODULAR FILE`” text and part of the “`VMP settings`” block.

Number of data points Number of columns Length in bytes Version Column types

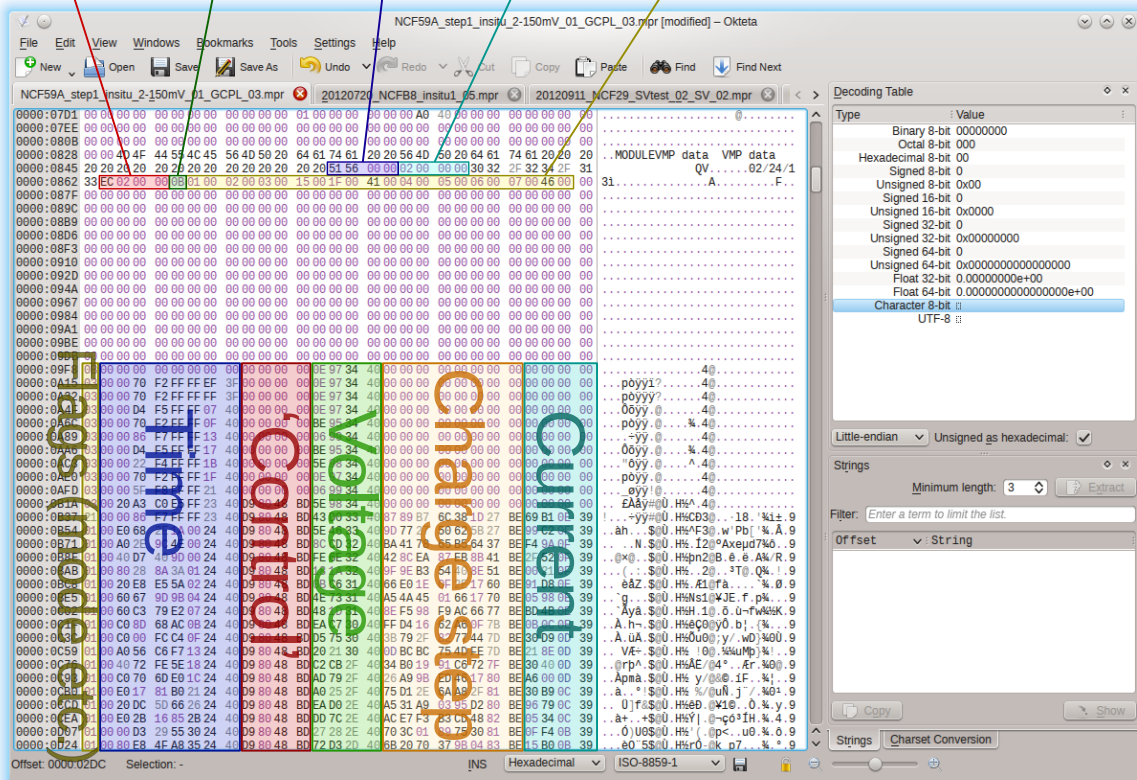


Figure C.2: The start of the “VMP data” block of a .mpr file, viewed in Okteta, with annotations showing the locations of various data.

C.2.2 “VMP data” block

Most interesting is the “VMP data” block (see Figure C.2, which follows the “VMP settings” block and, after an initial region of unclear significance, contains regularly patterned data that on inspection turn out to correspond to the values for time, current and so on that are exported in the `.mpt` file. Different files have the data columns in different orders or have columns that are not present in other files. However, there is a series of numbers at the beginning of the “VMP data” block which correspond to the columns present later on in the data block. For example, number 4 corresponds to elapsed time as a 64-bit floating point number, number 8 corresponds to current in milliamps as a 32-bit floating point number, while number 11 also corresponds to current in milliamps but as a 64-bit floating point number. See Table C.1 for the full list of column ID numbers whose meaning I was able to determine.

Table C.1: ‘Column ID numbers’ in the “VMP data” section of `.mpr` files

Number	Variable	Unit	Precision
1	‘mode’	(n/a)	2 bit integer
2	charge/discharge	(n/a)	1 bit boolean (true = charge)
3	error	(n/a)	1 bit boolean
4	time	s	64 bit float
5	‘control’	V mA^{-1}	32 bit float
6	voltage ($E_{w.e.}$)	V	32 bit float
7	charge step (ΔQ)	mA h	64 bit float
8	current (I)	mA	32 bit float
11	current (I)	mA	64 bit float
19	‘control’	V	32 bit float
21	control change flag	(n/a)	1 bit boolean
23	charge step (ΔQ)	mA h	64 bit float
24	cycle number	(n/a)	64 bit float (!)
31	‘Ns changes’ flag	(n/a)	1 bit boolean
65	counter increment flag	(n/a)	1 bit boolean
70	power (P)	W	32 bit float
434	charge (Q)	C	32 bit float

C.2.3 Timestamp and other data

The ‘module’ headers record the date that the file was created or saved, but for correlating *in situ* NMR spectra with the electrochemistry it is necessary to know the time to within a range of at most a few minutes. This information is clearly recorded in the file, because some (but not all) the exported text files include the time, to the nearest second, that data acquisition was started. (However, the exported text files do not include time zone information.) The location of the date and time information in the `.mpr` file was not

obvious, so an exhaustive search was carried out looking for bit patterns resembling the appropriate date and time in several different formats. After much trial and error, a 64-bit floating point number representing the date and time in the ‘Excel date format’* was found in the “VMP LOG” block, just before a string containing the filesystem path where the file was originally saved. As in the text files, there appears to be no information about time zone or daylight savings time.

There are still large regions of the `.mpr` files whose contents are not accounted for here. The latter parts of the “VMP settings” block clearly contain information about the program or ‘schedule’ controlling the current and voltage settings of the battery cycler. Elsewhere in the file, it is interesting to note that text strings are always preceded by a one-byte integer recording the length of the string, and also followed by at least one NULL character. In this way, they are valid both as ‘Pascal strings’ and as ‘C strings’.

C.2.4 Implementation details

The Python package `galvani`, available from <https://github.com/chatcannon/galvani>, provides the classes `MPTfile` and `MPRfile` which can be used to load `.mpt` text files and `.mpr` binary files respectively. The implementation is in the file `BioLogic.py` — `MPTfile` uses NumPy’s `loadtxt` function, while `MPRfile` defines a NumPy data type on the fly based on the column IDs described in Table C.1 and uses this to read in the electrochemical data as a Numpy ‘Record Array’.

C.3 TNMR format

Uniquely, TecMag actually provide documentation for the `.tnt` file format used by their TNMR software. (Although the Bruker data format has been documented by the authors of third party software, I was not able to find information about the file format, with the exception of the `audita.txt` and `auditp.txt` files, either on the Bruker website or in the documentation included with the `Topspin` software.) A low-level description of the `.tnt` file format is given in the document “A1 - TNMR File Format.doc” which is included with the TNMR installation. The meaning of some of the fields was not entirely clear, however, so a small number of test spectra of reference samples were acquired with unusual settings in order to elucidate their function.

The Python package `pytnt`, available from <https://github.com/chatcannon/pytnt>, provides a `TNTfile` class which can be used to open `.tnt` files and perform simple processing operations, including functions that are only really useful for *in situ* experiments

*The date and time representation in Microsoft Excel originated with a programmer who was unaware of the Gregorian calendar and therefore included February 29th, 1900 as a valid date. This bug is present in every version of Microsoft Excel, having been kept for reasons of backwards compatibility.

such as working out the time when a particular spectrum in a series was acquired. Part of the code in the `pytnt` package has been included in the larger `nmrglue` package written by Helmus and Jaroniec [168], allowing a much larger range of processing operations and conversion into several different file formats.

Appendix D

Availability of software code

D.1 ProfFitS

ProfFitS can be downloaded from <https://gitorious.org/proffits/proffits>. It is distributed under the GNU general public license (GPL) version 3 or greater, with the exception of some code adapted from SciPy [169] which is distributed under permissive (BSD or MIT style) licences. It is released as a Python package. A simple checkout of the git repository can be used without any compilation, but performance is greatly improved if the Fortran extensions are used — this requires `f2py` and a recent Fortran compiler. Since it makes heavy use of linear algebra operations, it is recommended that you ensure your NumPy installation is linked to optimised versions of BLAS and LAPACK.

D.2 RMCprofile

It is planned to make RMCprofile available as free open source software. At the time of writing, this has still not happened.

D.3 pytnt

The code for reading the TNMR `.tnt` format (see section C.3) is released as a package called `pytnt` and is available at <https://github.com/chatcannon/pytnt>. `pytnt` is released under a BSD-style licence. Some of the functionality has also been incorporated into the `nmrglue` package [168].

D.4 Galvani

The code for reading the Arbin `.res` and Bio-Logic `.mpr` file formats is released in a package called `Galvani`. It is available at <https://github.com/chatcannon/galvani> under the GPL version 3 or greater. The `.res` functionality depends on `mdbtools`.

D.5 NMR PCA and NMF

The code implementing the PCA and NMF algorithms used in chapter 5 is available at <https://github.com/chatcannon/nmrpca>. It is released under the GPL version 3 or greater.